IN-91
[illegible]

Final Report for Grant NAG5-4381
from the NASA Planetary Atmospheres Program

STUDIES OF TENUOUS PLANETARY ATMOSPHERES

Research Area: Composition/Structure/Dynamics of Comet and Planetary Satellite Atmospheres

Start Date: August 1, 1997
End Date: December 31, 1998

Principal Investigator: Dr. Michael R. Combi

Space Physics Research Laboratory
Department of Atmospheric, Oceanic and Space Sciences
The University of Michigan
Ann Arbor, Michigan
(734) 764-7226

I. PROJECT OVERVIEW

I.A. Scientific Objectives In order to understand the physical and chemical processes which produce the dust and gas comae in comets and various tenuous planetary and planetary satellite (upper) atmospheres through interactions with their particle, field, and radiation environs, it is necessary analyze remotely observed and spacecraft data with physically meaningful models. With this in mind, we have undertaken a coupled program of theoretical modeling and complementary data analysis regarding the distribution of dust and the possible production of gas species from dust in comets, and the global distributions of neutral and ionized gases in, and escape from, tenuous planetary atmospheres of Io and Europa. The theoretical models developed will have further applications to other tenuous atmosphere such as that of Pluto or the upper atmospheres of the terrestrial planets.

I.B. Significance and Relevance This project addresses prime areas of study central to current and future NASA missions and for the goals of NASA's overall program in the study and exploration of the solar system and its origin. In the published report of COMPLEX, the Committee on Planetary and Lunar Exploration, of the Space Studies Board, National Research Council, comets and the Jupiter system were identified in the highest priority group.

Comets are not only important as members of the solar system and thereby part of NASA's mission to explore the solar system, but also in their central role for understanding the origin of the solar system and possibly the chemistry of the outer "veneers" of the Earth and other terrestrial planets. The study of cometary dust/gas interrelations is important for *in situ* and sample return laboratory measurements in upcoming comet missions. In the near term an understanding of sodium dust chemistry obtained through the analysis of remote ground-based observations will be relevant in planning for the laboratory studies of harvested cometary dust particles in the Stardust Discovery mission, nucleus samples from the planned New Millennium Deep Space Four mission, and *in situ* dust instruments on ROSETTA, an ESA mission to a comet with significant NASA participation.

Io and Europa, their atmospheres, and their interactions with Jupiter's plasma torus, are prominent in current and future NASA science goals and missions. A unique combination of modeling tools which have been, and continue to be, developed at the University of Michigan have already been applied to understand Galileo particle and fields measurements obtained during its encounters with Io and Europa. Both the Galileo mission and the Galileo Europa mission and remote measurements with the Hubble Space Telescope will continue to be sources of new results, as data already taken is reduced and released, and as upcoming encounters with Io and Europa yield new important insight into these atmospheres. NASA is developing plans for the Europa Orbiter mission for studying the icy surface and mantle below the icy surface, which may hold the clues to the thin extended atmosphere.

I.C. Strategy and Approach Our overall strategy is and has been to develop and apply sophisticated models of the type normally used in purely theoretical studies for the purpose of directly comparing models with measurements in order to gain a deeper understanding of the physical state and composition of the atmosphere in question. Typical first-principles theoretical investigations produce many detailed calculations to explore the type and range of physical phenomena that might or should occur, but are often only loosely constrained by observed characteristics and are often limited to physically overly simplistic assumptions. On the other hand, typical measurements, whether Earth-based and near-Earth based remote observations, or *in situ* spacecraft measurements, are often limited to fairly simple model analyses (scale-height distributions, uniform columns, constant temperatures, simple imposed uniform magnetic fields, etc.). The PI's approach throughout his studies with collaborators dealing both with comets and satellite atmospheres has been to use physically meaningful models and compare directly with data. For this reason we have developed the core modeling tools, and either analyzed published measurements, or established various collaborations with observers. The subjects of study covered here are unified by this overarching strategy.

II. SCIENTIFIC BACKGROUND

II.A. Scientific Background: Dust and Sodium in Comets The standard dust coma treatments originated with the pioneering work of Finson-Probstein (1968a&b) which considers the dust to consist of a population of spherical particles having a range of sizes with a distribution determined by a power law in particle diameter. The particles were considered to have a constant density, $\rho(a) = \rho_o$ independent of particle size. The light scattering properties, which are needed to describe the observed scattered radiation, and to calculate the radiation pressure acceleration on each particle size, were considered to be simply proportional to the geometric cross section of the particle implying that the light scattering efficiency, Q_{scat} and the radiation pressure efficiency, η_{rp}, both equal unity and are independent of particle size. It is clear from the work of a number of investigators that these underlying assumptions are highly oversimplified for physical dark absorbing dust particles (e.g. see the review by Grün &Jessberger 1991).

The Finson-Probstein approach has been advanced in recent years to include various complex physical parameterizations including porous (fractal aggregate) size-dependent dust density, realistic radiation and radiation pressure scattering efficiencies for dark dielectrics, anisotropic production, and fragmentation (Fulle et al., 1993 & 1997; Konno et al., 1993; Combi 1994). The difficulty in interpreting observed monochromatic two-dimensional images of the coma and tail is that the parameter space is underconstrained. Even for complicated inversion techniques (Fulle et al.), it is necessary to adopt some of the parameterizations, fix some parameters, and solve for others. So, one can get a mathematical inversion that is only unique within the constraints of the underlying assumptions and parameterizations.

We (Combi 1994) had found that dust images of the coma provide evidence that the 1-to-1-to-1 Finson-Probstein type relationship between particle size, velocity, and radiation pressure, implicit in most dust coma analyses, does not hold in general. We arrived at a similar and independent suggestion as Fulle et al. (1993 & 1997) had: that particle fragmentation within and/or just outside the dusty-gas acceleration region ($r < 1000$km) would produce this effect. Analyses of the Giotto Halley Multicolor Camera images independently point to fragmentation (Konno et al. 1993; Keller et al. 1990). More recently, Crifo and co-workers (preprint) have suggested another possible mechanism which would violate the 1-to-1-to-1 Finson-Probstein relation, that is, if cometary particles come in a range of shapes (i.e., not just spherical, e.g., flat, or long and thin), a velocity range for any particular average particle size could also result. It is only through continued work on the detailed model analysis of observational data of dust in comets, preferably multi-wavelength observations, that further progress can be made.

Sodium in comets has received much recent attention with the announcement of spectacular sodium tail images in comet Hale-Bopp (1995O2) in the press releases and first papers by Cremonese et al. (1997) and Wilson et al. (1998). However, sodium tails in comets have been reported in observations going back to the early part of the century. Our recent paper (Combi et al. 1997) contains a review of many of the older observations.

II.B. Scientific Background: Tenuous Atmospheres The nature of the atmospheres and ionospheres of Jupiter's natural satellites Io and Europa and their interactions with their surrounding radiation, and particles and fields environments is a very active and timely field of study. Various kinds of work, depending on different regime-dependent approaches have been adopted in recent years, with the hope of understanding the basic global structure of the atmospheres, and their interactions with solar radiation and with the Jovian plasma torus environment.

Io's interaction with Jupiter's corotating plasma torus has been studied for over 25 years. Io has a neutral atmosphere which is probably locally thick but rather uneven across its surface. (See Lellouch 1996 for an excellent review of pre-1996 literature.) The ultimate source for atmospheric gases appears to be the numerous active volcanoes on the surface, moderated by

condensation and sublimation from the surface. The energetic particle environment near Io is responsible for the balance of the plasma heating, Joule heating, ionization, and surface and atmospheric sputtering, and in some form drives the escape of the neutral atmosphere (Schneider, Smyth, & McGrath, 1989).

Our understanding of the interaction of Io with Jupiter's corotating plasma goes back to the discovery of Io-related decametric radio emission discovered by Bigg (1964) and the unipole inductor model which explains it (Goldreich & Lynden-Bell 1969). There were a number of theoretical studies of this interaction during the immediate post-Voyager era (See Hill et al. 1983 for an excellent post-Voyager review). Early theoretical work was often done either in the context of a "thin" atmosphere [e.g., see Cloutier et al. 1978] indicative of the surface temperature (~130 K), or "thick" extended neutral atmosphere (e.g. see Goertz 1980) more indicative of volcanic temperatures (~1000 K). Subsequent evidence (again see the review by Lellouch 1996) seems to indicate a mixed picture of the global atmosphere, which has a large extended corona like a thick atmosphere, but appears to be dominated by local major injection of hot (high speed) gas/dust plumes to high altitudes but only near active volcanic vents. Therefore, although the atmosphere is probably only locally thick, it still has a large extended neutral corona which might provide a sufficient source of impact ionization and photoionization.

SO_2 appears to be the major primary constituent in Io's atmosphere (Ballester et al., 1994; Lellouch et al., 1992), but observations to date still only provide hemispherically averaged total column abundances. The sodium eclipse measurements of Schneider et al. (1991) are the only unambiguous information we have about the vertical distribution of neutral gas species in the corona of Io from about 1.4 to about 6 R_{Io}. They found a power law with an exponent of $\alpha \sim -3.5$ described this distribution. Smyth & Combi (1997) have shown that this vertical distribution of sodium from the Schneider et al. eclipse observations and the more typical emission profiles of more spatially extended sodium can together be explained by a single modified incomplete cascade sputtering distribution, which results naturally from multiple neutral-neutral and ion-neutral collisions between torus ions and atmospheric neutrals. The interpretation of recent Hubble observations of various UV emissions of atomic S and O (Ballester et al., 1997) is complicated by the fact that the spatial distributions of the emissions are determined by a combination of the mass distribution in the atmosphere with excitation by the plasma density and temperature environment. Theoretical and empirical models have explored the structure of the neutral atmosphere and its behavior to various gas sources and energetic heating and ejection processes, such as sublimation, volcanic ejection, surface and atmospheric sputtering, UV, plasma, and Joule heating, and LTE and non-LTE IR radiative cooling (Sieveka & Johnson 1985; McGrath & Johnson 1987; Moreno et al., 1991; Strobel et al., 1994; Pospiezalska & Johnson 1995; Wong & Johnson 1995 & 1996). Recent work by Summers & Strobel (1996) models the photochemistry and energy balance for Io's atmosphere accounting for vertical transport via the adoption of eddy mixing (and the eddy diffusion coefficient) in a 1D-spherical model. Wong and Johnson (1995 & 1996) have addressed 3D structure as well as horizontal and vertical transport explicitly with a hydrodynamic approach. Finally, Marconi et al. (1996) have addressed aspects of transition from a lower thick atmosphere to an upper escaping atmosphere using a layered approach for a 1D-spherical, single-species Io-type calculation solving hydrodynamic equations at low altitude and performing Direct Simulation Monte Carlo calculations at high altitude. Boundary conditions are passed back and forth between the two approaches.

Recent observational studies (Belton et al. 1996; Ballester et al. 1997; Trauger et al. 1997; Roesler et al. [private communication]) seem to indicate that the atmosphere/ionosphere around Io envelopes the satellite at low altitude, but that there are major aspherical anomalies at higher altitudes both toward and away from Jupiter, and in the direction of the wake. There may be variations with the local magnetic system-III longitude (i.e., the position of the plasma torus). Despite all the recent advances in theoretical work, still only a rough sketch of the some aspects of the structure of the global atmosphere can be made. It is clear that vertical and horizontal transport, day/night and upstream/downstream asymmetries, local peculiarities, and time-variations are all important in shaping the global atmosphere.

There have been a number of 3D numerical studies of the plasma flow past Io (Linker et al., 1988, 1989, 1991; Wolf-Gladrow et al., 1987). Because of the complexities in the problem and numerical difficulties, they have been limited to restricted portions of the problem, have introduced fixes like artificial viscosity, or have been run using less than fully physically realistic conditions. Linker et al. (1991) have performed the best example to date of 3D MHD modeling of Io. They used the two-step Lax-Wendroff method. These calculations were performed on a non-uniform but fixed structured grid, and artificial dissipative terms (artificial viscosity) had to be introduced to the basic MHD equations in order to make them computational stable. Our contribution in this area is discussed in the next section.

Although neutral oxygen (Hall et al. 1995) and sodium (Brown & Hill 1996) have only recently been detected in a neutral atmosphere around Europa, suggestions that an oxygen atmosphere should accumulate above the water-ice surface actually go back 20 years (Yung & McElroy 1977; Kumar & Hunten 1982). Further confirmation of the existence of an atmosphere was provided recently by detection of an ionosphere in radio occultation experiments from the Galileo Orbiter (Kliore et al. 1997). The current working scenario is that water molecules breaking up near the surface would, through chemical reactions, produce O_2 and H_2, but the lighter H_2 would prefentially escape leaving an O_2 lower atmosphere, an atomic O upper atmosphere/exosphere, and an O^+ ionosphere. Recent 1D-spherical calculations (Ip 1996) suggest a possible two component exosphere: a lower thermal population with a small scale height, and an upper corona extending a few satellite radii.

Recent theoretical work on the atmosphere/exosphere/ionosphere of Europa has been done using diffusive photochemical and energy-balance models. Being constrained by the observations of Hall et al. and Brown & Hill, Ip et al. (1996) have made 1D-spherical calculations that predict a lower atmosphere with a moderate exponential scale height and an extended corona. Sauer et al. (1996) have begun a study of 3D aspects of the interaction of Jupiter's plasma torus with Europa's atmopshere. They adopt multiple 1D hydrostatic-type diffusive profiles for the atmosphere and account for chemistry and energy balance and the impacting plasma torus. They solved for the effects of currents and electric fields assuming a constant and uniform magnetic field. The recent flybys of Europa by the Galileo orbiter indicate the presence of an ionosphere (Kliore et al. 1997), roughly consistent with expectations from the O detection, and a disturbed local magnetic field (Kivelson et al. 1997) which could be accounted for by an intrinsic field or possibly an induced field (Kivelson, private communication). Our new studies of the effects of ionospheric mass-loading on the flow and local magnetic field are discussed in the next section.

III. PROGRESS AND CURRENT WORK STATUS

III.A. Progress of Work: Dust Coma Studies During the last few months of the current grant, our plan was to complete the analysis of the comet Austin (1989 C1) dust coma images in collaboration with Dr. David Schleicher. For this work we are performing a similar dust coma analysis as was done for the comet P/Halley images as described in the paper by Combi (1994). Observations of the coma of comet Austin indicated a fairly steady and uniform production of gas and dust (Schleicher, private communication), not complicated by large amplitude time-dependent variations or aspherical production. It provides a good testbed for studying the role for dust velocity dispersion (for each particle size) that could result from particle fragmentation. We have contour plots of one of the images, however, Dr. David Osip who was a postdoc with Dr. Schleicher during the observation and reduction of comet Austin data, was to provide us with the images in digital form. In anticipation of receiving the digital data and using the contour plots, the modeling background work was begun and preliminary model calculations were performed and compared with the observed coma.

For Halley, Combi (1994) found that 3 images of the dust coma could not be adequately reproduced with a straightforward Finson-Probstein type formulation. A model which produced dust particles that fragmented into smaller particles after they reached terminal velocity in the

dust-gas drag region could reproduce the images. In keeping with the Monte Carlo nature of the calculation a "heuristic" dust fragmentation parameter was constructed in the form

$$d_f = d_0 R^a$$

where d_0 is the radius of a dust particle before fragmentation, R is a random number on the interval of 0 to 1, and a is an adjustable postive parameter. There is no fragmentation for a value of a = 0, and much fragmentation for a value as large as 4. This formulation has the interesting property of conserving the form of the size distribution which varies from $d^{-3.2}$. to $d^{-3.4}$. Combi (1994) had found that with a value of a = 2 three images of the dust coma taken at heliocentric distances of 1.82, 1.45 and 1.08 AU before perihelion could all be well reproduced by the model. A value of p = 2 means that each original particle fragments on the average into 27 particles. This is consistent with the analysis of the Giotto camera images of the dust coma very near to Halley's nucleus by Thomas and Keller (1990), who found that each original dust particle had to fragment into at least 2.7 particles as a lower limit.

For comet Austin the first sets of model calculations indicated that the power law exponent of the particle size distribution had to be changed. This is actually consistent with the results of Fulle et al. (1993) for comet Austin. It is clear from the preliminary results that a model with a moderate amount of fragmentation will be required (a ~ 2) but without a careful comparison with the actual digital image data it is impossible to reach an clear conclusions at this point. This work will be continued and completed in the coming months after the current grant period, but the preliminary comparison is illustrated in Figures 1 and 2.

In addition to the apparent direct production of gaseous sodium (Na) from the nucleus (Combi et al. 1996, 1997; Cremonese et al. 1997; Brown et al. 1998), there have been reports of observations of comet Hale-Bopp giving convincing evidence for a possible production of gaseous Na from dust, both in the coma of the comet (Brown et al. 1998; Rauer et al. 1998; Arpigny et al. 1998), and far down the dust tail (Fitzsimmons et al. 1997; Wilson et al. 1998). Figures 3 a&b show two images of the cometary Na tails taken by Wilson et al. in March 1997 and by Cremonese et al. in April. Both the brightness down the tail and the tail position angle with respect to the sunward direction from the April image has been shown with some simple model calculations by Cremonese et al. to be consistent with a nucleus or near-nucleus source, similar to the direct nucleus source component seen in comets observations of comets Bennett, Kohoutek and Halley (Combi et al. 1997). However, Wilson et al. conclude from their March image that neither the brightness distribution nor the tail position angle are consistent with a direct nucleus or near nucleus source. Some sodium must be produced by an extended source out in the dust tail. Based on long-slit spectroscopy of the coma region (distances < 2 x 10^5 km) Brown et al. (1998) report roughly equal contributions to the total gaseous Na production rate in comet Hale-Bopp coming from the direct nucleus source and the extended dust source. This raises interesting questions regarding the processing of dust particles once liberated from the nucleus, both over short periods of time in the coma and long periods of time required to travel large distances down the tail and to fill interplanetary space. Is observed cometary Na eroded only from the surfaces of typical dust particles? Or, does the gaseous Na originate from a population of dust particles, like the mixed CHON-refractory particles that might completely disintegrate? The careful detailed modeling of remote ground-based observations of gaseous Na in the comas and tails of comets will provide important results in this area.

Spatial profiles of Na in three comets (Bennett 1969 Y1, Kohoutek 1973 F, and 1P/Halley) were determined by Combi et al. (1997) from long-slit spectra (2D spatial/spectral images) with the slit aligned both parallel and perpendicular to the comet-sun line, and displaced antisunward. Like the various reported Hale-Bopp measurements they found evidence for a source of gaseous Na which originated at the nucleus (or a very short-lived parent species). Unlike Hale-Bopp which seems to show an extended source spatially coexistent with the dust in the sunward coma and tail, we found a large and highly temporally variable extended source on the tailward side of the nucleus, that bore a remarkably similar spatial morphology to that of H_2O^+, but no similarity to the dust continuum profiles determined from the same data. This

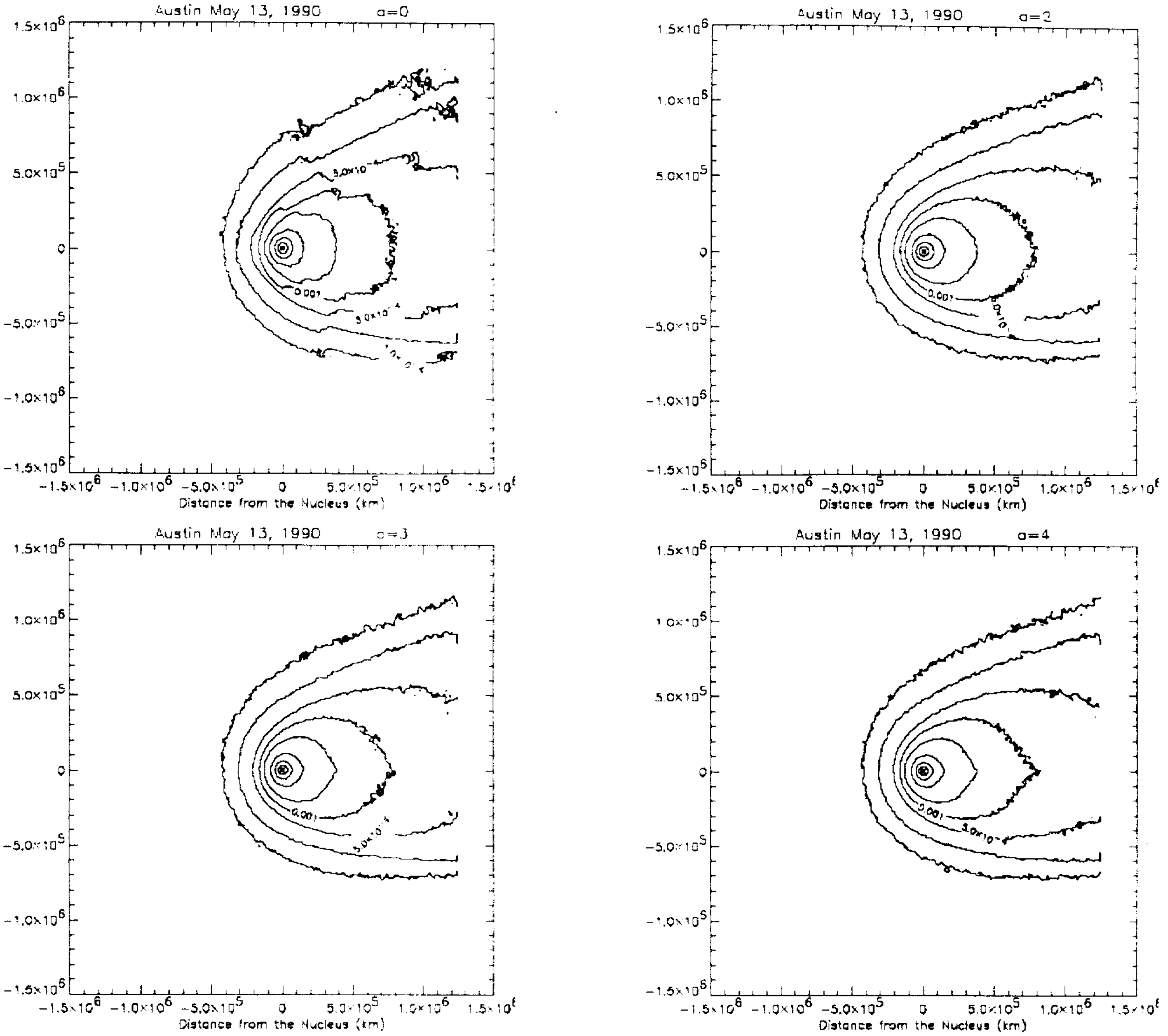

Figure 1. Fragmentation Models for Comet Austin. Shown from the upper left are four models for the comet Austin observation geometry in mid-May 1990 with four values of the fragmentation parameter, a. As in the case of Halley, clearly the simple model without fragmentation (a=0) is not correct, but at this point it not clear which model is best when comparing with the contour plot of the observation in Figure 2.

tailward extended source varied by factors of a few from day-to-day in two of these comets, and was most noticeable in observations of these "old" comets at heliocentric distances < 0.9 AU. All three of these comets had similar gas production rates that were more than an order of magnitude smaller than Hale-Bopp at comparable heliocentric distances. Clearly an important aspect of understanding cometary sodium will be differences from comet to comet.

Combi et al. showed that a direct nucleus source model could describe the sunward profiles and the inner part of the antisunward profiles in the three "old" comets. It accounted for direct production of Na from the nucleus, the heliocentric velocity dependences of the radiation pressure acceleration and the g-factor (from the solar Fraunhofer lines), collisional entrainment within the inner part of the expanding water coma, and photoionization. We showed that (1) collisional entrainment could explain the sunward extension of the profile, (2) an extended source was required to explain most of the tailward spatial profiles in all three comets, (3) the photoionization lifetime as computed from theoretical cross sections, which is 3 times longer than that computed from old experimental cross sections (Huebner, Keady and Lyon 1992),

seems to be correct, and (4) that the nucleus (or near-nucleus) source of gaseous Na seen in the coma was about ~1% of that expected from solar abundances. Cremonese et al. (1997) independently reached a similar conclusion about the Na lifetime and the production rate in comet Hale-Bopp. All the observational and model analysis results of Combi et al. (1997) had already been presented at the Asteroids, Comets, Meteors conference by Combi et al. 1996, 9 months before any of the observations of Na in comet Hale-Bopp.

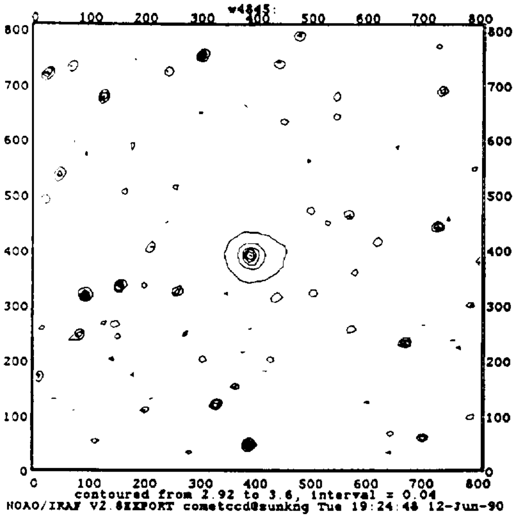

Figure 2. Contour Plot of Dust Coma Image of Comet Austin. Shown is a contour plot of the dust coma of comet Austin taken with a 4845 Å filter. The square field of view is roughly comparable to the models shown in Figure 1.

Brown et al. (1998) have compared a Monte Carlo model to their measured spatial and line-of-sight Doppler velocity profiles of Na in comet Hale-Bopp along a long slit aligned with the comet-sun line. Their model includes a calculation for an extended dust source and a nucleus source. Their analysis notes and indirectly accounts for the collisional coupling between Na atoms and molecules in the inner coma by avoiding that portion of the calculation. None of the published models so far (Combi et al. 1997; Cremonese et al. 1997; Brown et al. 1998; Kawakita and Fujii 1998) can address all combinations of effects which are actually important to sort out all the important physical effects at the same time, in all the data, including the orbital dynamics effects and extended production from the dust coma and tail.

Work has begun to incorporate an extended source of Na from dust in our full 3D dust model and to make a first study. The shell of the dust coma model is actually the same code as was developed years ago for our hydrogen coma model (Combi & Smyth 1988a&b). A calculation of an extended Na from dust model then is just a merger of the core source region parts of the H coma model and the dust coma model. In this calculation the time-history of a Na atom follows the same sequence as now done for H atoms. The calculation accounts for the extended production of Na atoms from a dust coma/tail distribution, the time-dependent variation of the dust/gas production rates, the heliocentric distance dependence of the Na lifetime, the heliocentric distance and velocity dependence of the Na g-factor and solar radiation pressure acceleration. These results can then be added as necessary to a direct nucleus component for comparison with data which of course includes Na from both sources.

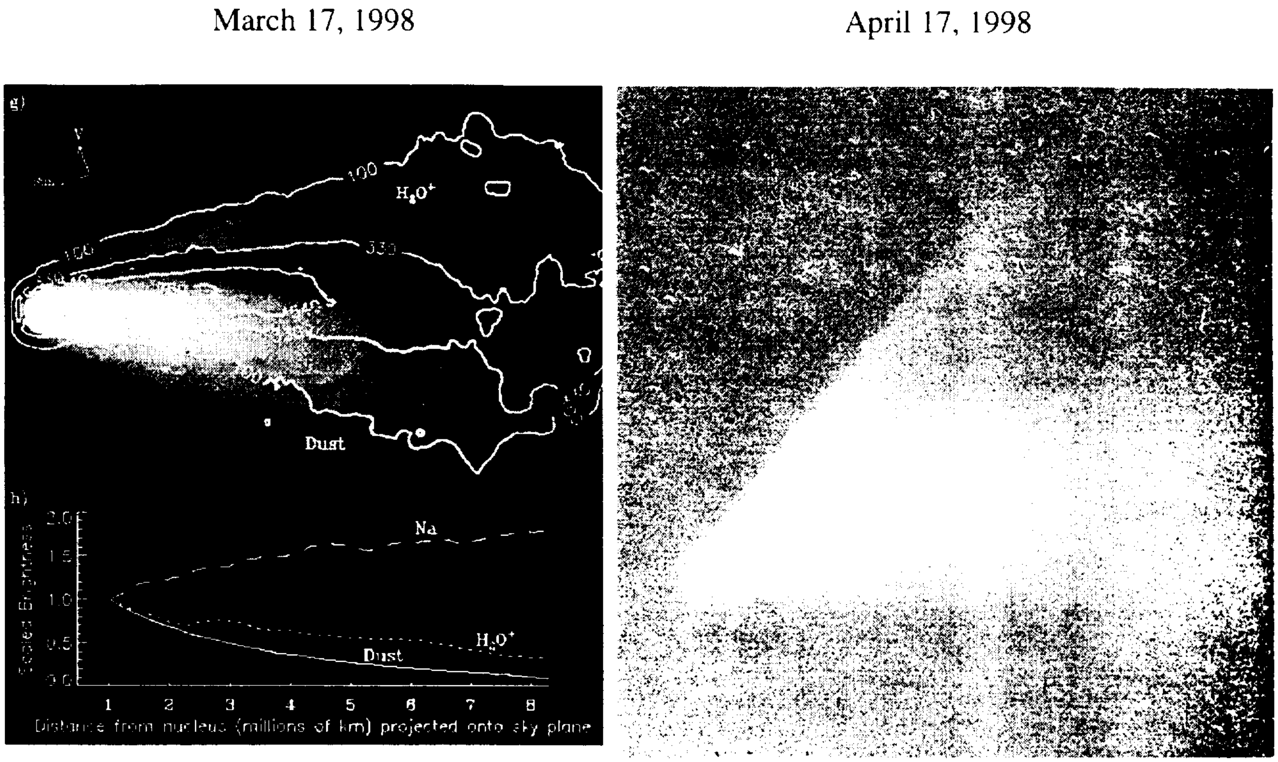

Figure 3. Images of the Sodium Tail in Comet Hale-Bopp. At the left is a contour plot of the sodium image from Wilson et al. (1998) after complete subtraction of the underlying dust superimposed over the false color versions of the H_2O^+ and dust-continuum tails. At the right is the narrow-band interference filter image obtained by Cremonese et al. (1997) which includes a combination of sodium (the long thin feature running from the head toward the uppermost right) plus the underlying dust tail (the diffuse structure running toward the right). Clearly the long, thin and bright sodium tail seen by Cremonese et al. in April was not apparent a month earlier.

Figure 4 shows our prelimary model calculation for the Na distribution for comet Hale-Bopp as produced by the dust in the coma and tail, corresponding to the March 17, 1997, data of Wilson et al. (1998). Figure 5 shows a direct nucleus source model for the April (Cremonese) observations. The direct nucleus model does produce a long straight Na tail as described by Cremonese et al. (1997) for April. (Note the spatial scale of the model is much larger than the image. The observations only cover the inner straight portion of the Na tail which is shown in the model to have some curvature at larger distances.) The model reproduces both the variation of brightness down the tail and the position angle of the tail in a single self-contained and self-consistent calculation. Cremonese et al. had presented some calculations for the average velocity and brightness down the tail using a simplified calculation and compared it with their spectral observations. Separately, they presented some syndynamic calculations of the apparent position angle of the sodium tail in their image data, given some representative values of the β parameter (the ratio of the radiation pressure acceleration to the sun's graviational acceleration). Our model combines all effects realistically in a single Monte Carlo numerical simulation As it should be, our nucleus-centered model is consistent with the simple model calculation of Cremonese et al. (1997) in terms of the brightness and velocity variations down the tail, as well with as the position angle of the sun.

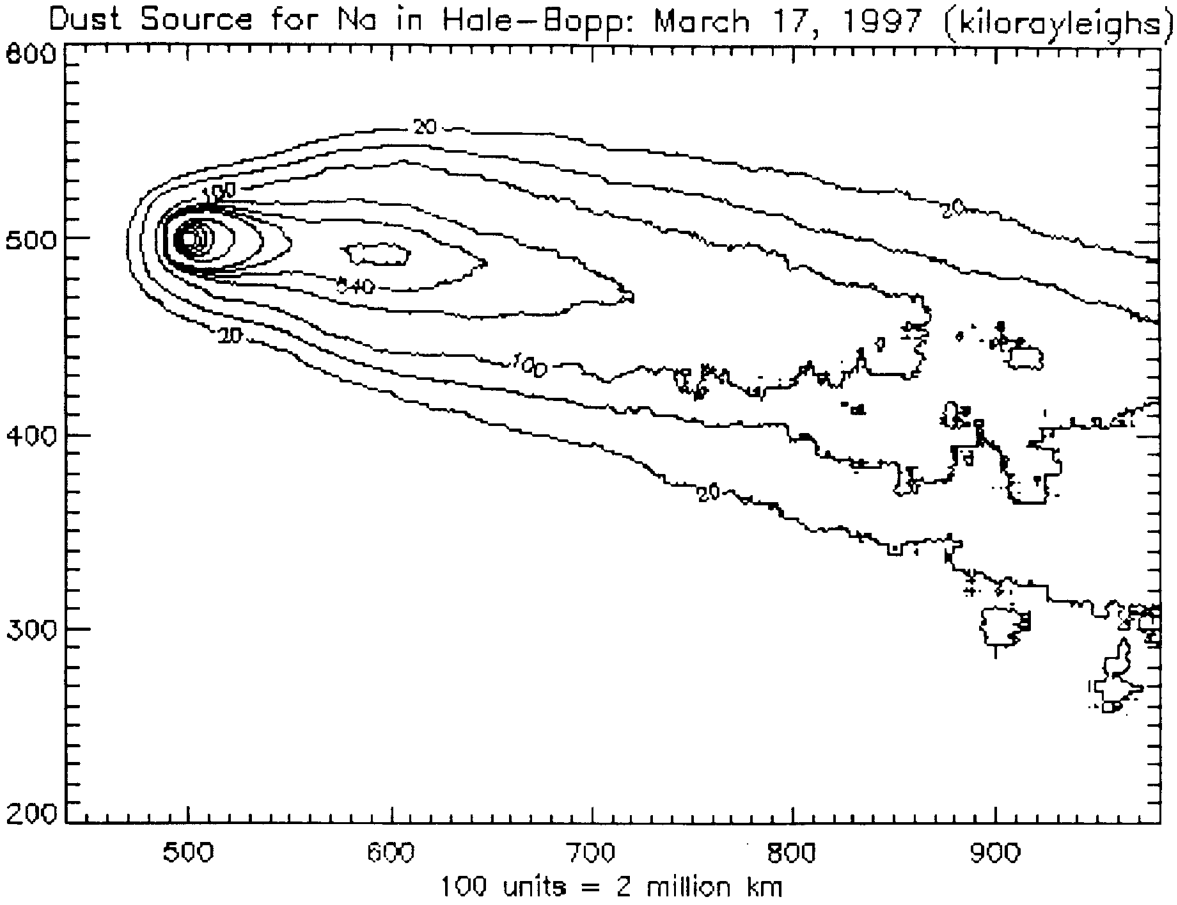

Figure 4. Model Calculation for a Dust Source of Gaseous Sodium. Shown are contours of brightness (in kilorayleighs) for a model calculation where sodium atoms are produced from dust with a production rate proportional to the surface area of the dust particles. The sun is to the left.

The direct nucleus source model for the March (Wilson) observation, not shown here, looks very similar to that for April (although overall not as bright as April for the same production rate). Clearly it does not look anything like the March observation. On the other hand, the basic behavior in the March image is reasonably well reproduced by the model produced with the dust source. No effort has yet been made to carefully reproduce the brightness distribution or simultaneously reproduce the dust tail image by adjusting the dust model parameters. This work is left for after the current grant period. The dust model includes a nominal dust size power law distribution (28 particle sizes distributed logarithmically from 0.1 µm to 1 cm). Dust terminal velocities are calculated using Sekanina's approximate formula (see Sekanina 1981 and Sekanina and Larson 1984). The model reproduces the approximate position angle of the Na tail (about mid-way between the ion and dust tails) and the small peak in brightness (750 Rayleighs) located at about 2 million km down the tail as seen in the observations of Wilson et al. (1998). This peak results from sodium atoms produced in the vicinity of the nucleus and pushed to large enough antisunward velocities so that they appear (in velocity space) to go first through the center of the solar Fraunhofer line absorpton and over to the red side wing. This produces a large increase in the effective g-factor between the nucleus and this location. (See also the later discussion in connection with Figure 7.)

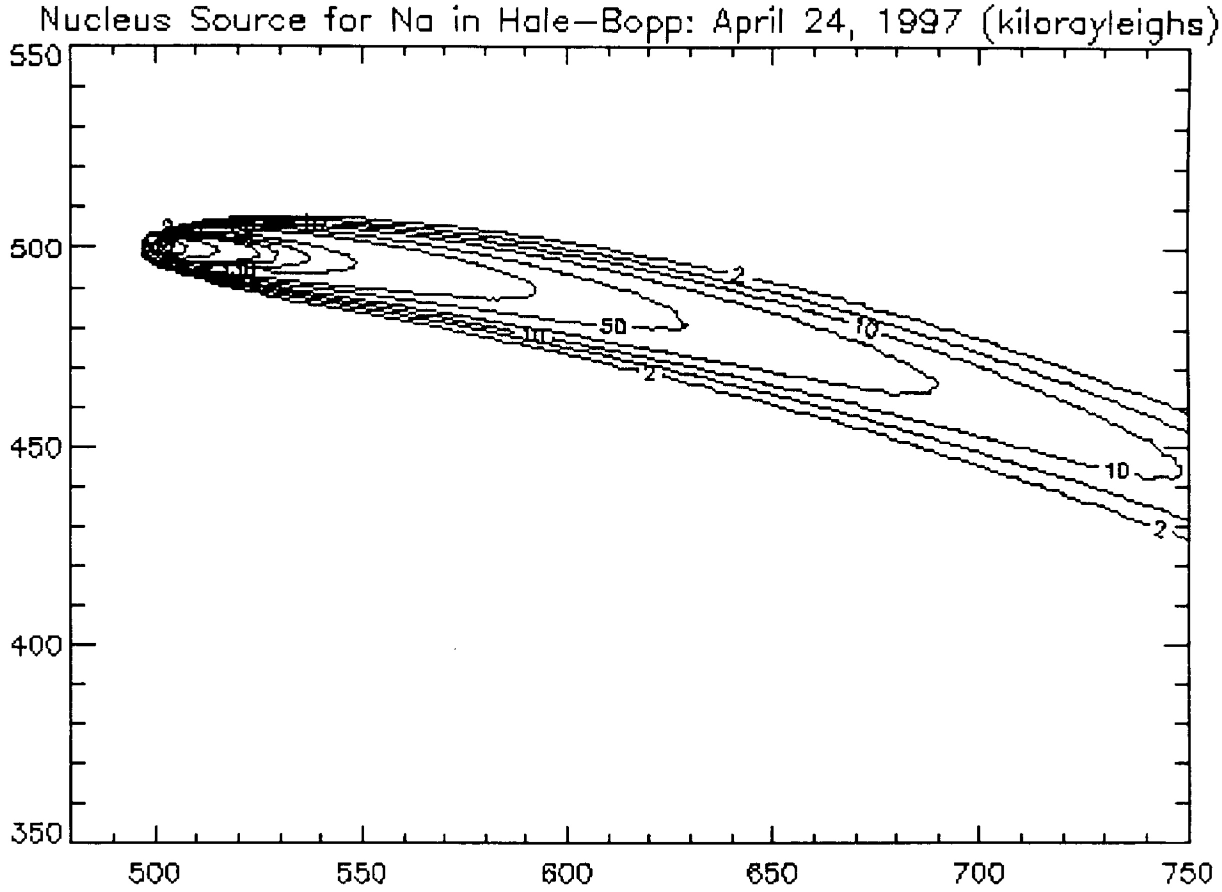

Figure 5. Model Calculation for a Direct Nucleus Source of Gaseous Sodium for April 24, 1997. Shown is a model calculation for a direct nucleus source for sodium under the influence of collisional entrainment in the outflowing water coma, the heliocentric velocity dependent radiation pressure acceleration and g-factor, and 3D time-dependent solar orbital dynamics. The linear dimension is as in Figure 4: 100 units = 2 million km. The sun is to the left. The map is projected for the Earth-comet-Sun geometry of the date.

Figure 6 shows the result of a calculation of the dust source model corresponding to the April postperihelion image of Cremonese. The sodium produced from dust in the inner coma does produce a long straight tail similar to that observed, but the brightness profile close to the nucleus for this extended source does not reproduce the observations. However, based on the Cremonese et al. image alone, it is not yet possible to put a limit on the contribution to the total sodium product in the dust source compared with the direct nucleus source because the dust contribution was not subtracted.

Recently, Kawakita and Fujii (1998) have presented model calculations for the March (Wilson) and April (Cremonese) images using the same Monte Carlo procedures as had been applied by us (Combi et al. 1997) for the sodium distribution in the inner coma of the three "old" comets. This calculation includes the heliocentric velocity dependent radiation pressure acceleration and g-factor for sodium atoms and collisional entrainment of sodium atoms in the

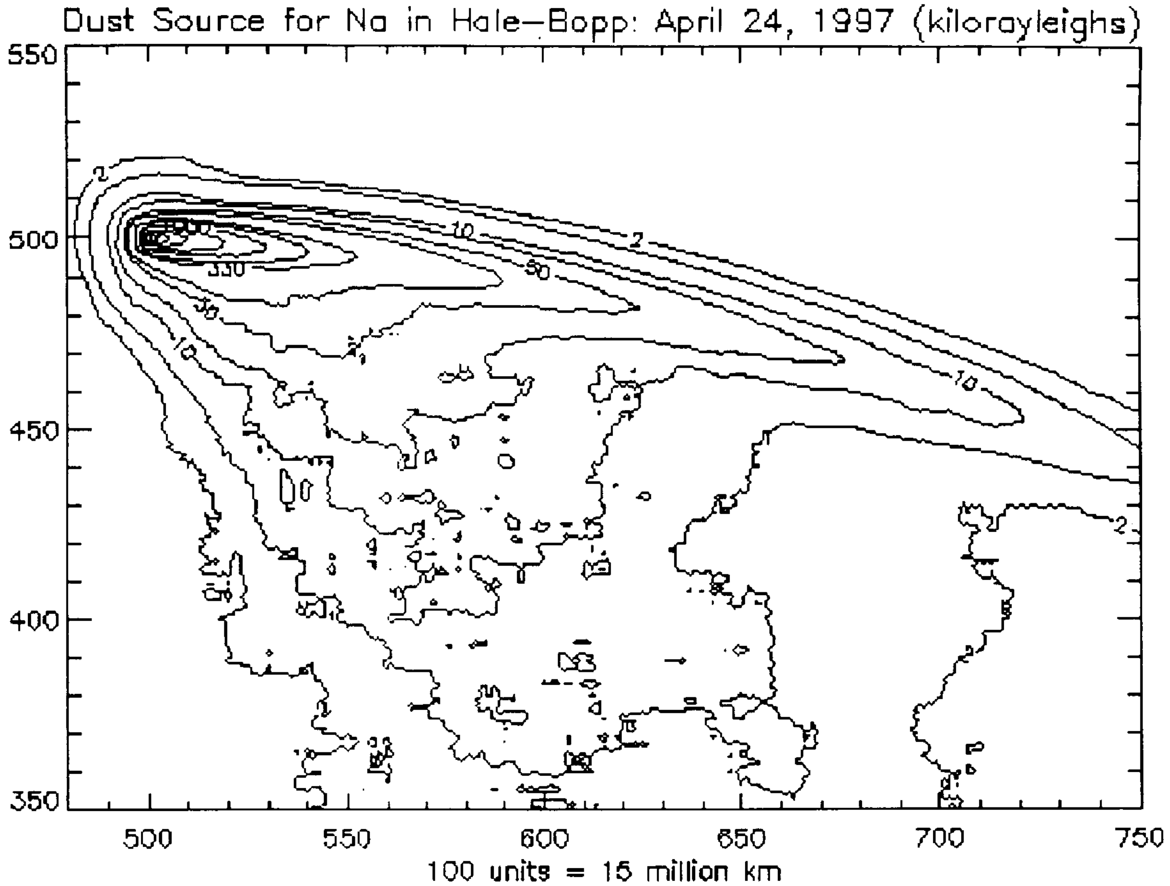

Figure 6. Model Calculation for a Dust Source of Gaseous Sodium for April 24, 1997. Shown is a model calculation for a dust source of gaseous sodium corresponding to the image of Cremonese et al. (1997) who report a long straight tail at this time.

outflowing water-dominated coma, but does not include the full 3D sun-centered orbital dynamics calculations of our new direct nucleus model, nor does it address the dust coma/tail source for sodium. Kawakita and Fujii conclude (based on these rather incomplete modeling studies) that the major difference between the March and April images can be explained simply by the difference in the radiation pressure acceleration environment between the two periods. There is some validity to their suspicion in this regard, but it does not explain the whole story. Figure 7 shows a plot from Combi et al. (1997) showing the variation of the radiation pressure acceleration on sodium atoms with heliocentric velocity. Note that the g-factor, not surprisingly, also has a similar shape. The heliocentric velocity of comet Hale-Bopp for the March and April time periods are also noted in the figure. Note the arrows anchored at the positions of the comet's rest frame for each date show the direction (red shift) of liberated sodium atoms in the coma and tail. It is true that one would expect the tail to be longer and the brightness to be higher in April than March as suggested by Kawakita and Fujii. However, their calculation does not (and cannot) address the difference in position angle with respect to the sunward direction between the two time periods. The difference in position angle <u>is not explained</u> simply by the difference in heliocentric velocity. So, although they may be correct in stating that the long straight Na tail produced by the direct nucleus source should be weaker in March than in April, the appearance of the overall tail in March cannot be explained simply by this effect alone. It is clear based on our preliminary calculations, which are consistent with the suggestions of Wilson et al. (1998), that a direct nucleus source alone cannot explain the position angle of the tail. Our preliminary dust coma/tail source model (Figure 4) clearly shows that a dust coma/tail source

probably explains most of sodium that is seen in the extended tail images of Wilson et al. in March.

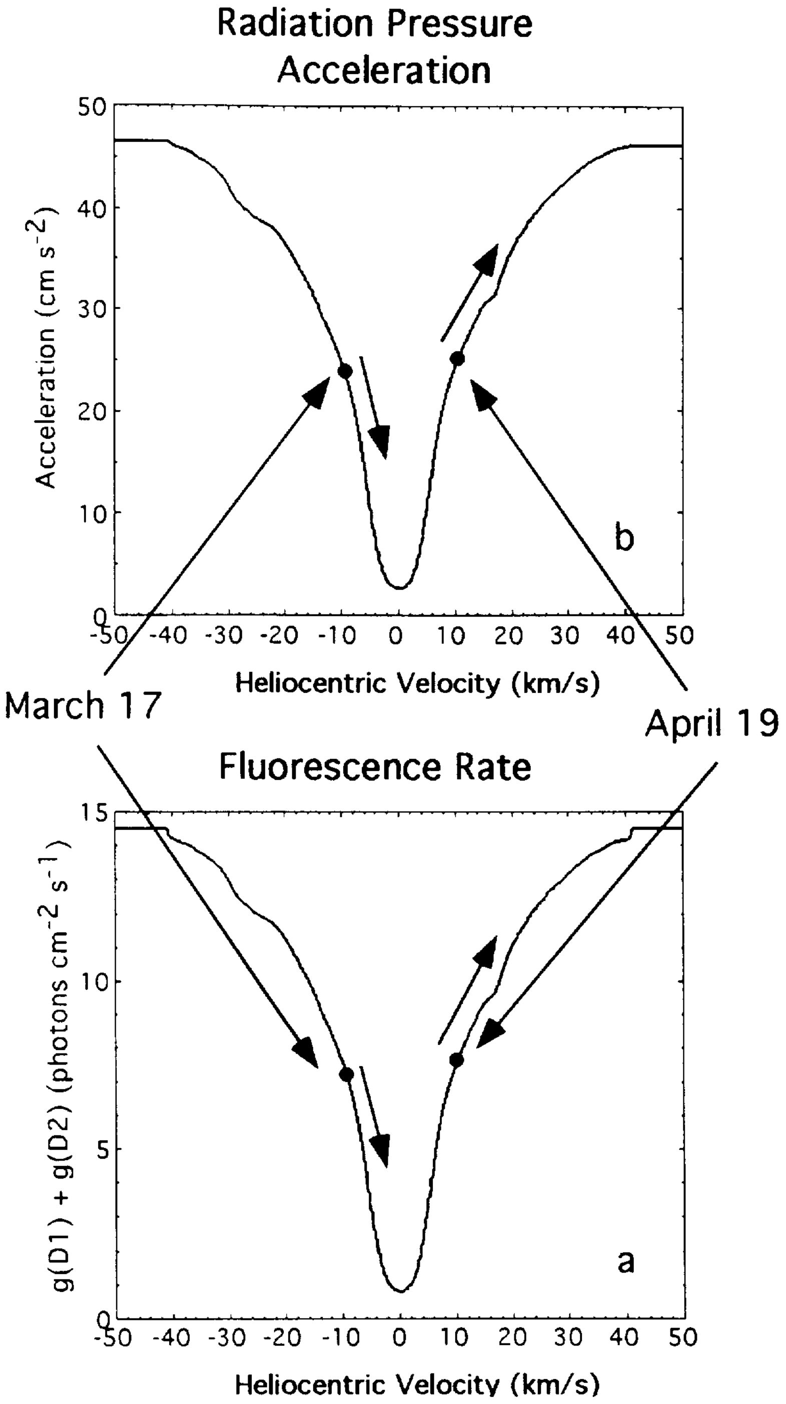
Radiation Pressure Acceleration

Fluorescence Rate

Figure 7. Heliocentric Velocity Dependence of the Radiation Presssure Acceleration and Sodium G-factor Shown is a figure from Combi et al. (1997) of the variation of the radiation pressure acceleration (above) and fluorescence rate (below) with an atom's heliocentric velocity. The heliocentric velocity of an atom in comet Hale-Bopp's rest frame for mid-March (Wilson et al.) and mid-April (Cremonese et al. image) 1997 are shown.

Finally, the PI was invited to give a talk on Dust-Gas Interrelations at the First International Conference on Comet Hale-Bopp which was held on February 1998. The topic involved dust coma subjects appropriate to this project and gas coma subjects appropriate for another. Work in the months preceding the talk involved reviewing dust and gas issues pertaining to comets in general and Hale-Bopp in particular, such as extended source of gas from dust, dust fading, and dust fragmentation. A paper "Dust-Gas Interrelations in Comets: Observations and Theory" (Combi et al. 1998b) was submitted for the special refereed proceedings volume of "*Earth, Moon, and Planets.*" As of this writing the paper has been revised and is about to be resubmitted. From the language in the review and interchanges with the editor we expect this version will be accepted in the next few weeks.

III.B. Progress of Work: Tenuous Atmosphere Studies Two models and modeling efforts serve as the bases of the work described in the tenuous atmosphere portion of this proposal. One is a major modeling effort directed by our colleague, Dr. Tamas Gombosi, involving several complementary subsets and collaborative efforts with other independent scientists at Michigan (like the PI and Co-I of this proposal), to develop robust and efficient 3D MHD and hydrodynamic computer codes for application to various problems in Earth and Solar System space science. These include, for example, the Earth's magnetosphere, the heliosphere (Linde et al. 1998), the comet solar-wind interaction with ion-chemistry (Gombosi et al. 1996; Häberli et al. 1997), the dusty-gas comet coma (Combi et al. 1998b), the comet-like interaction of the solar wind with Mars and Venus (Bauske et al. 1998), the magnetospheres of the outer planets, and the interactions of planetary satellite (Io, Europa, and Titan) atmospheres with the local corotating planetary plasma (Combi et al. 1998a; Kabin et al. 1997abc, & 1998a).
3D Multiscale MHD Model with Mass-Loading The first results for applying the 3D multiscale ideal MHD model for the mass-loaded flow of Jupiter's corotating magnetospheric plasma past Io are described in our recently published paper (Combi et al. 1998a). A copy of this paper is included as part of this report. Preliminary versions of these results were presented last year by Combi et al. (1997) and Kabin et al. (1997a). The model is able to consider simultaneously physically realistic conditions for ion mass loading, ion-neutral drag, and intrinsic magnetic field in a full global calculation without imposing artificial dissipation. Io's extended neutral atmosphere loads the corotating plasma torus flow with mass, momentum, and energy. The MHD equations for mass, momentum, energy and B-field are solved on an adaptively refined unstructured Cartesian grid using a multiscale adaptive upwind scheme for MHD (MAUS-MHD) with a novel scheme for dealing in a numerically robust way with the difficulties normally encountered in implementing the div **B** = 0 condition (Powell 1994). For the work described our paper we explored a range of models without an intrinsic magnetic field for Io. Figure 8 shows a comparison of our results with particle and field measurements made during the December 7, 1995, flyby of Io, as published by the Galileo Orbiter experiment teams. For two extreme cases of lower boundary conditions at Io, our model can quantitatively explain the variation of density along the spacecraft trajectory and can reproduce the general appearance of the variations of magnetic field and ion pressure and temperature. The two cases correspond to boundary conditions at an ionosphere boundary of 150 km above the surface of Io for the plasma density and the B-field which are fixed (an absorbing boundary, allowing plasma flow and magnetic flux to pass through) and reflective (a robust non-penetrating and perfectly conducting ionosphere). The effect of a realistic ionosphere is somewhere between these extremes. The net fresh ion mass-loading rates are in the range of ~300-650 kg s^{-1}, and equivalent charge exchange mass-loading rates are in the range ~540-1150 kg s^{-1} in the vicinity of Io.

First calculations have also been performed for the interaction of Europa's atmosphere with Jupiter's plasma torus (Kabin et al. 1997b). A paper has been submitted to JGR (Kabin et al. 1998b) and is currently being revised. A copy of the submitted version is included as part of this report. As a starting point we adopted the simple atmosphere derived from the Galileo radio occulation results of Europa's ionosphere by Kliore et al. (1997). However, it is necessary to point out that there are large uncertainties about the mean of the suggested ionosphere, and the derived neutral atmosphere from Kliore et al. A given neutral atmospheric surface density and

scale height, combined with a net ionization rate provides ion mass, momentum and energy loading rates, by analogy with our Io results, and serve as a source term for the MHD equations. We used the vacuum superposition approach of Kivelson et al. (1997) as a starting point for estimating an intrinsic magnetic field for Europa and then iteratively constrained our model parameters by comparison with the Galileo magnetometer measurements (Kivelson et al. 1997) which we have obtained in numerical form from Dr. Kivelson and co-workers at UCLA. Not surprisingly the addition of mass loading, decreases the dipole moment required for an intrinsic field. So far our best results have been obtained with a model which has an ion mass loading rate to 6 x 10^{24} s^{-1}. This is below the rate suggested from the nominal mean atmosphere of Kliore et al., however, the difference is not unreasonable given the uncertainties in the scale height from 6 occulations, the values of the appropriate ionization and recombinations frequencies (factors of a few), and the simplicity of the spatial nature of our source rates. For our best model the spatial extent and magnitude of the enhancement in plasma density near Europa, compared with the nearby ambient plasma torus density, is very similar to those shown by Gurnett et al. (1998) for electron density as derived from the Galileo plasma wave measurements. The preliminary results are shown in Figure 9.

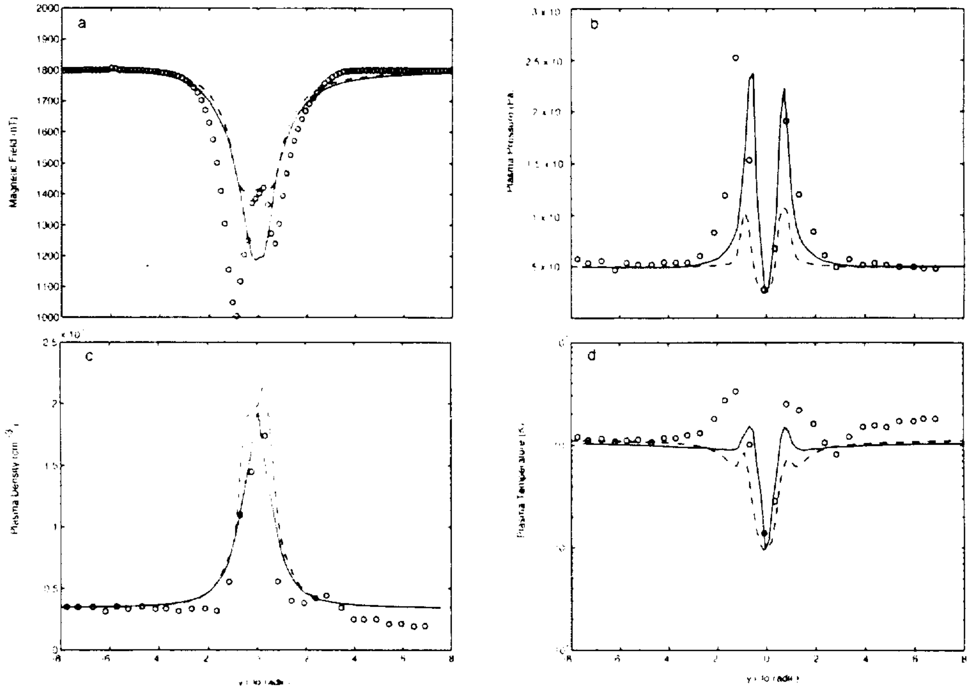

Figure 8. Comparison of MHD Mass-Loading Models with Galileo Particle and Field Measurements. The magnetic field measurements from Kivelson et al. (1996) are in (a), and the plasma density, pressure and temperature measurements from Frank et al. (1996) are in (b), (c), and (d), respectively. The solid model lines are for reflective boundary conditions and the dashed model lines are for fixed boundary conditions at an altitude of 150 km from Io by Combi et al. (1998a).

<u>Kinetic Ion-Neutral DSMC in 3D</u> (KIND_3D) The new model undertaking of this project is a 3D neutral and ion multi-species kinetic model, embedded in the multiscale Cartesian grid system structure of the 3D MHD code. The KIND_3D is based on DSMC techniques taken from an extensive repertoire of dilute gas dynamics methods in the computational fluid dynamics (CFD) literature, and already applied to cometary and Earth polar wind applications by our group. For the original CFD applications see, for example, the monograph by Bird (1994). The method enables a kinetic calculation of neutral and ion gas species to be made, either separately, iteratively, or ultimately together, in a satellite or tenuous planetary atmosphere, ionosphere, and exosphere/corona. Results from either MHD and DSMC models can then easily serve as inputs

to the other, or ultimately the models can be run intimately. Work in Michigan on kinetic modeling of neutral and ionized gases using particle simulation codes began in the last few years in applications for multispecies 2D axisymmetric modeling of the non-equilibrium flow of the neutral coma (Combi 1996), with non-LTE radiational cooling and UV heating, and for multispecies 1D-spherical modeling of the Earth's polar wind flow (Miller & Combi 1994; Miller et al. 1995). A description ofthe KIND_3D model for Io was presented at the 1998 Spring AGU meeting in Boston (Bauske & Combi 1998a). First calculations were presented at the 1998 Fall AGU meeting in San Francisco (Bauske & Combi 1998b). For these results we ran a single species neutral model for an atmosphere produced by a combination of sublimation and two volcanoes. A major modeling paper, documenting KIND_3D and presenting first applications to Io is being prepared for submission during the early part of the follow-on grant which has already been approved for funding by the Planetary Atmospheres.

The Direct Simulation Monte Carlo (DSMC) method has a long history (Bird 1994) of application in areas as diverse as study of hydrodynamic shock structures, calculation of low-density, hypersonic flows around spacecraft, and simulations of plasma reactors for microelectronics manufacturing. Originally, the method was used for simulations in the (neutral gas) transition regime, where the mean free paths of particles are too large for traditional continuum CFD methods to be applicable. Because collisions are important, free molecular simulations are also not appropriate. Therefore, individual particles are simulated as they move around within a grid, colliding with other particles and with solid objects. Macroscopic properties, such as density and temperature are computed by appropriate averaging of particle masses, positions, velocities, and internal energies. Surface properties are calculated from the momentum and energy exchanges with the surface, also allowing for chemical reactions. In the collisionally thick limit an appropriate DSMC calculation asymptotically approaches the same results as a hydrodynamic calculations such as the Euler or Navier-Stokes formulations.

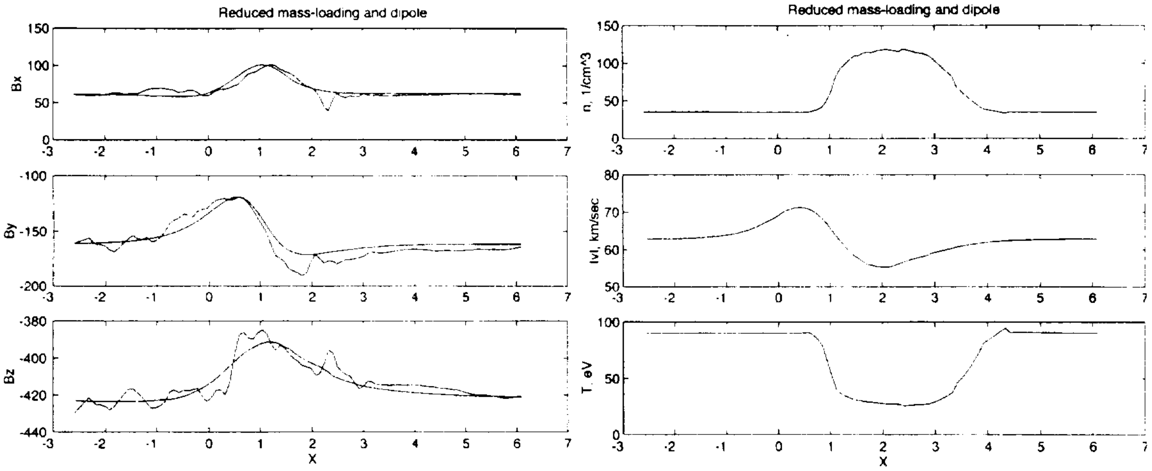

Figure 9. MHD Model with Mass Loading for Galileo E4 Flyby of Europa. At the left are shown the 3 components of magnetic field compared with the Galileo magnetometer measurements. At the right are shown plots of plasma density, velocity, and temperature. The model has fixed boundary conditions at the surface, mass-loading, ion-neutral charge exchange, recombination, and an intrinsic magnetic dipole field with components (0, 71, -64) R_E^3 nT. Results are from Kabin et al. (1997b).

Many applications today are in dilute, but collisionally dominated particle regimes where the particles have nearly thermal collision energies and the ionization ratio is very low. In particle oriented plasma physics the Particle In Cell (PIC) method is used, usually in order to study collision free plasmas (for a review see Winske & Omidi, 1996) and therefore particle collisions were included only in special cases (see, e.g., Wang et al., 1996 and references therein). With the hybrid model we explore a new way to bridge the gap between the collision dominated and the collision free regime in partially ionized plasmas and we also extend the

range of the DSMC method towards the higher particle energies usually encountered in planetary ionospheric and magnetospheric plasma environments (hundreds of eV/amu).

We divide the spatial region simulated by the model into 'inner' and 'outer' domains. Inner domains may contain a whole planetary obstacle and a fraction of its surrounding atmosphere / exosphere / plasma environment. Both types of domains are simulated using the MHD approach in order to obtain the magnetic field. In inner domains we embed the multispecies KIND_3D model which allows detailed simulations of the chemistry and of surface interactions. Each domain is adaptively refined and therefore contains multiple cells in various sizes to match requirements specific to the domain. The MHD parts, e.g., may have high resolution at a planetary bow shock, while the DSMC parts are able to simulate the outflow of hot gases due to volcanic activity from specific surface regions above Io. At domain boundaries the MHD flow entering a DSMC domain is converted to entering particles by sampling from the particle distribution.

Lutisan (1995) compared several variants of the DSMC method and found the No Time Counter technique (NTC) of Bird (1994) and the Null-Collision technique (Koura, 1986, 1989, 1998) to be among the fastest and most reliable ones. We chose the NTC method for its simplicity and its closeness to classic kinetic theory. In contrast to Bird, we allow a particle to undergo several changes of its internal energy per time step, thus allowing for fewer particles per cell and larger time steps where necessary.

Apart from higher energies than in usual DSMC calculations, we also face the need to simulate regions with orders of magnitude differences in density. The model chemistry will contain a variety of different species including trace species. Our basic ideas to approach these problems numerically are the use of weighted species groups and of a regular spaced subgrid within each cell of the adaptive grid structure. Usually every particle in a simulation cell represents a fixed number of real particles. This leads to problems if one species is underrepresented since a large number of samples is necessary to get reasonable statistics for this species. A weighting method artificially changes the species value in order to allow for more simulation particles. In collisions of species with different weights additional means must be undertaken to conserve the overall momentum and energy balance at least on average. For binary Coulomb collisions and a completely different particle selection method Takizuka & Abe (1977) suggested an algorithm which was later improved by Miller & Combi (1994).

KIND_3D has added functionality beyond the basic algorithms suggested by Bird (1994) to account for chemical reactions and collisions with large inelastic cross sections. We developed a corresponding weighting scheme which allows for trace species. Basically the number of selections for collisions is now recalculated every time a species type changing collision (reaction, ionization, etc.) occurs and the collision iteration proceeds as long as there are selections to work on. Our NTC variant employs a data structure which allows fast addition and deletion of particles without need to loop over all particles for reindexing after such collisions. The weighting scheme determines the number of selections and the acceptance of the collisional momentum, energy, and type change for the higher weighted particle. Weighting is also used to keep the numbers of simulation particles in different density regimes approximately equal and at a computationally feasible number. Care is taken of particles moving from one cell to another with a different cell weight. Particles with higher weights are replicated, and particles with lower weights are deleted with a probability set by the ratio of the particle weight to the cell weight.

Now we describe the current status of the model, as of this writing. A single processor version of the hybrid model is specified for Io. Particle species include O, S, O_2, S_2, SO, SO_2, SO_3, and the corresponding ions. We account for $O^+(^4S)$, $O^+(^2D)$, $O^+(^2P)$, $S^+(^4S)$, $S^+(^2D)$, $S^+(^2P)$ as separate species for photoionization and take care of the excess energies which contribute to the electron energies for ionization, to the particle energies for dissociation, and to UV heating. Energy dependent solar photo rates and the solar photon fluxes are taken from Huebner et al. (1992). Particle trajectories are calculated either assuming the adiabatic particle motion in the corotating magnetic field of Jupiter--the gyrotropic approximation--(Northrop & Hill, 1983; Northrop & Birmingham, 1982) or by direct numerical integration of the momentum equations. The plasma is assumed to be quasi neutral and as a first approximation the electron temperature

given by the scaled MHD plasma temperature. At a later stage we will calculate electrons independently, for example, using the method of Harvey & Gallis (1996).

Insufficient knowledge about the energy dependence of collision cross sections is a major problem in space physics. KIND_3D includes the variable soft and hard sphere molecule models (Bird 1981; Koura & Matsumoto 1991, 1992) for elastic cross sections. For small particle energies Bird (1994) suggests schemes to convert temperature dependent reaction rate coefficients to steric factors. We are extending these and the elastic cross sections towards higher energies with theoretical approximations from Johnson (1990) and will make use of accurate calculations from the astrophysical community (e.g., the Opacity project, Cunto et al. 1993) to get a fast and reliable chemical reaction network for high collision energies. An up-to-date atomic/molecular database will be maintained.

In DSMC methods dissociation and vibrational excitation during molecular collisions are coupled. Whenever a redistribution of vibrational energy during a collision occurs, there is some probability for dissociation if the available energy exceeds the dissociation threshold. Calculations of these effects are usually based on the statistical collision model of Borgnakke & Larsen (1975) and its improvements made by a number of successors. As a first step, we use the method suggested by Bird (1994) and Carlson & Bird (1995) for molecular collisions. Here discrete vibrational energy levels are given by a harmonic oscillator potential. The energy levels are extrapolated beyond the dissociation level and a probability is calculated in order to decide wether the molecule dissociates or not. A new scheme was suggested by Lord (1998) which does not need the extrapolation and uses a more appropriate anharmonic oscillator potential. We will implement it in a second step. Cooling, or radiation escape losses are the other half of accounting for internal rotational energy transfer in collisional processes. Strobel et al. (1994) accounted for non-LTE radiative escape in the context of their 1D diffusive photochemical model. Non-LTE radiative escape is handled in DSMC as a by-product of the accounting of internal energy, as described for water IR cooling in a cometary coma DSMC model (Combi 1996).

With the DSMC method a lower boundary can be adopted either from somewhat below a defined exobase at some altitude above the surface, or at the surface (as is the case possibly at locations on the night side of Io and/or far away from volcanoes, or for Europa). Particle surface interactions are currently restricted to elastic collisions or absorption. One of the next steps among others will be the implementation of the Cercignani-Lampis surface interaction model (Lord, 1991). Depending on the obstacle chosen for the MHD part, the lower boundary is not always equal to the planetary surface. In this case incoming particles will be sampled from exospheric fluxes which are specified depending on surface conditions.

KIND_3D provides a self-consistent approach to modeling chemistry, radiative effects, and kinetic effects important in the interaction of the extended neutral atmosphere and ionosphere with the outer impinging magnetized plasma flow. The advantage of having KIND-3D embedded in the MHD multiscale adaptive grid means that both parts of the problem can be solved using the most physically reasonable but yet still computationally efficient methods.

REFERENCES

Arpigny, C. , Rauer, H., Manfroid, J. , Hutsemekers, D., Jehin, E., Crovisier, J., & Jorda, L. 1998 A&A 334, L53

Ballester, G. E., et al. 1997. BAAS 29, 980.

Ballester, G., McGrath, M., Strobel, D., Zhu, X., Feldman, P. & Moos, H.W. 1994. Icarus 111, 2.

Barker, E., A. Cochran, & W. Cochran. 1998. Earth, Moon & Planets (in press).

Bauske, R. & Combi, M. 1998. *Eos Transactions, AGU*, **79**, S200, 1998a.

Bauske, R. & Combi, M. 1998. *Eos Transactions, AGU*, **79**, F551, 1998b.

Bauske, R., A. Nagy, T. Gombosi, D. De Zeeuw, K. Powell, & J. Luhmann. 1998. JGR 103, 23625.

Belton, M. J. S. et al. 1996. Science, 274, 377.

Bigg, E.K., 1964, Nature, 203, 1008.

Bird, G. A. 1981. Progr. Astro. Aero.; Rarefied Gas Dynamics, 74, 239; 1993. Progr. Astro. Aero, 185.

Bird, G.A. 1994. *Molecular Gas Dynamics and the Direct Simulation of Gas Flows*, Clarendon, Oxford

Borgnakke, C., & P. S. Larsen. 1975. Journ. Comput. Phys., 18, 405.

Brown, M.E. & R.E. Hill. 1996. Nature 380, 229.

M.E. Brown, A.H. Bouchez, H. Spinrad, and A. Misch. 1998. Icarus (in press)

Carlson, A., & G. Bird 1995. In Rarefied Gas Dynamics, ed. I. Harvey & R. Lord, Clarendon, Oxford.

Cloutier, P.A., R.E. Daniell, Jr., A.J. Dessler, & T.W. Hill, 1978, Astrophys. Space Sci. 55, 93.

Combi, M. 1994. Astron. J. 108, 304.

Combi, M. 1996. Icarus 123, 207.

Combi, M., DiSanti, M.A., & Fink, U. 1996. Asteriods, Comets, Meteors, July 1996, Versailles, France.

Combi, M., DiSanti, M.A., & Fink, U. 1997, Icarus 130, 336.

Combi, M., Kabin, K., Gombosi, T., DeZeeuw, D., Powell, K. 1997. Ann. Geophys. 15 (III), 824.

Combi, M., Kabin, K., Gombosi, T., DeZeeuw, D., Powell, K. 1998a. JGR 103, 9071.

Combi, M., Kabin, K., DeZeeuw, D., Gombosi, T., Powell, K. 1998b. Earth, Moon & Planets (in press).

Combi, M.R., & W.H. Smyth. 1988a ApJ 327, 1026; 1988b ApJ 327, 1044.

Cunto, W., C. Mendoza, F. Ochsenbein, and J. J. Zeippen. 1993. TOPbase A&A 275, L5

Cremonese, G. et al. Astrophys. J. 154, 327.

Finson, M.L. & Probstein, R.F. 1968a, Astrophys. J. 154, 327: 1968b, ApJ 154, 353.

Fitzsimmons, A. and the European Hale-Bopp Team. 1997. IAU Circ. 6634.

Fulle, M., S. Bosio, G. Cremonese, S. Cristaldi, W. Liller, & L. Pansecchi. 1993. A&A, 272, 634.

Fulle, M., Cremonese, G., and Böhm, C.. 1998, A. J. 116, 1470.

Fulle, M., H. Mikuz, & S. Bosio. 1997. A&A 324.

Goertz, C.K. 1980. JGR 85, 2949.

Goldreich, P. & D. Lynden-Bell, Io, 1969, ApJ, 156, 59.

Gombosi, T., D. L. DeZeeuw, R.M. Häberli, & K.G. Powell. 1996. JGR 101, 15233.

Grün, E. & Jessberger, E. 1991, In the *Physics and Chemistry of Comets*. Ed. Walter Huebner, Springer-Verlag, New York, p. 113-176

Gurnett, D.A., W.S. Kurth, A. Roux, S.J. Bolton, E.A. Thomsen, J.B. Groene. 1998. GRL 25, 237.

Häberli, R. , M. Combi, T. Gombosi, D. De Zeeuw, & K. Powell. 1997a. Icarus, 130, 373.

Harvey, J. K. & M. A. Gallis. 1992. Prog. Astronaut. Aeronaut., 224.

Hall, D., D.F. Strobel, P.D. Feldman, M.A. McGrath, & H.A. Weaver. 1995. Nature 373, 677.

Hill, T.W., A.J. Dessler, & C.K. Goertz, 1983, In *Physics of the Jovian magnetosphere*, ed. by A.J. Dessler, Cambridge University Press, Cambridge.

Huebner, W.F., Keady, J.J. & Lyon, S.P. 1992, Astrophys. Sp. Sci. 195, 1.

Ip, W.-H. 1996. Icarus 120, 317.

Johnson, R. E., Energetic Charged Particle Interactions with Atmospheres and Surfaces, Springer-Verlag, Berlin Heidelberg, 1990.

Kabin, K., M. Combi, T. Gombosi, D. DeZeeuw, & K. Powell. 1997a. Spring AGU, SM52A-07.

Kabin, K., M. Combi, T. Gombosi, A. Nagy, D. DeZeeuw & K. Powell. 1997b BAAS, 29, 985.

Kabin, K. T. Gombosi, D. DeZeeuw, K. Powell, & P. Israelovich. 1997c. Fall AGU, P32A-12

Kabin, K., T. Gombosi, D. DeZeeuw, & K. Powell. 1998a. JGR (in preparation).

Kabin, K., M. Combi, T. Gombosi, A. Nagy, D. DeZeeuw, K. Powell, & M. Kivelson. 1998b. JGR (submitted).

Kawakita, H. and Fujii, M. 1998. ApJ 502, L185.

Keller, H.U., Marconi, M.L., & Thomas, N. 1990, A&A 227, L1.

Kivelson, M. et al. 1997. Science 276, 1239.

Kliore, A., D. Hinson, F. Flasar, A. Nagy, & T. Cravens. 1997. Science 277, 355.

Konno, I, Huebner, W.F., & Boice, D.C. 1993, Icarus 101, 84.

Koura, K. 1986. Phys. Fluids, 29, 3509; 1989. Prog. Astronaut. Aeronaut., 117, 25; 1989. Prog. Astronaut. Aeronaut., 117, 25; 1998. Computers Math. Applic., 35, 139.

Koura, K. & H. Matsumoto. 1991. Phys. Fluids A, 3, 2459; 1992. Phys. Fluids A, 4, 1083.

Kumar, S. & D. Hunten. 1982. In Satellites of Jupiter, ed. D. Morrison, Univ. Arizona Press, Tucson, 782

Lara, L., & W. Ip. 1997. Icarus 130, 16

Lellouch, E. 1994. Icarus, 108, 255; 1996. Icarus, 124, 1.

Lellouch, E., M. Belton, I. de Pater, G. Paubert, S. Gulkis, & T. Encrenaz. 1992. Icarus 98, 271.

Linde, T., T. Gombosi, P. Roe, K. Powell, D. DeZeeuw. 1998. JGR, 103, 1889.

Linker, J., M. Kivelson, & R. Walker. 1988. GRL 15, 1311; 1989. GRL 16, 763; 1991. JGR 96, 21037.

Lord, R. G. 1991. In Rarefied Gas Dynamics (ed. A. Beylich), p. 1427, VCH Verlagsgesellschaft mbH, Weinheim, Germany

Lord, R. G. 1998. Phys. Fluids, 10, 742.

Lutisan, J. 1995. Molecular Simulation, 189.

McGrath, M.A. & R.E. Johnson. 1987. Icarus 69, 519.

Miller, R. H., & M. R. Combi. 1994. Geophys. Res. Lett., 21, 1735.

Miller, R., C. Rasmussen, M. Combi, T. Gombosi, D. Winske. 1995. JGR 100, 23901.

Moreno, M.A., G. Schubert, J. Baumgardner, M.G. Kivelson, & D.A. Paige 1991. Icarus 93, 63.

Northrop, T. G. & T. J. Birmingham. 1982. J. Geophys. Res., 87, 661.

Powell, K. G. 1994. ICASE Rep. 94-24, Inst. for Comput. Appl. in Sci. and Eng., Langley, VA.

Rauer, H., C. Arpigny, J. Manfroid, G. Cremonese, & C. Lemme. 1998. A&A 334, L61.

Sauer, J., D. Strobel, & F.M. Neubauer. 1998. JGR (submitted)

Schneider, N.M., D.M. Hunten, W.K. Wells, A.B. Schultz, & U. Fink, 1991, ApJ 368, 298

Schneider, N.M., W.H Smyth, and M.A. McGrath. 1989. NASA Spec. Publ. NASA SP-494, 75.

Sekanina, Z. 1981. A.J. 86, 1741.

Sekanina, Z. and Larson, S. 1984. A.J. 89, 1408.

Sieveka, E. M. & R. E. Johnson. 1985. JGR 90, 5327

Smyth, W. H. & M. R. Combi. 1997. Icarus 126, 58.

Strobel, D. F., X. Zhu, & M.E. Summers. 1994, Icarus 111, 18.

Summers, M.E., D.F. Strobel. 1996. Icarus 120, 290.

Takizuka, T., & H. Abe. 1977. Journ. Comput. Phys., 25, 205.

Trauger, J., K. Stapelfeldt, G. Ballester, J. Clarke, and WFPC2 Science Team. 1997. BAAS 29, 1002.

Wang, J., R. Biasca, and P. C. Liewer. 1996. JGR 101, 371

Wilson, J.K., J. Baumgardner, & M. Mendillo. 1998. GRL 25, 225.

Winske, D., & N. Omidi. 1996. JGR, 101, 17287.

Wolf-Gladrow, D.A., F.M. Neubauer, & M. Lussem. 1978. JGR (Space) 92, 9949

Wong, M. C. & R.E. Johnson. 1995. Icarus 115, 109, 1996a JGR 101, 23243; 1996b, JGR 101, 23255.

Yung. Y. & M. McElroy. 1977. Icarus 30, 97.

Sent - 7/1/45

On Europa's magnetospheric interaction: an MHD simulation

K. Kabin, M. R. Combi, T. I. Gombosi, A. F. Nagy, D. L. DeZeeuw,

K.G. Powell
The University of Michigan, Ann Arbor, MI 48105

Short title:

Abstract. The three-dimensional interaction of Europa with the Jovian magnetosphere is modeled using a complete set of ideal magnetohydrodynamic (MHD) equations. The model accounts for exospheric mass-loading, ion-neutral charge exchange, recombination and a possible intrinsic dipole magnetic field of Europa. The single fluid MHD equations are solved using a modern finite-volume higher-order Godunov-type method on an adaptively refined unstructured grid, which allows a detailed modeling of the region near Europa, while still resolving both the upstream region and the satellite's wake. The magnetic field and plasma density measured during Galileo's E4 flyby of 19 December 1996 are reproduced reasonably well in the simulation. The general structure of the plasma flow past Europa and bounds on the total mass-loading and ion-neutral charge exchange rates are discussed.

Introduction

Jupiter's satellite Europa is located deep inside Jovian magnetosphere on the outskirts of the Io plasma torus. Europa has a water ice surface which is constantly bombarded by energetic ions. Atoms and molecules sublimated from the ice surface form a thin gravitationally bounded atmosphere. Suggestions that an oxygen atmosphere should accumulate above Europa's water ice go back over 20 years [*Wu et al.*, 1978; *Kumar and Hunten*, 1982]. Atomic oxygen emissions from Europa was detected using the Hubble Space Telescope (HST) by *Hall et al.* [1995], who estimated the column abundances of molecular oxygen to be $\sim 1.5 \times 10^{15}\ cm^{-2}$ and a surface pressure $\sim 10^{-11}$ bar. These values are consistent with the equilibrium ice sublimation model, described by *Johnson* [1990].

Brown and Hill [1996] reported the discovery of sodium around Europa. Their conclusion is that this sodium originated from Europa's surface. Sodium emissions are visible up to 25 Europa radii. Although sodium is a minor species, it should trace the distribution of dominant species. Thus, in addition to the exponentially decaying bound part there may be a large corona with an algebraic radial dependence. The best fit to the observations, performed by *Brown and Hill* [1996] favors $\sim r^{-2.5}$ distribution of the neutral density (r is the distance from the center of Europa), which is somewhat less steep than the otherwise similar exponent ($\sim r^{-3.5}$) for Io sodium [*Schneider et al.*, 1991]. A model for hot oxygen corona of Europa was suggested by *Nagy et al.* [1998].

Solar photoionization and particle impact ionization should produce an ionosphere around Europa. Galileo's flybys on 19 December 1996 (E4) and on 20 (E6a) of February 1997 were used for radio occultation and reconstruction of ionosphere profiles by *Kliore et al.* [1997]. The typical distance between Galileo and Europa was about 1,500 km during the ingresses and about 4,000 km during the egresses. An additional distant radio occultation (E6b) took place on 25 of February 1997 when Galileo was about 2.8×10^6 km from Europa. The latitudes of the occultations were close to $-2°$, $-24°$ and $-14°$

respectively. These three occultations gave six ionospheric profiles which were averaged to give a plasma scale height of 240-440 km, with the maximum electron density of 10^4 cm^{-3} near the surface. From these measurements *Kliore et al.* [1997] inferred a neutral scale height of 120 km and a surface neutral density of 10^8 cm^{-3}. Integrating this gives a column abundance of about 10^{15} cm^{-2}, which is consistent with the results of *Hall et al.* [1995]. However, there are very large uncertainties involved in the deduction of atmospheric densities from the ionospheric profile. It is based on just six occultations with significantly different latitudes and an impact ionization rate which was most likely too low, just to mention two potential difficulties. One can see on figures in *Kliore et al.* [1997] that the electron density, obtained from the inversion of the radio-occultation data, often becomes negative. Thus, we will use the results of *Kliore et al.* [1997] as a starting guess, which will be modified, rather than a prescribed input for our model.

The closest approach distance during Galileo's flyby of 19 December 1996 was 688 km above the surface of the satellite. Successful magnetic field measurements were obtained during this flyby [*Kivelson et al.*, 1997]. Near the closest approach a perturbation of ~ 50 nT was observed, which was clearly not a random disturbance, but a coherent magnetic signature associated with Europa. *Kivelson et al.* [1997] explained the magnetic signature of Europa by assuming an intrinsic dipole field. Based on a magnetostatic vacuum superposition they have suggested an upper limit for Europa's dipole which produces a maximum surface magnetic field magnitude of 240 nT. In more recent papers *Kivelson et al.* [1998] and *Khurana et al.* [1998] suggested an induced dipole model as an explanation for at least part of the observed magnetic signature.

During the E4 and E6a flybys Galileo plasma wave instrument observed strong whistler-mode noise. From the measured upper hybrid resonance frequency and the local electron plasma frequency *Gurnett et al.* [1998] inferred the electron density. They observed an electron density enhancement of 30 to 100 cm^{-3} close to Europa. Unfortunately, the average charge state of the plasma ions is not known very well. If we assume that it is about 2, then the results for the electron density of *Gurnett et al.* [1998] are close to the older model of Io plasma torus of *Smyth and Combi* [1988]. Thus, the Galileo measurements [*Gurnett et al.*, 1998] imply a plasma density enhancement in the wake behind Europa 2-2.5 times the upstream values.

While there is a wealth of models for ionospheres and magnetospheres of major planets and satellites, Europa until very recently has escaped the attention of the modelers. Prior to the Galileo mission very little was known about Europa, which resulted in only very crude models of the environment of the satellite.

Wolff and Mendis [1983] considered the effects of the Jovian magnetosphere on the icy surface of Europa, Ganymede and Callisto; however they did not perform any simulation of plasma flow around the satellites. A decade later, *Schreier et al.* [1993] constructed a "zero-dimensional" model of the Europa plasma torus. The focus of their work was the balance of the chemical species rather than plasma dynamics. Europa's magnetospheric interaction was described by *Ip* [1996] from a physical point of view, while the main object of the paper was Europa's exosphere. Some of the parameters used by *Ip* [1996], such as an acoustic Mach number for the upstream plasma of $M = 2.7$, seem to be inconsistent with our current understanding of Europa's space environment.

Recently, *Saur et al.* [1998] developed a more sophisticated model for Europa's magnetospheric interaction. However, the emphasis of their work was on the neutral atmosphere, for which they obtained some important results that agree with the observations of *Hall et al.* [1995]. At the same time, *Saur et al.* [1998] did not treat the magnetic field self-consistently, which diminishes the value of their results for the understanding of plasma flow around Europa and makes impossible an attempt to reproduce Galileo's magnetometer data from their model.

In a theoretical paper *Neubauer* [1998] considered general properties of sub-Alfvénic interaction of Galilean satellites with Jovian magnetosphere. He discussed the qualitative effects of ion pick-up, ion-neutral collisions and intrinsic magnetic field on the plasma flow past a satellite and described several possible types of magnetospheric interaction. The quantitative understanding of the details of this interaction requires global three-dimensional MHD modeling. This is the main objective of our work; we also compare our model results with Galileo's magnetometer and plasma wave instrument measurements.

Model

We describe the plasma environment of Europa with the single fluid ideal MHD equations. The conservative dimensionless form of these equations is

$$\frac{\partial}{\partial t}\begin{pmatrix} \rho \\ \rho\mathbf{u} \\ \mathbf{B} \\ E \end{pmatrix} + \nabla\cdot\begin{pmatrix} \rho\mathbf{u} \\ \rho\mathbf{u}\mathbf{u} + p^{*}\mathbf{I} - \mathbf{B}\mathbf{B} \\ \mathbf{u}\mathbf{B} - \mathbf{B}\mathbf{u} \\ \mathbf{u}(E + p^{*}) - \mathbf{B}(\mathbf{B}\cdot\mathbf{u}) \end{pmatrix} = \mathbf{S}$$

where $p^{*} = p + B^2/2$, $E = \rho u^2/2 + p/(\gamma - 1) + B^2/2$ and $\mathbf{I}$ is a unit 3×3 matrix. The source term, appearing on the right-hand side of the system has the form

$$\mathbf{S} = \begin{pmatrix} \dot{M} + \chi(\rho_0^2 - \rho^2) \\ -\dot{M}\eta\mathbf{u}\rho \\ 0 \\ -\eta\dot{M}(\rho u^2/2 + p/(\gamma - 1)) \end{pmatrix}$$

Here $\dot{M}$ is the local mass loading term (proportional to the neutral density), η is the ion-neutral collision momentum-energy transfer rate per unit volume, χ is the recombination rate and ρ_0 is the upstream plasma density. The derivation of these source terms from the Boltzmann equation can be found in *Gombosi* [1991]. They are very similar to those used by *Combi et al.* [1998]. The only difference is that in the present Europa model we included ion recombination. It is naturally treated as a second order reaction. Ion loss from recombination is accompanied by a production term whose role is to keep perfect balance for the upstream conditions. In our simulation we used $\chi = 8 \times 10^{-8}\ cm^3 s^{-1}$ based on *Torr and Torr* [1985]. This is the same value as used by *Kliore et al.* [1997]. This parameter was not adjusted through the simulation, but kept constant.

Europa is approximated by a sphere 1500 km in radius. The boundary conditions on the surface were imposed by utilizing cut cells [*DeZeeuw and Powell*, 1993], which allow second order (piecewise linear) reproduction of the surface geometry. In our simulations we have studied a number of possible boundary conditions on Europa's surface.

The simplest and the most numerically natural type of the boundary conditions is a perfectly conducting solid sphere. Under these assumptions, no plasma flow or magnetic flux are allowed to penetrate the body. However, this approach might not be physically appropriate. The conductivity of Europa's ionosphere and surface ocean layer can be very high, but still finite, and thus, over millions of years of the planet existence, the external magnetic field would still diffuse into the planet interior.

We can assume completely "absorbing" boundary conditions for Europa. The reason to allow the plasma to penetrate the surface of the satellite can be the following. Europa is surrounded by a neutral atmosphere, which is relatively dense near the surface. An impinging ion is likely to be lost in it, rather than diverted around the planet. Absorbing boundary conditions could also be explained by a recombination rate that becomes larger in the lower neutral atmosphere. A consistent model of ion-neutral interaction requires an ionosphere model for Europa to be coupled with the MHD model of the magnetosphere. However, this kind of numerical simulation is beyond our present capabilities. The models of a "superconducting sphere" and an "absorbing sphere" are clearly the two extremes bracketing reality.

The system of MHD equations is solved using a higher order Godunov-type finite volume method on an unstructured Cartesian grid with adaptive mesh refinement. The cell structure ("octree") provides very good resolution in the interaction region, while allowing the total simulation box to be very large. The numerical aspects of the model and grid structure are described in *DeZeeuw and Powell* [1993], *Powell* [1994], *Powell et al.* [1995]. Convergence to the steady-state was accelerated by local time-stepping and optimal residue smoothing [*van Leer et al.*, 1989]

The reference frame we use throughout this article is a Cartesian system of reference in which the X axis is parallel to the corotation direction, Z axis is parallel to the Jovian spin axis and Y completes the right-handed system.

The upstream parameters for Europa are not known exactly, so the input for our model was based on the Galileo magnetic field measurements [*Kivelson et al.*, 1997] and on a model of the Io plasma torus [*Smyth and Combi*, 1988] derived from the Voyager 1 plasma data. The following is a table of the parameters which we used:

-plasma density 35 cm^{-3}

-plasma temperature 90 eV

-plasma speed 90.3 km/s (corotational value)

-mean molecular mass 24 amu

-ratio of the specific heats 1.67

-a uniform tilted Jovian magnetic field with components in the Cartesian frame of reference (63, -162, -422) nT (tilted 8° with respect to the upstream velocity). These parameters correspond to a sonic Mach number $M = 0.7$ and Alvfénic Mach number $M_A = 0.25$.

Results and discussion

We have investigated a number of boundary conditions, mass-loading functions, ion-neutral charge exchange coefficients and intrinsic dipole fields trying to reproduce the Galileo measurements. In order to perform the comparison between the measurements and the model we have removed the global trend (constant linear slope) from the original magnetometer data [*Kivelson et al.*, 1997]. It is straightforward in principle to incorporate a constant slope (or even an arbitrary coordinate dependence) into the initial conditions for the magnetic field, however most of the large scale structure of the magnetic field is related to a time-dependent effect. This effect includes both Galileo orbital motion and Jupiter rotation around its spin axis which is 10° different from its dipole axis. Time-accurate calculation of the Galileo flyby is beyond our current computational capabilities and is not the purpose of the current paper.

We show by the dashed line in figure 1, as a baseline, the results of vacuum superposition of a dipole field and Jupiter's magnetic field, approximated by a constant vector. To get the best fit we have minimized the L_2 norm of the difference between the magnetostatic model and data. The resulting value for the dipole is (-0.1, 86., -108.) nT R_E^3, which gives a magnetic field intensity of 270 nT at the surface at the magnetic pole. This dipole is within 15% of the value suggested by *Kivelson et al.* [1997].

The numerically simplest type of boundary condition is a perfectly conducting Europa. This type of boundary conditions was one of the two bracketing cases for Io used by *Combi et al.* [1998]. Figure 1 shows by dotted line the results of a simulation with this kind of boundary condition. In this case we did not use any mass-loading, but tried to fit the magnetic field measurements by changing the intrinsic dipole value. Our best results were obtained with a dipole moment of (16, 42, 57) R_E^3 nT. This fit is no better than the magnetostatic superposition, but it has an important message – the dipole moment vector has almost reversed its direction as compared with the vacuum superposition. This tells us that the problem is very sensitive to the boundary conditions.

The major processes in Europa's upper atmosphere leading to the production of new ions are photoionization and electron impact ionization of atmospheric neutrals. *Kliore et al.* [1997] estimated that the ionization frequency due to impacts is three times larger than that due to photons. This means that the ion production rates are likely to be non-spherically symmetric and perhaps weighted toward the ram side. The actual angular dependence of the production rates is, however, unknown and cannot be inferred from available data.

We started with the total mass-loading of $1.1 \times 10^{26}\ s^{-1}$ distributed spherically symmetrically with an ion scale-height of 240 km, which are the parameters suggested by *Kliore et al.* [1997]. With mass-loading, ion-neutral charge exchange and recombination included we fail to obtain any reasonable fits to the data using a superconducting sphere for Europa, but had to switch to completely absorbing boundary conditions. Even with absorbing boundary conditions, the disturbance of the magnetic field in our model was too large and did not seem to have the correct character. Thus, we reduced the total mass-loading together with the scale-height. Our best fit – figure 1, continuous line – was obtained with a total mass-loading of $6 \times 10^{24}\ s^{-1}$ and an ion scale-height of 120 km. We assumed an ionization frequency of $1 \times 10^{6}\ s^{-1}$ (same as *Kliore et al.* [1997]) and an ion-neutral charge exchange parameter of $\eta = 2.8 \times 10^{-8}\ cm^3 s^{-1}$. These parameters are significantly different from those recommended by *Kliore et al.* [1997], but we point out the very large uncertainties that appear in their evaluation of the "best ionospheric profile". A theoretical calculation Europa's exosphere by *Nagy et al.* [1998] somewhat modified the earlier result of *Kliore et al.* [1997] and estimated the total escape rate of hot oxygen as $8.8 \times 10^{25}\ s^{-1}$. Even this estimation is still significantly larger than our value for the total mass loading. In this simulation we used the dipole moment of (0,71,-64) R_E^3 nT which is approximately 40% smaller than the value from the vacuum superposition. As one can expect, the mass-loading diminishes the required value of the intrinsic magnetic field. It does not seem feasible yet to set a lower limit different from zero on Europa's magnetic field, because the details of the neutral atmosphere interaction with Jupiter's plasma torus are very uncertain and the boundary conditions have an important effect on the conclusions about Europa's intrinsic magnetic field. It is quite possible that the mass-loading functions more complicated than the spherically symmetric ones used in this work can be responsible for the observed magnetic field signature. The future availability of plasma instrument data can significantly improve the precision of the model, since it will be possible to compare plasma densities and temperatures along the Galileo trajectory, which are most directly affected by the mass-loading parameters. The plots of plasma density, speed and temperature based on our model are shown in figure 2 and are in qualitative agreement with the measurements of *Gurnett et al.* [1998].

The general structure of the plasma flow around Europa can be inferred from figures 3, 4 and 5. The density contours go from 40 cm^{-3} to 120 cm^{-3} with increments of 10 cm^{-3}. Qualitatively, the density in the XY and XZ planes are similar, but one can see that in XZ plane the plasma tail behind Europa is much broader. This is a typical MHD effect explained by the anisotropy of the plasma flow with respect to the velocity direction. The magnetic field is mostly along the Z axis, which favors the flow around the obstacle in XY plane and hinders the flow in XZ plane. The asymmetry between the two perpendicular slices of the three-dimensional solution is even more prominent in the velocity magnitude. The speed contours go from 88 km/s to 94 km/s in figure 4 and to 91 km/s in figure 5 in increments of 3 km/s. The lines with arrows are plasma stream-lines. They are not bent as much as they would be in the case of stronger obstacle, such as a conducting sphere. It is interesting to point out that the curvature of the stream-lines is different in the two cross-sectional planes due to the three-dimensional character of the flow. The speed increases faster and to a higher value along the Y axis than along the Z axis, which explains why density tail is broader in the Z direction than in the Y direction.

Conclusions

In this paper we presented the results of a three-dimensional MHD simulation of Europa magnetospheric interaction. Even in our relatively simple model we were able to reproduce the main features of the Galileo magnetometer and plasma wave instrument measurements. Although we have used an intrinsic dipole moment for Europa in our model, it is possible that the satellite does not have one, and its magnetic signature can be explained without such a field. Many non-MHD effects, such as finite gyro-radius radius of ions, multi-fluid interaction, physical resistivity and viscosity, deviations from thermal equilibrium, cannot be self-consistently incorporated into our model yet. In our present model we have not included the effect of coronal-type mass-loading, which may be inferred from the measurements of *Brown and Hill* [1996] and the model calculations of *Nagy et al.* [1998]. It is clear, that this part of Europa's atmosphere is very thin, and from our experience with the Io model [*Combi et al.*, 1998] the fine details of the mass-loading process are not overly important. In the future, however, the mass-loading far from Europa might play a critical role in interpreting the results of later Galileo flybys - *[Kivelson, private communication]*. Study of these effects and comparison with coming Galileo data will be the basis of future work.

Acknowledgments. We thank Dr. M. G. Kivelson and the Galileo Magnetometer team for providing us the electronic versions of the data and many useful discussions.

Figure 1.

Figure 2.

Figure 3.

Figure 4.

Figure 5.

References

Brown, M. E., and R. E. Hill, Discovery of an extended sodium atmosphere around Europa, *Nature*, *380*, 229–231, 1996.

Combi, M. R., K. Kabin, T. Gombosi, D. DeZeeuw, and K. Powell, Io's plasma environment during the Galileo flyby: Global three-dimensional mhd modeling with adaptive mesh refinement, *J. Geophys. Res.*, *103*, 9071–9081, 1998.

DeZeeuw, D. L., and K. G. Powell, An adaptively-refined Cartesian mesh solver for the Euler equations, *J. Comp. Phys.*, *104*, 55–68, 1993.

Gombosi, T., The plasma environment of comets, *Rev. Geophys.*, *29*, 976–984, 1991.

Gurnett, D. A., W. Kurth, A. Roux, S. J. Bolton, E. A. Thomsen, and J. B. Groene, Galileo plasma wave observations near Europa, *Geophys. Res. Lett.*, *25*, 237–240, 1998.

Hall, D. T., D. F. Strobel, P. Feldman, M. McGrath, and H. A. Weaver, Detection of an oxygen atmosphere on Jupiter's moon Europa, *Nature*, *373*, 677–679, 1995.

Ip, W. H., Europa's oxygen exosphere and its magnetospheric interaction, *Icarus*, *120*, 317–325, 1996.

Johnson, R. E., *Energetic charge-particle interaction with atmospheres and surfaces*, Springer Verlag, Berlin, 1990.

Khurana, K. K., M. G. K. nd D. J. Stevenson, G. Schubert, C. T. Russel, R. J. Walker, and C. Polanskey, Further evidence for the presence of oceans in europa and callisto, *Nature*, *00*, 00, 1998.

Kivelson, M. G., K. Khurana, S. Joy, C. Russel, D. Southwood, R. J. Walker, and C. Polanskey, Europa's magnetic signature: Report from Galileo's pass on 19 December 1996, *Science*, *276*, 1239–1241, 1997.

Kivelson, M. G., K. K. Khurana, D. J. Stevenson, L. Bennett, S. Joy, C. T. Russel, R. J. Walker, and C. Polanskey, Europa and callisto: Induced or intrinsic fields in a periodically varying plasma environment, *J. Geophys. Res.*, *00*, 00, 1998.

Kliore, A. J., D. Hinson, F. Flasar, A. Nagy, and T. Cravens, The ionosphere of Europa from Galileo radio occultations, *Science*, *277*, 355–358, 1997.

Kumar, S., and D. M. Hunten, The atmospheres of io and other satellites, in *Satellites of Jupiter*, edited by D. Morrison, pp. 782–806, The university of Arizona press, 1982.

Nagy, A. F., J. Kim, T. E. Cravens, and A. J. Kliore, Hot oxygen corona at europa, *Geophys. Res. Lett.*, *00*, 00, 1998.

Neubauer, F. M., The sub-Alfvénic interaction of the Galilean satellites with the Jovian magnetosphere, *J. Geophys. Res.*, *00*, 00–00, 1998.

Powell, K. G., An approximate Riemann solver for magnetohydrodynamics (that works in more than one dimension), Tech. Rep. 94-24, ICASE, Langley, VA, 1994.

Powell, K. G., P. Roe, R. S. Myong, T. Gombosi, and D. L. DeZeeuw, An upwind scheme for magnetohydrodynamics, Tech. Rep. 95-1704 CP, AIAA Paper, 1995.

Saur, J., D. F. Strobel, and F. M. Neubauer, Interaction of the Jovian magnetosphere with Europa: constrains on the neutral atmosphere, *J. Geophys. Res.*, *00*, 00, 1998.

Schneider, N. M., D. M. Hunten, W. Wells, A. B. Schultz, and U. Fink, The structure of Io's corona, *Astrophys. J.*, *368*, 298–315, 1991.

Schreier, R., A. Eviatar, V. M. Vasyliūnas, and J. D. Richardson, Modeling the Europa plasma torus, *J. Geophys. Res.*, *98*, 21231–21243, 1993.

Smyth, W. H., and M. R. Combi, A general model for Io's neutral gas clouds. II. application to the sodium cloud, *Astrophys. J.*, *328*, 888–918, 1988.

Torr, M. R., and D. G. Torr, Ionization frequencies for Solar cycle 21: revised, *J. Geophys. Res.*, *90*, 6675–6678, 1985.

van Leer, B., C. H. Tai, and K. G. Powell, Design of optimally-smoothing multi-stage schemes for the Euler equations, in *AIAA 9th Computational Fluid Dynamics Conference*, no. AIAA-89-1933-CP, Washington, D.C., 1989.

Wolff, R. S., and D. A. Mendis, On the nature of the interaction of the Jovian magnetosphere with the icy Galilean satellites, *J. Geophys. Res.*, *88*, 4749–4769, 1983.

Wu, F.-M., D. L. Judge, and R. W. Carlson, Europa: ultraviolet emissions and the possibility of atomic oxygen and hydrogen clouds, *Astrophys. J.*, *225*, 325–334, 1978.

K. Kabin, M. R. Combi, T. I. Gombosi, A. F. Nagy, D. L. DeZeeuw, Department of Atmospheric and Oceanic Sciences, The University of Michigan, Ann Arbor, MI 48109. (e-mail: kabin@engin.umich.edu)

K. G. Powell, Department of Aerospace Engineering, The University of Michigan, Ann Arbor, MI 48109.

Received July 10, 1998; revised ???; accepted ???.

This manuscript was prepared with AGU's LaTeX macros v4, with the extension package 'AGU^{++}' by P. W. Daly, version 1.5b from 1996/10/24.

Figure Captions

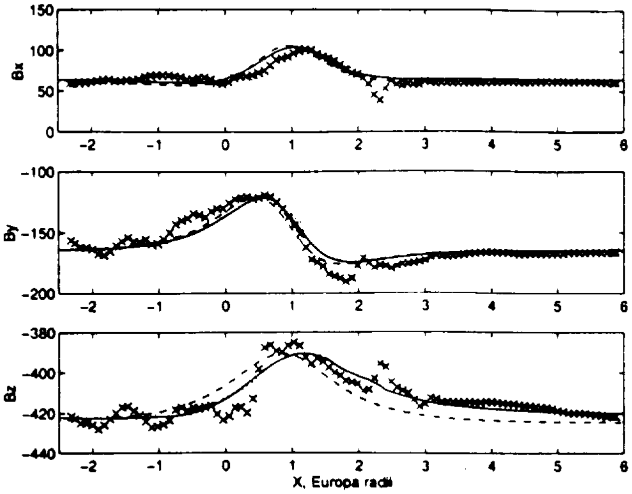

Figure 1. Magnetic field components: x – measured, dashed line – vacuum superposition, dotted line – superconducting sphere with dipole and continuous line – absorbing sphere with mass-loading, ion-neutral charge exchange, recombination and dipole.

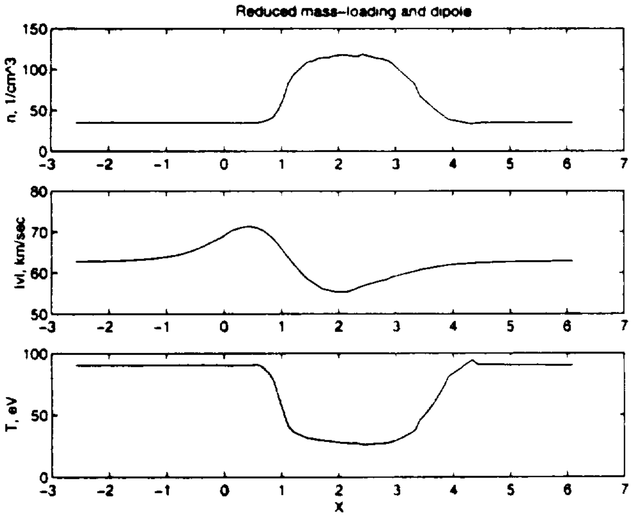

Figure 2. Density, speed and temperature profiles along the fly-by, for absorbing sphere with mass-loading, ion-neutral charge exchange, recombination and dipole.

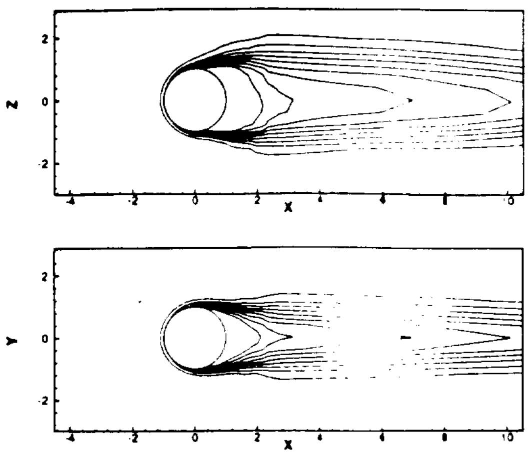

Figure 3. Density; the contour lines are separated by 10 cm^{-3} increments. The lowest contour line (on the outside) is 40 cm^{-3}.

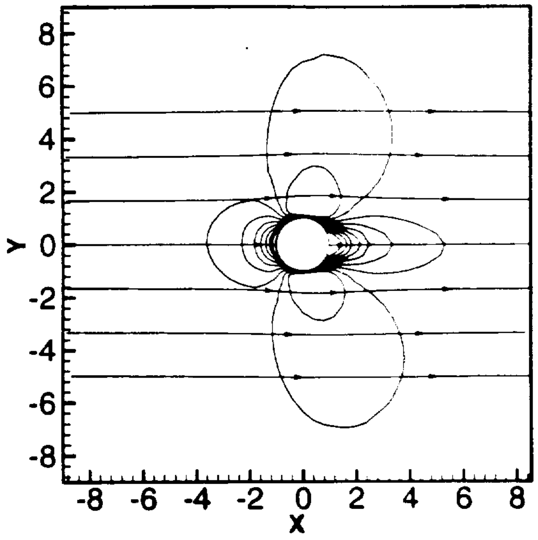

Figure 4. Speed and streamlines in XY plane. The contour lines with 3 km/s increments. The contours stretched in the Y direction correspond to 94 and 91 km/s, the outmost contour stretched in the X direction is 88 km/s.

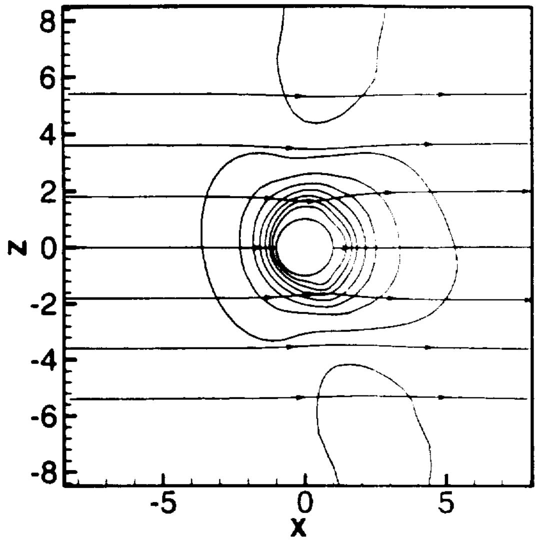

Figure 5. Speed and streamlines in XZ plane. The contour lines with 3 km/s increments. The "wings" correspond to 91 km/s, the first closed contour is $88 km/s$.

Dust-Gas Interrelations in Comets: Observations and Theory

Michael R. Combi, Konstantin Kabin, Darren L. DeZeeuw and
Tamas I. Gombosi
Space Physics Research Laboratory
Department of Atmospheric Oceanic and Space Sciences
The University of Michigan
Ann Arbor, MI 48109, USA

Kenneth G. Powell
W.M. Keck Foundation CFD Laboratory
Department of Aerospace Engineering
The University of Michigan
Ann Arbor, MI 48109, USA

Abstract. The development of the expanding atmosphere from the evaporating cometary nucleus has traditionally focused on observing and modeling the separate development of two distinct components, gas and dust, which are coupled dynamically with one another at distances out to a few tens of cometary radii. In the last decade or so, however, direct evidence from observations and suggestions from theory imply that the dusty-gas coma is a tightly coupled system where material is transferred between the solid and gaseous phase as an important integral part of the basic development of the coma.

Comet Hale-Bopp (C/1995 O1) was discovered far from the sun and is the largest and most productive comet, in the sense of release of gas and dust, in modern times. This has permitted observations to be made over an unprecedented range of heliocentric distance. This paper presents a review of a range of important issues regarding interrelations between dust and gas in comets, a description of the gas and dust environment for Hale-Bopp, and a summary of the preliminary results from Hale-Bopp which are relevant to these issues. Particular topics include dusty-gas models, dust fading and fragmentation, the role of dust and gas jets, the day/night distribution of gas and dust, and extended sources of gas.

Key words: Comets, Hale-Bopp, Dynamics, Photochemistry

1. Introduction

Historically, the term comet has been given to the expanding atmosphere of neutral and ionized gas and dust surrounding a small icy parent body (the nucleus) which is in an eccentric orbit around the sun and which shows a head (or coma) and one or more tails. It is understood that evaporation of volatile ices from the comet's nucleus, the release of particulate material (dust), and the subsequent interaction between dust and gas in its immediate vicinity (within a few nucleus radii) are responsible for the observed phenomena. For comet P/Halley we do have spacecraft images of the dust distribution in this region. In general, however, the innermost coma serves as an unresolved black box source for the gas and dust observed remotely outside this region. The detailed connection between the icy parent body and the black-box source of gas and dust remains clouded. There is still an incomplete picture regarding the overall nature of the conditions and processes occurring in the innermost coma. As will be discussed in detail below, recent evidence has blurred the traditional separation between the dust and gas components of the coma, indicating that not only are they dynamically coupled to one another but possibly together form a tightly coupled system. There is strong observational evidence for the production of extended non-nuclear sources of gas species which might come from dust or icy grains, and there are theoretical suggestions of recondensation of gases back into icy grains.

Comet Hale-Bopp (C/1995 O1) was discovered far from the sun and is the largest and most productive comet, in the sense of release of gas and dust, in modern times. This, combined with continued advances in ground-based and near-Earth-based instrumentation, has permitted an unprecedented range and quality of remote observations of gas and dust to be obtained. Because the geocentric distance for Hale-Bopp was never very small, this inner region is typically unresolved, and therefore continued progress in our understanding of the important innermost coma requires a combination of observational evidence of gas and dust exiting this region and theoretical modeling which accounts for the basic physics and chemistry. Observations of comet Hale-Bopp which provide new insight into the interrelations between gas and dust in the coma are summarized. Theoretical modeling developments in the study of dusty-gas dynamics are also discussed. Particular topics include dusty-gas models, dust fading and fragmentation, the role of dust and gas jets, the day/night distribution of gas and dust, and extended sources of gas.

2. The Gas-Dust Environment of Comet Hale-Bopp

Most coma modeling has been performed either for rather faint, to moderate, to so-called bright (P/Halley) comets. The very large production rate of Hale-Bopp introduces some interesting physical effects which are usually not very important in other comets and are often totally ignored in the interpretation of data. The first obvious difference is the large collisional coma. A typical definition for the collisional zone of a spherical coma is that distance where the local collisional mean free path is equal to the distance from the center of the nucleus. For example Whipple and Huebner (1976) give

$$R_{coll} = \frac{Q_{gas}\sigma}{4\pi v}$$

For the conditions of a Halley-class comet at 1 AU, a total gas production rate, $Q_{gas} = 7 \times 10^{29} s^{-1}$, a nominal collision cross section of $\sigma = 3 \times 10^{-15} cm^2$, and an outflow velocity of about 0.9 km s^{-1}, the collision zone radius is about 1.9×10^4 km. For comet Hale-Bopp near perihelion the total gas production rate is close to $10^{31} s^{-1}$. All else being equal, this would yield a collision sphere of about 2.7×10^5 km. The primary heating agent of the neutral coma is the collisional thermalization of the energy imparted to hot H atoms produced in the main branch of water photodissociation. In a Halley-class comet, because of the 20-to-1 mass ratio between H atoms and the average heavy molecule, the H atoms actually begin to decouple collisionally at ~/10 % of the typical collision zone radius, producing a moderating effect on photochemical heating which is dependent on the magnitude of the gas production rate. This was first treated in the context of hydrodynamic models using heuristic approximations (Ip 1983; Kitamura 1986), escape probabilities (Huebner and Keady 1983), and multifluids for pre-thermal and thermalized H (Marconi and Mendis 1984). Later iterative Monte Carlo-type kinetic models for H atoms were developed to explicitly calculation the collisional efficiency (Combi 1987; Bockelèe-Morvan and Crovisier 1987; Combi and Smyth 1988; Ip 1989). The combination of the variations of photochemical heating rate and the overall gas production rate with heliocentric distance is responsible for the variation of the terminal outflow speed of molecules and radicals in the outer coma. The large collision sphere implies that comet Hale-Bopp should have had a much larger region of photochemical heating resulting in higher gas kinetic temperatures and larger outflow speeds. A second related effect of the large gas densities is that infrared radiative cooling is effectively shut-off for the entire collisional coma (Bockelèe-Morvan and Crovisier 1987), thereby further enhancing the effect of the photochemical heating on the coma temperature and outflow speed.

The last important effect of the large coma densities on the expected behavior of the coma is the non-negligible opacity of ionizing and dissociating solar ultraviolet radiation into the inner coma. Marconi and Mendis (1984) had calculated a 1D multifluid spherical coma model for comet Halley conditions, with a self-consistent calculation of the effect of UV opacity in three UV wavelength bands which are primarily responsible for the main photodecay branches of water:

1: $\lambda < 1860$ Å: H + OH

2: $\lambda < 1450$ Å: H_2 + $O(^1D)$

3: $\lambda < 984$ Å: ionization (mostly H_2O^+).

The half-power points of their radial profiles of UV attenuation serves a good indicator of the typical distance for shielding the inner coma from incoming UV solar radiation in each wavelength band. If their results are scaled from the production rate in Halley to that of Hale-Bopp at 1 AU, shielding distances of 600, 1100, and 3300 km in each of the three wavelength bands, respectively, are found. This means that in the case of a spherical coma for comet Hale-Bopp ionization will be effectively shut off within ~3300 km of the nucleus (and in a cylindrical shadow extending to ~60,000 km antisunward given the size of the Sun's disk). Photodissociations will similarly be shut-off within about 800 km of the nucleus, and the ratios between the various branches will be modified within distances of ~1000 km. For a non-spherical coma, for instance where the gas production is skewed primarily sunward and in narrow jets, local effects could be even stronger because of the higher concentrations of gas density. The increased opacity could have consequences on extracting parent production rates or interpreting spatial profiles obtained from very high spatial resolution observations of daughter radicals near the nucleus.

Using a 1D-spherical hybrid kinetic/dusty-gas-hydrodynamic calculation with a fairly simple composition, the gas velocity and temperature have been calculated for a range of heliocentric distances for conditions appropriate for comet Hale-Bopp. This formulation accounts for a water-driven photochemistry, which should be dominant even for fairly large heliocentric distances. The kinetic portion of the calculation is a Monte Carlo model that explicitly accounts for the collisional efficiency of hot H atoms from the main water dissociation, and is solved iteratively with the 1D-spherical steady-state equations for mass, momentum, and energy assuming an ideal gas. The detailed parameters (lifetimes, branching ratios, collision cross sections) have been discussed at length already (Combi and Smyth 1988; Combi 1989; Combi and Feldman 1993). For these models a nucleus radius of 25 km is adopted and the gas coma is assumed to be composed of 80% H_2O, 16.5% CO, and 3.5% CO_2. The CO and CO_2 are included mainly to raise the mean molecular mass to the correct level (about 20 amu). All of the dust is assumed to have a mean size of 0.65 mm. Past calculations for P/Halley (Combi 1989) produced reasonable results for both the velocity of the gas and the dust particles using only a single dust size of 0.65 μm and a density

Table I. Hybrid Kinetic Dusty Gas Hydrodynamic Model.

r (AU)	$Q(H_2O)$ ($10^{28} s^{-1}$)
3	40.
2.5	70.
2	140.
1.5	200.
1	800.

of 1 g cm^{-3} which gave equivalent results to using an entire more realistic distribution of dust sizes and size dependent particle bulk density (Gombosi et al. 1986). For the calculations presented here a dust-to-gas ratio of 5 times that of Halley was adopted, as is indicated in photometric measurements of $Af\rho$ by Schleicher et al. (1997). As will be discussed below, $Af\rho$ is only a good indicator of the abundance of visible wavelength (half-micron) sized particles, and is only related to the real dust-to-gas ratio given some the particle size and terminal velocity distributions. The calculation accounts for the UV optical depth of the water photodissociation rate which is effectively shut off in the inner coma for distances ranging from 800 km at 1 AU to only 35 km at 3 AU. Table I gives the assumed parameters used for the particular calculations.

Figure 1 shows the variation of the gas radial outflow velocity and the gas kinetic temperature as a function of distance from the center of the nucleus for the model calculations. The temperature shows the typical drop to very low values at a few hundred km caused by the dominance of the pressure-driven expansion. The precise form of the drop is a balance between the expansion-cooling and dust-gas heating in the inner coma and photochemical heating in the outer coma. Because of the large production rate, rather larger outflow speeds for parent molecules are expected to be found for Hale-Bopp than for Halley at comparable heliocentric distances. These are produced by increased photochemical heating efficiency resulting from the more complete thermalization of hot H atoms, as well as by increased gas heating by the dust in the inner coma caused by the large dust-to-gas ratio.

These model results compare favorably to early observations from which outflow velocity and temperature of the coma have been determined. Biver et al. (1997, 1998) derived mean coma outflow speeds and rotational temperatures from their mm and sub-mm observations of CO and CH_3OH at IRAM and JCMT corresponding to beam aperture full-

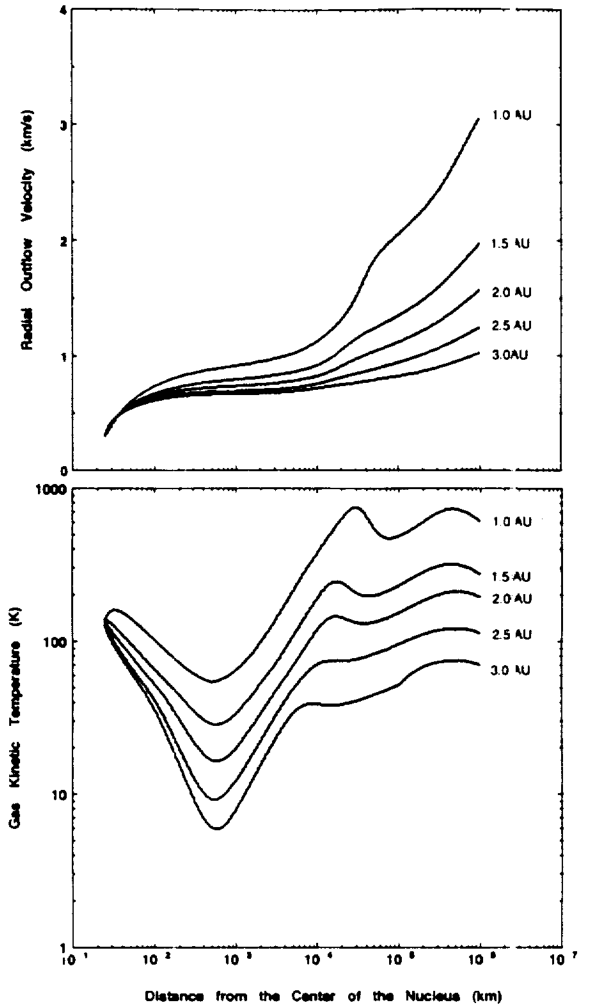

Figure 1. 1D-Spherical Hybrid Kinetic/Dusty-Gas Hydrodynamics. The results of 1D-spherical dusty-gas hydrodynamic model for comet Hale-Bopp where the photochemical heating rate is calculated by a kinetic Monte Carlo simulation.

width-half-maxima (FWHM) in the range of 10 to 26 arcsec. At least in the inner coma, which is primarily sampled by these measurements, the large collision rates discussed above, should maintain a reasonable equilibrium between the gas kinetic and rotational temperatures. We have integrated the mean radial outflow velocity and mean gas kinetic temperature from the results obtained from the 1-D model over a Gaussian beam of 14 arcsec (the intermediate size for the observations) at the appropriate pre- and post- perihelion geocentric distances and fitted them to power-law variations with heliocentric distance for comparison with the results of Biver et al. They found pre- and post-perihelion velocities in km s^{-1} of 1.18 $r^{-0.44}$ and 1.07 $r^{-0.37}$, and rotational temperatures of 116 $r^{-1.24}$ and 93 $r^{-0.83}$ in Kelvin. Here, r is the heliocentric distance in AU. For the corresponding model values we find pre- and post- perihelion velocities of 1.01 $r^{-0.32}$ and 1.02 $r^{-0.34}$ and temperatures of 114 $r^{-1.6}$ and 117 $r^{-1.6}$. The small differences between pre- and post- perihelion results from the model are due to the differences in geocentric distance for corresponding observations before and after perihelion. The agreement between model and observations for the mean outflow speed is quite good. Perhaps this should not be too surprising because the same calculation was successful in explaining a number Doppler resolved observations for comets P/Halley and Hyakutake 1996B2 (Combi 1989; Smyth et al. 1995; Combi and Cochran 1997). Despite the fact that it is not clear that the mean rotational temperature extracted from the observed aperture-integrated spectrum should necessarily yield the same temperature as the mean value of the gas kinetic temperature integrated over the same aperture, the agreement between temperatures and their variation between the observations and the simple model calculation is nonetheless quite good.

An independent confirmation of the model outflow speeds at large distances is found in a comparison with the analysis of the OH line profile observed with the Nançay radio telescope (HPBW of 3.5 by 19 arc min) by Colom et al. (1998). Using a model which assumes an OH velocity of 1.05 km s^{-1}, water and OH lifetimes at 1 AU of 8.2 $\times 10^4$ s and 1.1-1.6 $\times 10^5$ s (the range coming from the heliocentric velocity dependence) they find mean water outflow velocities of 0.7 km s^{-1} for the comet at 3 AU and 2.2 km s^{-1} at 0.93 AU. This is in excellent agreement with the outflow speeds at large distances from the comet at both heliocentric distances in the model calculation.

Measurements of gas species are typically interpreted using a model which adopts (by necessity) an outflow speed. The radial outflow speed for Hale-Bopp clearly varies with both distance from the nucleus and overall with heliocentric distance. Based on our calculations both variations can be expected to be much more pronounced than had been found for Halley (Combi 1989) because of the enhanced photochemical heating efficiency in Hale-Bopp. Based on the comparison above with velocities and temperatures extracted from observations, we believe that the model velocities and temperatures shown here are reasonably representative of the conditions in comet Hale-Bopp. The velocities might be especially useful in the analysis of observations where the dynamical conditions in the coma are needed. These are given in Table II.

Observations of the coma of comet Hale-Bopp indicate that the ejection of dust into the coma is primarily, perhaps exclusively in the sunward direction. (Rauer et al. 1997; Hayward et al. 1997; Weaver et al. 1997). Near perihelion a well-developed system of dust haloes on the sunward side of the nucleus indicates* that dust is ejected into a narrow jet from a primary active area when that area is illuminated by sunlight (Lederer et al. 1998; Larson et al. 1998). Gas seems also to be primarily produced from this active area, although it appears to remain active at a reduced level even when rotated into the apparent night side of the nucleus (Samarasinha et al. 1998; Larson et al. 1998). It is clear then that, although 1D spherical models are valuable for determining the nature of global average gas and dust dynamics, multidimensional models are necessary to understand many important attributes of comet Hale-Bopp.

We present here the results of a three-dimensional calculation for the dusty- gas dynamic flow in the vicinity of the nucleus for an active area superimposed on a uniform background. The calculation is performed on an unstructured multiscale Cartesian octree grid using adaptive mesh refinement. This octree structure is a hierarchical cell structure, based on multiple generations of cubic parent cells which can be split into 8 child cells (see DeZeeuw and Powell 1992). The adaptive refinement of the mesh follows the gradients of the dynamical variables of the calculation and naturally results in the smallest cubes in regions where the flow gradients are the highest. Such a scheme makes optimal use of computer resources allowing problems with disparate scales and complex geometries to be modeled globally (i.e., a large simulation volume), while still retaining sufficient resolution for following small features locally , such as capturing shocks. The general numerical method has been applied to the MHD equations for the comet solar-wind interaction (see Gombosi et al. 1996; Häberli et al. 1997a&b; Gombosi et al. 1998), and now to neutral dusty-gas flows without B-fields (Kabin et al. 1998).

Our method differs from a series of limited three-dimensional dusty-gas calculations by Crifo and coworkers (Crifo et al. 1995, 1997, and 1998) in fundamentally important ways. With their model they have already investigated a number of complicated emission conditions and geometries, including, weak and strong comets, multiple jets, many dust sizes, and non- spherical nuclei. Their calculation is performed on variable-sized, but fixed, spherical-polar grid. Because of the natural singularity in the spherical-polar grid at the pole, their solution is limited to regions away from the pole. Our method uses nested Carte-

Table II. 1D Spherical Hybrid Kinetic/Hydrodynamic Gas Outflow Velocities.

log d(km)	Heliocentric Distance (A.U)				
	1.0	1.5	2.0	2.5	3.0
1.4	0.300	0.296	0.293	0.291	0.289
1.5	0.408	0.426	0.500	0.432	0.431
1.6	0.507	0.505	0.531	0.495	0.491
1.7	0.582	0.560	0.548	0.538	0.531
1.8	0.641	0.603	0.585	0.570	0.561
1.9	0.689	0.636	0.613	0.595	0.585
2.0	0.728	0.664	0.636	0.616	0.604
2.1	0.760	0.687	0.656	0.632	0.619
2.2	0.787	0.706	0.672	0.646	0.631
2.3	0.810	0.722	0.686	0.656	0.640
2.4	0.830	0.737	0.697	0.664	0.647
2.5	0.848	0.749	0.706	0.671	0.652
2.6	0.863	0.759	0.713	0.675	0.655
2.7	0.876	0.767	0.719	0.678	0.657
2.8	0.887	0.774	0.723	0.680	0.659
2.9	0.898	0.780	0.727	0.682	0.660
3.0	0.908	0.786	0.730	0.684	0.662
3.1	0.919	0.793	0.734	0.687	0.663
3.2	0.930	0.799	0.738	0.689	0.665
3.3	0.943	0.807	0.743	0.692	0.667
3.4	0.956	0.816	0.748	0.696	0.669
3.5	0.972	0.826	0.755	0.700	0.672
3.6	0.991	0.837	0.764	0.706	0.677
3.7	1.013	0.851	0.773	0.714	0.682
3.8	1.040	0.867	0.785	0.723	0.690
3.9	1.076	0.886	0.798	0.735	0.700
4.0	1.119	0.911	0.816	0.749	0.711
4.1	1.170	0.943	0.838	0.766	0.722
4.2	1.232	0.986	0.868	0.785	0.732
4.3	1.307	1.042	0.904	0.804	0.742
4.4	1.401	1.100	0.940	0.823	0.752
4.5	1.528	1.150	0.972	0.840	0.761
4.6	1.681	1.193	1.004	0.858	0.771
4.7	1.815	1.230	1.029	0.876	0.782
4.8	1.910	1.266	1.056	0.895	0.793
4.9	1.983	1.303	1.109	0.914	0.804
5.0	2.048	1.341	1.112	0.934	0.816
5.1	2.112	1.382	1.142	0.955	0.827
5.2	2.181	1.426	1.174	0.978	0.840
5.3	2.255	1.475	1.210	1.003	0.856
5.4	2.338	1.530	1.249	1.030	0.874
5.5	2.433	1.591	1.292	1.059	0.894
5.6	2.543	1.659	1.339	1.091	0.915
5.7	2.666	1.732	1.390	1.124	0.938
5.8	2.796	1.809	1.445	1.160	0.963
5.9	2.926	1.887	1.503	1.198	0.989
6.0	3.050	1.964	1.562	1.237	1.016

d = distance from the center of the nucleus in km.

sian cells, avoiding the geometrical singularity limitation and permitting fully global modeling adapting the cell structure to the calculation automatically, and with no spatial limitations.

Briefly the calculation solves the standard dusty-gas Euler equations for mass density, momentum and energy for a single-fluid gas and the equations for mass density and momentum of a number of dust particle sizes. For a detailed discussion see the review by Gombosi et al. (1986). The coupled system can be written in Cartesian coordinates as:

$$\frac{\partial \rho}{\partial t} + \nabla \cdot (\rho \mathbf{u}) = \frac{\delta \rho}{\delta t}$$

$$\rho \frac{\partial \mathbf{u}}{\partial t} + \rho (\mathbf{u} \cdot \nabla) \mathbf{u} + \nabla p = -\mathbf{F}$$

$$\frac{1}{\gamma - 1} \frac{\partial p}{\partial t} + \frac{1}{\gamma - 1} (\mathbf{u} \cdot \nabla) p + \frac{\gamma}{\gamma - 1} p (\nabla \cdot \mathbf{u}) = -Q$$

$$\frac{\partial \rho_i}{\partial t} + \nabla \cdot (\rho_i \mathbf{v}_i) = \frac{\delta \rho_i}{\delta t} \qquad i = 1..N$$

$$\rho_i \frac{\partial \mathbf{v}_i}{\partial t} + \rho_i (\mathbf{v}_i \cdot \nabla) \mathbf{v}_i = \mathbf{F}_i \qquad i = 1 \ldots N$$

where ρ is the gas mass density, u is the gas velocity, p is the gas pressure, vi and ρ_i are the velocity and mass density for dust particles of radius a_i. The terms on the right hand sides of the equations are the various source terms. $\frac{\delta \rho}{\delta t}$ is the gas production source. $\frac{\delta \rho_i}{\delta t}$ is the dust production source. F is the gas-dust drag force. Q is the dust-gas heat exchange rate. Then we can write the source terms as

$$\mathbf{F}_i = \frac{3 \rho_i}{4 a_i \rho_d} p C_D' \mathbf{s}_i$$

$$\mathbf{F} = \sum_{i=1}^{N} F_i$$

$$Q = \frac{\gamma + 1}{\gamma} \rho C_p u \sum_{i=1}^{N} \left(T_i^{rec} - T_i \right) St_i'$$

$$\mathbf{s}_i = \frac{\mathbf{u} - \mathbf{v}_i}{\sqrt{2 \frac{kT}{m_0}}}$$

Here C_p is the gas heat capacity at constant pressure and the rest of the coefficients can be defined under the assumption of diffusive reflection as:

$$C_D' = \frac{2\sqrt{\pi}}{3}\sqrt{\frac{T_i}{T}} + \frac{2s_i^2+1}{s_i^2\sqrt{\pi}}e^{-s_i^2} + \frac{4s_i^4+4s_i^2-1}{2s_i^3}\mathrm{erf}(s_i)$$

$$T_i^{rec} = \left(1+\frac{\gamma-1}{\gamma+1}s_i^2R_i'\right)T$$

$$R_i' = \frac{\left(2s_i+\frac{1}{s_i}\right)e^{-s_i^2}/\sqrt{\pi}+\left(2s_i^2+2-\frac{1}{s_i^2}\right)\mathrm{erf}(s_i)}{s_ie^{-s_i^2}/\sqrt{\pi}+\left(s_i^2+\frac{1}{2}\right)\mathrm{erf}(s_i)}$$

$$St_i' = \frac{e^{-s_i^2}}{8s_i\sqrt{\pi}}+\frac{1}{8}\left(1+\frac{1}{2s_i^2}\right)\mathrm{erf}(s_i)$$

The dust bulk density, ρ_d, is the mass density of a particular dust particle. The gas temperature is T. The dust temperature, T_i, is constant for a particular dust particle size in equilibrium with solar radiation. C_p is the gas specific heat at constant pressure and the various other quantities are given assuming the standard free molecular conditions for gas-dust (Probstein 1968 with minor corrections by Kitamura 1986). These are s_i, the gas-dust relative Mach number, C_D', the dust-gas drag coefficient, T_i^{rec}, the recovery temperature, R_i', the heat transfer function, and St_i' the Stanton number. The equations are presented here in terms of the primitive variables (density, velocity, and pressure); they are rewritten in terms of the conserved variables (mass, momentum, and energy) for the purpose of solving them numerically.

We first present here a calculation for a single concentrated gas/dust jet with uniform production over the rest of the nucleus. The nucleus is taken to be a sphere with radius of 28 km. Based on rough estimates relevant for comet Hale-Bopp at 1 AU, we have set 30% of the gas and dust production to come from a single active area with a Gaussian in angle having a width of 10^o (half-angle), and the remaining 70% spread uniformly over the nucleus. The total gas production rate of 10^{31} s^{-1} with a mean molecular mass of 20 amu is adopted. Six sizes of dust particles with radii of 0.1, 1, 10, 100, 1000, and 10000 μm (the latter three corresponding to 0.1, 1 and 10 mm) are adopted with a dust- to-gas mass ratio of 5 (Schleicher et al. 1997) and a number distribution varying as $a^{-3.5}$, where a is the particle radius. The precise value of the dust-to-gas mass ratios depends critically on the extension of the population to very large particles, which contain most of the mass, and the functional form of the size distribution which is not well-specified. For example, essentially the same distribution of small particles for comet Halley yielded total dust-to-gas mass ratios varying from 0.3 (Gombosi 1986) to greater than 1 (Crifo 1991). The actual difference was only in the extension of the distribution to the very large particles (cm-sized) by Crifo, which effect neither the gas dynamics, nor contribute to ground-based observations of dust continuum.

For the model calculations shown here the entire simulation box extended to ± 50 times the nucleus radius (R_n), or to 1400 km from the nucleus. A total of 220,000 cells were included in the simulation and the cells ranged in size from 0.78 R_n to 10 R_n. The adaptive mesh structure is shown for the full simulation box and for a magnified region near the nucleus in Figure 2. As in the models of Crifo and co-workers each dust size is a separate fluid, however in our case the full multifluid calculation is carried out in the whole simulation volume. The full multifluid calculations of Crifo and co-workers which include many more dust sizes (up to 44 logarithmically spaced sizes) are typically carried out in a restricted volume near the nucleus, and are extended to large distances outside the subsonic region using a steady-state expansion calculation. In our full calculation each dust size introduces four additional equations and unknowns to be solved in every cell.

There are a number of important and interesting results from our dusty-gas calculation. Plate 1a-b (color section) shows color contour plots of the number density of the gas with superimposed velocity streamlines and the gas speed. Note that the gas flow lines originating from the active area expands tangentially near the nucleus but that by a several R_n the flow is essentially radial and the asymmetry due to the active area is frozen-in. Plates 2a-b and 3a-b (color section) show similar pairs of plots for two of the sizes of dust with radii of 1 μm and 1 mm. In all cases the color table for the speed plots is the same. Colors for the density are relative because of the large differences in dust bulk mass density from size to size and compared with the gas. We selected these two particular dust sizes because both the density and speed variations are typical for the nearby dust sizes. The plots for the 1 μm particles are very similar to those for the 0.1 and 10 μm particles. Those for the 1 mm particles are similar to those for the 0.1 and 10 mm particles, although the speeds of course are somewhat larger and smaller, respectively,for the two groups. For all dust sizes the dust jet remains more concentrated over the active area and the gas squirts laterally to the side of the dust jet, making the gas distribution more uniform over the day-side hemisphere than the dust. This is not unexpected.

The dust velocities for the small dust sizes (0.1, 1, and 10 mm) follow the gas flow quite closely. Because of the dust mass loading, the gas and

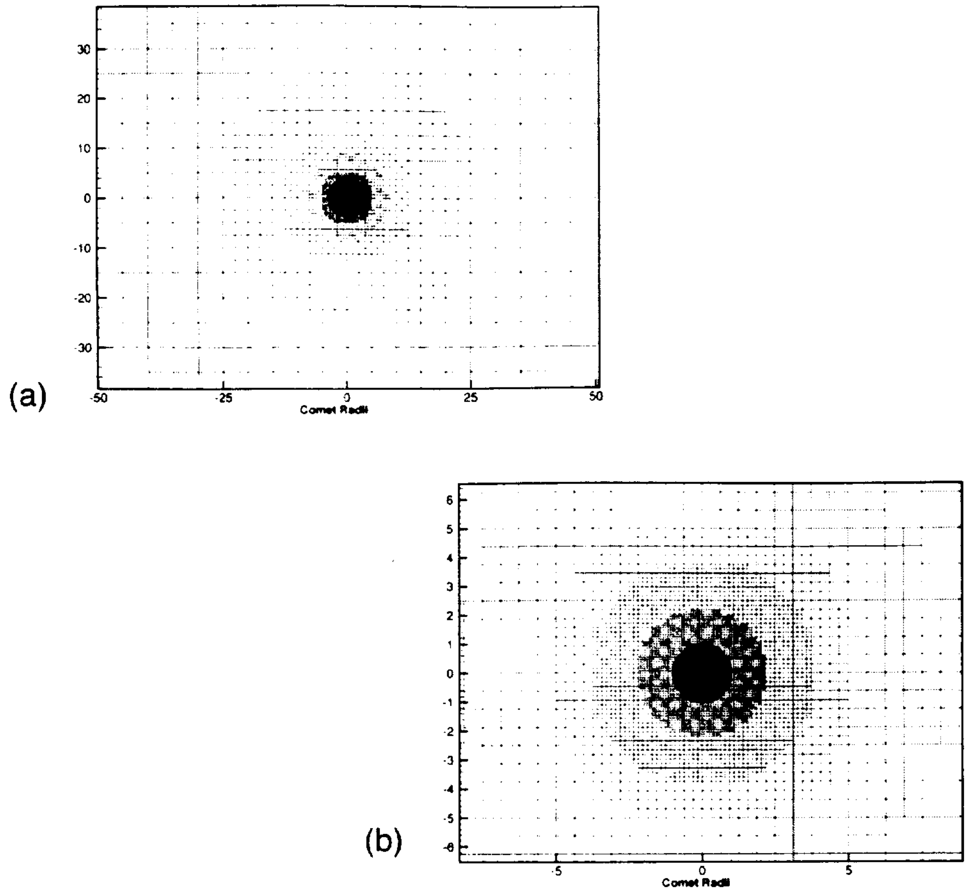

Figure 2. Two Views of Adaptive Mesh for Dust-Gas Jet Calculation. Above in (a) the whole simulation volume is shown extending to 50 nucleus radii (1400 km) from the nucleus. Below in (b) the cell structure around the nucleus is shown, where the nucleus corresponds to the black circle at the center.

small-dust speeds are slowest in the middle of the dust jet and fastest throughout the uniform background. Owing to the large gas densities the smaller dust sizes follow the gas flow very closely everywhere, and only the larger dust sizes show the conical type structure which has been seen even in the early 2D- axisymmetric dusty-gas jet modeling (Kitamura 1986; Körösmezey and Gombosi 1990). Furthermore, the larger dust sizes achieve the highest speeds in the jet (i.e., to the left in the Plate 3b), where the gas densities are the highest, and somewhat lower speeds away from the jet (i.e. to the left in Plate 3b), the opposite behavior of the small particles.

The most important implications from the model calculations result from the overall large dust speeds of all particles, compared with past calculations of moderately bright, Halley-class, comets. All of the particles in the optical size range, i.e. those that make the dominant contribution to optical CCD imaging of the dust coma, and of course smaller particles, are accelerated to ~90% or more of the gas velocity. There is only a small range in speeds. Even the 10 μm particles are accelerated to ~75% of the gas speed. The uniform speeds of particles in the optical size range may be responsible for the sharpness of the observed dust jets in Hale-Bopp and for the rough spatial coincidence (or at least roughly similar spiral pitch angles) of the spiral dust jets and gas jets in the CCD-images (Larson et al. 1998; Lederer et al. 1998; Samarasinha et al. 1998). In Halley, the small grains suggested to be the source of the gas jets (sub-μm) were accelerated to nearly the gas velocity, but the larger optical-size grains (μm sized) were not. The combination of different outflow speeds with nucleus rotation produced a velocity sorting effect between gas (CN) and dust jets (Samarasinha, private communication). In Hale- Bopp near perihelion, our calculation shows that all the optical and smaller particles are accelerated to nearly the gas speed. Therefore, there should be little velocity-sorting between optical and smaller particles, resulting in sharp dust jets, and gas jets following the same spiral arcs as the dust jets. We have also run a model with 85% of the gas production and all of the dust production coming from one active area, and the resulting large dust velocities for optical- sized particles are similar (see below).

Only the largest particles show the typical fall-off in velocity with increasing particle size, however, the velocities are still much larger than the usual published values that are based on comets with much lower gas production rates (Crifo 1991; Gombosi et al. 1986). This may have important consequences on the estimate of total dust-to-gas mass ratios extracted from long-wavelength observations which are sensitive to detecting most of the dust mass that is present in mm-sized particles (Senay et al. 1998). In Table III we show values of the gas and dust particle velocities at different angular locations compared with the jet near the outer portion of the simulation box at a distance of 1300 km from the center of the nucleus.

Only preliminary reduction and analyses have been performed on the data needed to properly characterize the realistic balance between the separate components of gas and dust in an active jet and in a uniform background. The two cases we have examined, one with 30% of the production in the jet and one with 85% of the production in the

Table III. 1D Gas and Dust Terminal Speeds in a 3D Dust-Gas Jet

	Terminal Speeds in m s^{-1}			
Species	In Jet	45°	90°	135°-180°
Gas	718	734	748	810
0.1 μm	698	718	727	795
1.0 μm	647	668	669	741
10 μm	549	556	555	603
0.1 mm	394	370	370	355
1.0 mm	212	182	182	148
10 mm	84	72	73	48

jet, yield very similar large dust particle speeds. Therefore, the large dust speeds can be used in the next iteration of the process of trying to understand the temporal and geometric aspects of rotating dust and gas jets in the coma from the observations. They should also be used in the interpretation of long wavelength observations which detect mainly the large mm-sized particles which are the dominant contributors to the global dust mass production rate.

For comparison with the first model results shown in Plates 1-3, Plate 4a-b (color section) shows the gas number density and dust bulk mass density for the 1-μm optical- sized particles in the vicinity of the nucleus in the case of a strong jet where 85% of the gas production and 100% of the dust production is in the jet and only 15% of the gas production is distributed uniformly around the nucleus. For this more confined distribution of material at the surface of the nucleus the dust jet remains more focused but the gas distribution broadens, expanding to 2 to 3 times its original Gaussian width. Some evidence from the observed images indicates that the observed jets may be narrower than even this model where 85% of the production is in the jet. This could indicate a role for some kind of collimation due to the spatial topology of the surface, which is not in our current model. Such collimation could be caused by the active area that produces the jet being recessed into the surface as in a crevasse or a crater. The effects of surface topology and local solar insolation which has possible influence on the strength and appearance of gas and dust jets have begun to be addressed by Crifo et al. (1998).

Boice et al. (1998) have also recently presented results of a 1D-spherical dusty coma model of comet Hale-Bopp at several heliocentric distances which includes the surface layer as part of the calculation. Their calculation accounts for gas emission from the surface, from transport through a porous surface layer, and from release of gas from dust in the coma. Separate fluids are included for electrons, heavy neutral gas, fast hydrogen, and dust.

3. Evidence from Observations

3.1. EXTENDED SOURCES OF GAS

The discovery of an extended source of formaldehyde (H_2CO) in comet P/Halley by Eberhardt et al. (1987) using data from the Neutral Gas Mass spectrometer on the Giotto spacecraft provided conclusive evidence of a substantial source of a gas species from unseen parent grains. There was not a sufficient amount of another heavier parent molecule to account for H_2CO which was present at the $\sim$7% level compared with water. That H_2CO is produced by an extended source in comet Hale-Bopp has also been suggested by Womack et al. (1997) and Wink et al. (1998). Radio observations of HNC by Biver et al. (1997) and mm-wavelength observations of CH_3OH by Womack et al. (1997) indicate that these species are also produced by an extended source. However, whether they are produced by grains or molecules (e.g., by photodissociation) is not yet known. In addition, the H_2CO itself was also found to serve as an important extended source for a substantial fraction of cometary CO (Meier et al. 1993; Samarasinha and Belton 1993). This has since been seen in infrared observations of a number of subsequent comets including most recently Hyakutake and Hale-Bopp (DiSanti et al. 1998). From radio observations of the OH radical in Hale-Bopp, Colom et al. (1998) report evidence for water sublimation from grains.

3.2. DUST AND GAS JETS, HALOES AND SHELLS

One of the most interesting aspects of the early analysis of observations of Hale-Bopp is the dominance of gas jet activity. Shortly after discovery at nearly 7 AU it was found that CO, probably the dominant species at that time, was being produced in a narrow, well-focused, day-side jet (Jewitt et al. 1996). Subsequently dust jets in various configurations were seen to dominate continuum images (Kidger et al. 1996; Weaver et al. 1997). Near perihelion in addition to the well-developed day-side dust haloes, which were apparent to anyone looking at the comet through even an amateur telescope, narrow-band CCD imaging showed a set gas jets/haloes. The dust sources were only substantially active on the day side of the nucleus. This created a pattern made by one or more spiral jets which were not visible on the night side. The gas jets, however, continued activity on the night side, but at reduced level. Therefore, the gas jet spiral pattern was generally more continuous.

The CN radical, along with C_2, was one of the earliest spectroscopic detections made in comets (Huggins 1882). Coming from the presumption that CN was produced by the photodissociation of some stable parent molecule, early studies (Potter and DelDuca 1964; Jackson 1976) lead to the suggestion of various candidate species (HCN, C_2N_2, CH_3CN, HC_3N, etc.). The study of a large sample of both radial spatial profiles of CN (Combi and Delsemme 1980) and sunward and antisunward profiles distorted by radiation pressure acceleration (Combi 1980) lead them to conclude that the observational evidence was consistent with the production of CN by the photodissociation of HCN which had been discovered by radio emission (Huebner et al. 1974). However, their results were based on modeling the parent molecule outflow speed using the a heliocentric distance dependent velocity law of $0.58\ r^{-0.6}$ km s^{-1} (Delsemme 1982) which is now known to be too small. Later comparisons of production rates from radio observations of HCN and optical observations of CN (Bockelèe-Morvan and Crovisier 1985) showed that, although for some comets the production rates were roughly equivalent, for others the CN production rate was too large. This indicated multiple sources for CN with different relative compositions, varying from comet to comet.

The discovery of jets of CN in comet P/Halley by A'Hearn et al. (1986) lead them to the conclusion that the CN seen in the jets (at least) was produced from very small CHON (organic particulates rich in compounds containing carbon, hydrogen, oxygen, and nitrogen) grains. They reasoned that only a grain source would remain tightly entrained in the collimated flow. Although it was clear that most gas species and dust were produced from the same major active areas on the surface of the rotating nucleus (Millis and Schleicher 1986), the non-coincidence of CN and dust jets was explained as a velocity sorting according to grain size. The dust continuum was dominated by micron-sized grains which are accelerated only to some fraction (0.5 or less) of the gas velocity (Gombosi et al. 1986), whereas the CN in the jets was produced by very small CHON grains, which are accelerated to nearly the gas speed. Combi (1987), on the other hand, suggested that a localized source of parent molecules might remain collimated enough without the requirement to invoke grains. Parent molecules obviously travel at the gas speed so the non-spatial coincidence would be same whether produced from molecules or sub-micron CHON grains. A subsequent analysis of the CN-jet images by Klavetter and A'Hearn (1994) showed different radial distributions for CN within the jet compared to the CN between the jets, pointing again toward a CN-jet source (grains) with a length scale of ~8000 km, similar to that observed for H_2CO. In addition to CN and C_2 jets (Schulz and A'Hearn 1995), Cosmovici et al. (1988) also reported jets in images of C_3, as well as in a combination image of [OI] plus NH_2 emissions in comet P/Halley.

For comet Hale-Bopp pre-perihelion observations of HCN (Biver et al. 1997) and CN (Schleicher et al. 1997 and Rauer et al. 1997) indicate there is a rough equivalence of the HCN to CN production rate for heliocentric distances larger than about 4 AU. By 3 AU the relative CN production rate increases over HCN by about 60%, and although the published data are incomplete at the time of this writing, indications are that the ratio is approaching 2 near perihelion. Such a behavior is consistent with the gradual activation of a second source of CN at smaller heliocentric distances. Rauer et al. (1997) suggest possible sources in grains which might be activated by 3 AU, or additional parent molecules (CH_3CN and HCN).

Fitzsimmons and Cartwright (1996) and Wagner and Schleicher (1997) suggest that the appearance of CN spectroscopically at greater than 6 AU from the sun points to the same mechanism for at least a large fraction of the CN seen at small heliocentric distances. Therefore, a reasonably consistent picture emerges for a combination of sources. The major one is probably the photodissociation of some set of more volatile parent molecule species including HCN which are active at large heliocentric distances. Then at smaller distances (3 AU) an additional source becomes activated which could be either less volatile parent molecules, small vaporizing grains, or some combination. The variation of the ratios of the various sources from comet to comet, with time (heliocentric distance), and possibly with location on the nucleus, could explain many of the difficulties in tying together a simpler consistent picture with HCN alone (Bockelèe-Morvan and Crovisier 1985).

Regarding the identity of other photodissociation parents for CN, Festou et al. (1998) are suggesting C_2N_2, which has been already on candidate lists for a long time. They find that the a combination of a lifetime of 3.5 $\times 10^4$ seconds at 1 AU and a CN velocity of 1-2 km s^{-1} can explain the observed characteristics of production scale length and the Doppler-broadened velocity profiles. However, caution must be taken that model analysis must account properly for the expected large parent molecule outflow velocities (2 km s^{-1} at 10^5 km) and collisional quenching of the ejection velocity received by daughter radicals upon dissociation of their parents. These attributes of comet Hale- Bopp have been discussed above.

Lederer et al. (1998) have reported gas jets in all of the major visible neutral species, CN, C_2, C_3, NH, and (most importantly) OH during the two-month period surrounding perihelion. Wink et al. (1998) have presented Doppler- resolved radio observations during the same period of CO, HCN, CS, and H_2CO, which indicate production these species into localized jets rotating with the nucleus. The CO jet is active on both the day and the night side and appears to be located at the equator. The average line-of-sight velocity of CO varies periodically with the 11.3-hour rotation period of the nucleus and has an amplitude of about 0.2 km s^{-1}. This is not necessarily indicative of the ejection speed of gas from the jet, but the integrated deviation from a stationary mean composed of the coma average with the velocity dispersion of the jet projected along the line of sight. Wink et al. find that the HCN emission comes from the same location as CO but is weakened in the night side. The CS emission changes in a similar manner but appears to come from an active area in a different location in the northern hemisphere. The H_2CO emission appears in phase with CS but is systematically more blue-shifted. Because H_2CO is not a parent species (likely produced by grains), the extra velocity shift may not be surprising.

Larson and Hergenrother (1998) have presented reduced (i.e., continuum subtracted) CN images and dust continuum images. These show that dust jets and CN jets generally follow the same spiral geometry with nucleus rotation. Taken at face value this means that the velocity of the CN source and the velocity of the dust is about the same. As mentioned already this is in contrast to the case for Halley (A'Hearn et al. 1986) where the gas jet and dust jet had different spiral pitch angles, indicating different velocities. One interesting exception to the jet coincidence was a CN-only jet (or possibly more accurately, a gas-only jet) reported by Larson and Hergenrother.

Samarasinha et al. (1998) have presented a preliminary model for the CN gas jet which reproduces some of the basic features of their own CN images. Their images are otherwise similar to the above-mentioned data from Lederer et al. and Larson et al. Although the detailed appearances of gas and dust jets change with activity and rotation from day to day during this period, the general existence and appearance of dayside dust spirals and dayside and nightside gas spirals were consistent. Their model has a single active region as the source of the CN jet which continues activity on the night side of the nucleus at about 10% of the level on the day side. Taken at face value this might be consistent with the HCN observations of Wink et al. (1998) mentioned above, perhaps suggesting a connection between HCN jets and CN jets, at least in comet Hale- Bopp. If the dust jet activity had continued at a similar level into the night side, it would be very obvious in continuum images. Therefore, it is apparent that the dust jet activity on the night side is reduced to well below the 10% level. This is consistent with the appearance of dust jets in other comets, even Comet Hyakutake (1996B2), which showed well-developed day-side dust jets but fairly uniform (spherical) emission of gas species (CN and OH) from the vicinity of the nucleus (Harris et al. 1997).

Based on the dusty-gas modeling results presented in the previous section of this paper, it is clear that the dust-gas dynamic regime for comet Hale-Bopp, especially with the dominance of local active region(s), is very different from the more typical active comet, e.g., P/Halley, and C/Hyakutake (1996B2). Even fairly large particles (10 μm) in the dust-gas jet will be accelerated to a large fraction of the gas velocity. This means that it is quite natural for the gas and dust jets to be spatially similar in Hale-Bopp, but not so in P/Halley.

Perhaps the more interesting question raised by the existence of gas jets of CN, C_2, C_3, NH, OH (implying H_2O), CO, CS, and H_2CO, and the similar day- night behavior of CN and HCN jets regards the original conclusion by A'Hearn et al. (1986) that the CN in the CN jets of comet P/Halley were produced necessarily from CHON grains. As mentioned above, Combi (1987) had suggested that the parent of the CN in the jets might have just been a local enhancement of a parent molecule, i.e., gas emitted by the local active area which remains focused in a jet. A parent molecule would of course move with local gas speed, just as the small sub-micron grains invoked to explain the CN jets. Dusty-gas hydrodynamic models for localized active regions (Kitamura 1986, Körösmezey and Gombosi 1990; Crifo et al. 1995) have always indicated that radial expansion near the nucleus is rapid and that any jet asymmetry frozen-in by a few nucleus-radii would be maintained to considerable distances. Therefore, the general spherical symmetry of the gas coma in some comets, is probably not due to a simple isotropization from the physics of the inner coma flow expansion from day-side active areas. Either distributed production of gas species over the surface or significant extended production of gas from volatile grains away from the nucleus is required. Comet Hyakutake (1996B2) is an example of a comet with active dayside dust jet production but nearly spherical gas (CN and OH) distribution. There is also direct and indirect evidence for significant gas production from icy particles away from the nucleus (Harris et al. 1997).

3.3. THE CASE FOR C_2

It has been noticed for a long time that the radial distribution of C_2 radicals in comets is unusual compared with most other daughter species (e.g., CN, C_3, NH_2, etc.) whose distributions can all be reproduced by a photochemical model that accounts for one generation of exponential decay from a parent molecule. Delsemme and Miller (1971) suggested that the radial distribution could be explained if C_2 radicals were trapped in clathrate-hydrate icy grains which were liberated from the nucleus similarly to refractory dust particles, dragged away by the outflowing gas, and subsequently vaporized releasing the free C_2 radicals. They presented a mathematical icy grain halo model, which could be fitted to an observed C_2 profile. as an alternative to the photochemical Haser model, which fit poorly. A number of subsequent investigators who published spatial profiles of C_2, sometimes noted the same problem and suggested either that C_2 was produced from grains, or it was produced as a grand daughter species from a primary parent molecule.

Despite the difficulty, observed C_2 profiles (Cochran 1985; Combi & Delsemme 1986; Wyckoff et al. 1988; Fink, Combi, and DiSanti 1991; Schulz et al. 1993; Cochran and Trout 1994) and the extraction of production rates for all species from standard cometary aperture photometry (A'Hearn et al. 1995) have typically been analyzed using a standard 2-generation Haser model. In recent years more and more analyses of observations of OH (e.g., Weaver et al. 1997; Budzien, Festou and Feldman 1994; Cochran and Schleicher 1993) and CN (Schulz et al.1993 a&b, Schulz et al. 1994) have been performed using a vectorial model. Such in not normally the case for C_2. The best-fit Haser scale lengths have generally depended upon the spatial coverage of the data. Parent and daughter scales lengths which are more nearly equal are found if the data cover distances close to the nucleus (Wyckoff et al. 1988: Fink et al. 1993; Schulz et al. 1993). Parent and daughter scale lengths in the ratio of ~6-8 to 1 are found if the data cover distances farther from the nucleus (Cochran 1985; Combi and Delsemme 1986).

By scaling a set of radial profiles of C_2 in comet P/Halley which assumed their length scale they follow an $r^{1.5}$ variation (r = heliocentric distance) O'Dell et al. (1988) produced a single average C_2 profile covering several orders of magnitude in normalized-distance both very close to and very far away from the nucleus. They used a 3-generation version of a Haser-type photochemical model with a sequence of three scale lengths in the ratio of 1:5:50 corresponding to parent, daughter, and C_2 as granddaughter to account for the shape of the composite profile. The recent discovery of acetylene (C_2H_2) in comet Hyakutake and subsequent measurement in comet Hale-Bopp, provides a prime candidate, present at the ~1% level, for the 3-generation chain (C_2H_2 to C_2H to C_2). This particular chain has been suggested for many years (Jackson 1976; Yamamoto 1981; see the review by Jackson 1991).

However, this 3-generation model, like the standard Haser model, ignores the existence of expected excess energy at each photodissociation which has been properly included in the vectorial model (Festou 1981) and otherwise similar Monte Carlo models (Combi and Delsemme 1980). In a more recent spatial profile study for individual profiles in comet P/Halley, Combi and Fink (1997) examined both 3-generation models which included daughter species ejection velocity and a new version of a grain source model that modifies some properties of the older icy grain halo model (Delsemme and Miller 1971) to be appropriate for CHON grains which have been suggested as sources for CN and C_2 jets (A'Hearn et al. 1986, Klavetter and A'Hearn 1994, Schulz and A'Hearn 1995). They found that if the 3-generation model is correct then there are strict limits to the total ejection velocities for both dissociations taken together of < 0.5 km s^{-1}. In addition, they also found that a CHON grain halo could explain the radial distribution for a halo size of about 88,000 km at a heliocentric distance of 1 AU. This is the expected radius for velocity and lifetime of submicron (~0.2 μm) CHON grains (Lamy and Perrin 1987) if they behave as laboratory tholins (Khare et al. 1984).

Another approach into the question of the source of C_2 radicals has been found in comparing the spatial dependence of the (1-0) to the (0-0) Swan bands by Roussellot, LaFont and co-workers. Roussellot et al. (1994) suggested that their observed variation of C_2 (0-0) and (1-0) in comet P/Halley indicates production of vibrationally cool C_2 from the nucleus, presumably from the photodissociation of some parent molecule and hot C_2 in a spatially extended region and in the vicinity of observed jets, which is consistent with production from hot grains. More recent observations of comet Hyakutake (C/1996 B2) by Laffont et al. (1998) yield similar results indicating the production of cool C_2 near the nucleus but the production of high excitation temperature C_2 in the region associated with the antisunward-drifting condensations, clumps or clusters. Laffont et al. (1998) are presenting the results of similar observations and analyses in comet Hale-Bopp at this conference, but the results are not yet available as of this writing.

In an analysis of spatially resolved 1D spectroscopic observations of Hale- Bopp, Korsun et al. (1998) find similarities between the distributions of C_2 and dust continuum not shared by other gaseous species. They find that the other gaseous species (NH_2 and CN) are roughly symmetric (sunward-antisunward) with respect to the nucleus, but that C_2 is asymmetric with a sunward preference similar to the dust continuum. They reason that this is due to production of some of the C_2 from the dust. Sekiguchi et al. (1998) also report more specifically, based on observations of Hyakutake and Hale-Bopp that most C_2 is produced from C_2H_2, but that some C_2 is produced from dust.

3.4. Dust Fading and Fragmentation

A radial profile of column abundance (or brightness in the optically thin limit) varying as the inverse of the projected distance, ρ, is found for a simple constant point source expanding at a constant velocity. This is the simplest picture of dust production in comets. Even in the realistic case where solar radiation pressure is important, the radial profile in the direction away from the sun, as projected on the sky plane, is still found to vary as the inverse of the projected distance (Wallace and Miller 1958). Evidence for the departure from a $1/\rho$ distribution were reported by Jewitt and Meech (1987) and Jewitt and Luu (1989) from analyses of the radial profiles of dust continuum observations in comets. In spite of a technical error in their mathematical model discussed by Combi (1994), the finding by Baum et al. (1992) of what they called dust fading on scales of $\sim 10^4 - 10^5$ km in some comets, but not all, appears to remain valid. They found departures from the simple $1/\rho$ distribution which could be interpreted as a loss of particles with increasing distance from the nucleus. Preliminary indications from observations of comet Hale-Bopp (Schleicher, private communication) are that grain fading does not occur on this spatial scale.

On the other hand, there is evidence that grain fragmentation in the very innermost comae of active comets may be quite important. The brightness profiles of dust continuum determined with the Giotto Halley Multicolor Camera experiment (Keller et al. 1986) within a few tens of km of the nucleus of comet P/Halley flattened considerably. This occurred at distances where dust particles could still be accelerated by outflowing gas, and one might expect to have observed the brightness profile become more steep not less. The fragmentation of particles has the opposite effect from fading on the radial profile (Thomas and Keller 1990; Konno et al. 1993). As particles break apart, the total surface area of all the small particles is larger than those of the original large particles, in the absence of evaporative loss. This increases the total scattering cross section and thus increases the brightness, relative to the base-line $1/\rho$ with increasing distance.

In addition to the Halley Giotto images, there is evidence for fragmentation in the analysis of ground-based dust coma and tail images. In an analysis of dust tail images of comet Austin (1990V) with their inverse Monte Carlo model, Fulle et al. (1993) found that a considerable spread of initial velocities, the so- called terminal velocity, was required for particles having any particular size. This is contrary to the standard Finson-Probstein (1968) dusty-gas dynamics picture which implicitly assumes non-fragmenting particles, and where particles of a certain size and bulk density are accelerated by the gas flow to a particular single velocity, i.e., the velocity distribution for a certain size particle is a delta function. Combi (1994), in order to reproduce ground-based dust coma images of comet Halley using a Finson-Probstein-type Monte Carlo simulation, introduced a heuristic dust-fragmentation function, which assumed that particles started with some velocity given by dusty-gas dynamics and then fragmented into a population of smaller particles. More recent modeling by Fulle et al. (1997) for Hyakutake (1996B2) similarly requires a velocity dispersion for each particle size, implying that particle fragmentation is important within, and perhaps just outside, the dusty- gas acceleration region (typically a couple of hundred km).

Based on the modeling discussed in the previous section of this paper, it appears that for comet Hale-Bopp a wide range of particle sizes will be accelerated to nearly the gas velocity, especially within the concentrated jets. The more uniform velocities for the particles in the 0.1 to 10 μm range, which typically dominate the observed visible dust coma, will probably make the analysis of dust coma and tail images a less sensitive indicator of particle fragmentation than other recent and more moderate comets. All particles regardless of whether they were primary parent particles, or fragments of them, will all be accelerated to nearly the gas velocity and thus will not have much dispersion in velocity.

4. Summary

We have presented a review of the state of knowledge regarding issues of dust-gas interrelations in comets, especially as it relates to comet Hale-Bopp at the time of this writing. We include (1) theoretical modeling of the gas/dust environment for Hale-Bopp, (2) a review of certain important relevant issues as posed from the results of comets observed before Hale-Bopp, and (3) a discussion of new Hale-Bopp observations which either shed new light or at least herald the possible shedding of new light in the not-too-distant future. Hale-Bopp is still being actively observed by the world‘s major observing programs. Despite the fact that we now only have an incomplete and preliminary picture of the observational evidence in this important area, there are already many interesting and important findings and questions.

The dust-gas environment for comet Hale-Bopp especially when very active ($r \leq 1.5$ AU), is very different from the typical bright comets (e.g., P/Halley, and C/Hyakutake 1996B2). The large dust-gas production has a number of important consequences.

- The collisional fluid region is large.

- The resulting increased photochemical heating efficiency significantly increases gas outflow speeds and their variations with distance from the nucleus and with heliocentric distance.

- The large collision region will have an effect on the applicability of free-molecular- flow vectorial models which implicitly assume collisionless expansion.

- The UV opacity in the inner coma is not negligible, and could effect parent lifetimes and ion production especially for observations made with high spatial resolution.

- The high UV opacity will shield ionization within about 3000 km from the nucleus and within a tailward shadow (at $r = 1$ AU), and alter typical ion-neutral chemistry.

- The dust-gas interaction is strong and the region where it is important is large.

- This interaction yields fast micron-sized dust particles accelerated to nearly the gas speed. Even larger mm-size particles are accelerated to much larger velocities than the typical bright comet. Such effects will be important in understanding dust kinematics and in determining total dust-to-gas mass ratios from long wavelength IR and radio observations.

Preliminary observational results regarding dust-gas interrelations are also very interesting.

- The production of gas species and dust seems to be strongly influenced and sometimes dominated by localized active regions that rotate with the nucleus.

- The dust production from the active regions essentially turns-off on the night side.

- The gas production is reduced on the night side, but not completely inactive ($\sim$10% level in some species, but CO is uniformly active).

- There is evidence for extended sources not only for CO and H_2CO, as seen before, but also for CH_3OH, and HNC.

- At large distances ($r > 4$ AU) cometary CN seems to be mostly produced from HCN. At smaller distances ($r < 4$ AU) another source (or sources) appears to become active; suggestions for grains or other parent molecules (C_2N_2, CH_3CN) have been made.

- There is evidence for multiple sources for cometary C_2: photodissociation of C_2H_2 is an obvious candidate, and production of vibrationally excited C_2 from grains has been suggested.

- The new list of gas-jet species from visual-range CCD images of comet Hale-Bopp includes not only CN, C_3, and C_3 as in Halley, but also NH, and OH. Doppler-resolved radio observations indicate a similar behavior for CO, H_2CO, CH_3OH and H_2S. Similarities of behavior of HCN jets in Doppler-resolved radio observations and CN jets in CCD images, and the presence of gas jets in most commonly observed species, especially OH and NH, open to question the conclusion that previously observed CN jets necessarily implied production from an extended source of CHON grains. We examine here the pros and cons of three scenarios:

1. Gas-jet species are produced from CHON grains. Pros: Small organic grains (sub-μm) would be accelerated to nearly the gas speeds in both Halley and Hale-Bopp, accounting for the similar spatial geometry of dust and gas jets in Hale-Bopp but also their dissimilarity in Halley. Small organic grains (0.2 mm) should live long enough (1-2 $\times 10^5$ seconds) for a comet at 1 AU (Lamy and Perrin 1988) to provide a spatially extended source. Cons: The new evidence of gas jets in OH and NH in Hale-Bopp indicates the gas-jet source may be rooted in the volatile fraction of the comet rather than in organic CHON grains. The similar visibility of OH jets and CN jets indicates that the relative source rates are similar in the jets source as in the comet in general. This similar relative abundance was also the case for the OH, CN and C_2 arc-structure seen in the tail of comet Hyakutake (C/1996 B2) which indicated production by typical fragments of the bulk nucleus rather than just CHON grains which are only one component of cometary material.

2. Gas-jet species are produced from volatile nucleus fragments (icy grains). Pros: This picture accounts for production of OH and NH which are considered to be produced from the volatile fraction of the cometary nucleus material, rather than from the organic CHON grains. A similar process has been invoked to explain the production of OH, in addition to CN and C_2 from a secondary source down in the tail of comet Hyakutake (C/1996B2). Cons: In Hyakutake, both the lifetime of the particles (from the persistence of the source) and the motion of the source down the tail indicated that the parent fragment particles were large (mm-sized). In Hale-Bopp the gas-jet source particles are probably still closer to μm size rather than mm size based on the fast velocity and the fact that small icy grains do not survive more than about 10000 km from the nucleus (Delsemme and Miller 1971). Of course, the particles responsible for the jets in Hale-Bopp do not have to be the same as those responsible for the tail-side arc in Hyakutake.

3. Gas-jets are produced simply from localized concentrations of parent molecules. Pros: Because parent molecules are part of the general gas outflow, they, like the smallest grains, will move with the general gas outflow velocity. This would account for the velocity sorting for jets in Halley and for the lack of it in Hale-Bopp. The dusty-gas hydrodynamic models indicate that non- spherical asymmetries in the coma are frozen-in by a few nucleus-radii from the nucleus, therefore con-

centrations in angle of parent molecules could remain concentrated to large distances, thereby possibly maintaining a gas-jet identity. Cons: The gas concentrations which are similar to dust concentrations near the nucleus (10^o half-cone-angle FWHM Gaussians) tend to broaden to $\sim 30^o$ half- cone angle Gaussians by a few nucleus radii. Are these narrow enough to account for the well focused gas jets?

- A few more general and difficult questions regarding both gas and dust jets remain. It may be difficult to account for the constant projected radial propagation velocity of gas and dust jets (0.4 km s^{-1}) solely on geometrical projection effects (Larson, private communication). This has larger consequences than the exact nature of the gas and dust jets. It is clear from the modeling presented here that the outflow velocities (0.7 to 2 km s^{-1}) predicted by dusty-gas dynamics models are consistent with those observed in Doppler resolved measurements (Biver et al. 1998; Colom et al. 1998). How can gas jets propagate at much smaller speeds than the actual gas outflow speed?

Over the coming couple of years the wealth of important observational results for comet Hale-Bopp will be filling the scientific literature. It is very likely that as a result of this singularly bright comet we will obtain definite answers to many of the above important questions about dust-gas interrelations. They have important consequences, not just those pertaining directly to our understanding of the behavior of processes occurring in the coma, but also, and more significantly, on our understanding of the detailed compositional and morphological make-up of comets, and how and where they were formed.

5. Acknowledgments

This research was supported by grants NAG 5-4714 and NAG 5-4381 from the NASA Planetary Atmospheres program. We thank and appreciate a several day email-conference among Steve Larson, Nalin Samarasinha, Dominique Bockelèe-Morvan, and Dave Schleicher for helping to decide a compromise in setting (hopefully) useful 3D dusty-gas jet parameters with which to characterize the physics of the inner coma.

References

A'Hearn, M.F., Hoban, S., Birch, P.V., Bowers, C., Martin, R., and Klinglesmith, D.A.: 1986, *Nature* **324**, 649.

A'Hearn, M.F., Millis, R., Schleicher, D., Osip, D.D., and Birch, P.: 1995, *Icarus* **118**, 223.

Baum, W.A., Kreidl, T.J., and Schleicher, D.G.: 1992, *A. J.* **104**, 1216.

Biver, N., Bockelèe-Morvan, D., Colom, P., Crovisier, J., Davies, J., Dent, W.R.F., Despois, D., Gèrard, E., Lellouch, E., Rauer, H., Moreno, R., and Paubert, G.: 1997, *Science* **275**, 1915.

Biver, N., Bockelèe-Morvan, D., Colom, P., Crovisier, J., Germain, E., Lellouch, E., Davies, J., Dent, W.R.F., Moreno, R., Paubert, G., Wink, J., Despois, D., Lis, D.C., Mehringer, D., Benford, D., Gardner, M., Phyllips, T.G., Gunnarsson, M., Rickman, H., Bergman, P., Johansson, L.E.B., Winnberg, A., and Rauer, H.: 1998, *Earth, Moon and Planets* in press.

Bockelèe-Morvan, D., and Crovisier, J.: 1985, *Astron. Astrophys.* **151**, 90.

Bockelèe-Morvan, D., and Crovisier, J.: 1987, in *Proc. Symp. on the Diversity and Similarity of Comets*, **ESA SP 277**, p. 235.

Bockelèe-Morvan, D.,Wink, J., Despois, D., Colom, P., Biver, N., Crovisier, J., Gautier, D., Gèerard, E., Germain, B., Lellouch, E., Moreno, R. Paubert, G., Rauer, H., Davies, J.K., and Dent, W.R.F.: 1998, *Earth, Moon and Planets* in press.

Boice, D.C., Benkhoff, J., and Laffont, C.: 1998, *Earth, Moon and Planets* in press.

Budzien, S.A., Festou, M.C., and Feldman, P.D.: 1994, *Icarus* **107**, 164.

Colom, P., Gèrard, E., Crovisier, J., Bockelèe-Morvan, D., Biver, N., and Rauer, H.: 1998, *Earth, Moon and Planets* in press.

Cochran, A.L.: 1985, *Ap. J.* **289**, 388.

Cochran, A.L., and Schleicher, D.G.: 1993, *Icarus* **105**, 235.

Cochran, A.L. and Trout, A.P.: 1994, *A. J.* **108**, 1471.

Combi, M.R.: 1980., *Ap. J.* **241**, 830.

Combi, M.R.: 1987, *Icarus* **71**, 178.

Combi, M.R.: 1989, *Icarus* **81**, 41.

Combi, M.R.: 1994, *A. J.* **108**, 304.

Combi, M.R. and Cochran, A.L.: 1997, *Bull. A. A. S.* **29**, 1043.

Combi, M.R. and Delsemme, A.H.: 1980, *Ap. J.* **237**, 641.

Combi, M.R. and Delsemme, A.H.: 1986, *Ap. J.* **308**, 472.

Combi, M.R. and Feldman, P.D.: 1993, *Icarus* **105**, 557.

Combi, M.R. and U. Fink.: 1997, *Ap. J.* **484**, 879.

Combi, M.R. and Smyth, W.H.: 1988, *Ap. J.* **327**, 1044.

Cosmovici, C,B., Schwarz, G., Ip, W.-H., and Mack, P.: 1988, *Nature* **332**, 705.

Crifo, J.F.: 1991, in *Comets in the Post-Halley Era*, ed. R.L. Newburn et al. (Kluwer, Dordrecht), p. 937.

Crifo, J.F., Itkin, A.L., and Rodionov, A.V.: 1995, *Icarus*, **116**, 77.

Crifo, J.F., Itkin, A.L., and Rodionov, A.V.: 1997, *Icarus*, **127**, 319.

Crifo, J.F., Itkin, A.L., and Rodionov, A.V.: 1998, *(submitted)*.

Delsemme, A.H.: 1982, in *Comets*, ed. L.L Wilkening (Tucson: Univ. Arisona Press), p. 85.

Delsemme, A.H. and Miller, D.C.: 1971, *Planet. Space Sci. D.C.*, **19**, 1259.

DeZeeuw, D.L. and Powell, K.G.: 1992, *J. Comp. Phys.*, **104**, 55.

DiSanti, M.A., Mumma, M.J. , Dello Russo, N., Magee-Sauer, K., Rettig, T. and Novak., R.: 1998, *Earth, Moon and Planets* in press.

Eberhardt, P. et al.: 1987, *Astron. Astrophys.* **187**, 481.

Festou, M.C.: 1981, *Astron. Astrophys.* **95**, 69.

Festou, M.C., Barele, O., Davidge, T., Stern, S.A., Tozzi, G.P., Womack, M., and Zucconi, J.M.: 1998, *Earth, Moon and Planets* in press.

Fink, U. Combi, M.R., and DiSanti, M.A.: 1991, *Ap. J.* **383**, 371.,

Finson, M.L. and Probstein, R.F.: 1968, *Ap. J.* **154**, 353.

Fitzsimmons, A. and Cartwright, I.M.: *MNRAS* **278**, 37.

Fulle, M., Bosio, S., Cremonese, G., Cristaldi, S., Liller, W., and Pansecchi, L.: 1993, *Astron. Astrophys.* **272**, 634.

Fulle, M., Mikuz, H., and Bosio, S.: 1997, *Astron. Astrophys.* **324**, 1197.

Gombosi, T.I.: 1986, in *Exploration of Halley's Comet*, vol. II, ESA SP-250, p. 167.

Gombosi, T.I., DeZeeuw, D.L., Häberli, R.M., and Powell, K.G.: 1996, *J. Geophys. Res.* **101**, 15333.

Gombosi, T.I., Hansen, K.C., DeZeeuw, D.L., Combi, M.R., and Powell, K.G.: 1998, *Earth, Moon and Planets* in press.

Gombosi, T.I., Nagy, A.F., and Cravens, T.E.: 1986, *Rev. of Geophysics* **24**, 667.

Häberli, R.M., Combi, M.R., Gombosi, T.I., DeZeeuw, D.L. and Powell, K.G.: 1997, *Icarus* **130**, 373.

Häberli, R.M., Gombosi, T.I., DeZeeuw, D.L. Combi, M.R., and Powell, K.G.: 1997, *Sciences* **276**, 939.

Harris, W.M., Combi, M.R., Honeycutt, R.K., Mueller, B.E.A. and Scherb, F.: 1997, *Science* **277**, 676.

Hayward; T.L., and Hanner, M. S.: 1997, *Science* **275**, 1907.

Huebner, W.F., and Keady, J.J.: 1983, in *International Conference on Cometary Exploration*, Hungarian Academy of Sciences, Budapest, p. 165.

Huebner, W.F., Snyder, L.E., and Buhl, D.: 1974, *Icarus* **23**, 580.

Huggins, W.: 1882.*Proc. Roy. Soc.* **33**, 1.

Ip, W.-H.: 1983, *Ap. J.* **264**, 726.

Ip, W.-H.: 1989, *Ap. J.* **346**, 475.

Jackson, W.M.: 1976, in *The Study of Comets NASA SP-393* (Greenbelt, MD: NASA), 679.

Jackson, W.M.: 1991, in *Comets in the Post-Halley Era*, ed. R.L. Newburn, Jr. et al. (Dordrecht: Kluwer), 313.

Jewett, D. and Luu J.: 1989, *A. J.* **97**, 1766.

Jewett, D.C. and Meech, K.J.: 1987, *Ap. J.* **317**, 992.

Jewett, D., Senay, M., and Matthews, H.: 1996, *Science* **271**, 1110.

Kabin, K., Gombosi, T.I., Combi, M.R., DeZeeuw, D.L., and Powell, K.G.: 1998, in preparation.

Keller, H.U. et al.: 1986,*Astron. Astrophys.* **187**, 807.

Keller, H.U., Marconi, M.L., and Thomas, N.: 1990, *Astron. Astrophys.* **227**, L1.

Khare, B.N., Sagan, C., Arakawa, E.T., Suits, F., Calcott, T.A., and Williams, M.W.: 1984, *Icarus* **60**, 127.

Kidger, M.R., Serra-Ricart, M., Bellot,-Rubio, L.R., and Casas, R.: 1996, *Ap. J.* **461**, L119.

Kitamura, Y.: 1986, *Icarus* **66**, 241.

Klavetter, J.J. and A'Hearn, M.F.: 1994, *Icarus* **107**, 322.

Konno, I., Huebner, W.F., and Boice, D.C.: 1993, *Icarus* **101**, 84.

Korsun, P.P., Davis, S.P., Shavrina, A.V., Vasiljeva, I.E., Malanushenko, V.P., and Savanov, I.S.: 1998, *Earth, Moon and Planets* in press.

Körösmezey, A. and Gombosi, T.I.: 1990, *Icarus* **84**, 118.

Lamy, P. and Perrin, J.-M.: 1988, *Icarus* **76**, 100.

Laffont, C., Rousselot, P., Clairemidi, J., and Moreels, G.: 1998, *Planet. and Sp. Sci.* (in press).

Laffont, C., Rousselot, P., Clairemidi, J., Moreels, G. and Boice, D.C.: 1998, *Earth, Moon and Planets* in press.

Larson, S., and Hergenrother, C.: 1998, *Earth, Moon and Planets* in press.

Lamy, P.L. and Perrin, J.-M.: 1987, *Icarus* **76**, 100.

Lederer, S.M., Osip, D.J., Campins, H., and Schleicher, D.G.: 1998, *Earth, Moon and Planets* in press.

Marconi, M.L. and Mendis, D.A.: 1984 *Ap. J.*, **287**, 445.

Meier, R., Eberhardt, P., Krankowsky, D., and Hodges, R.R.: 1993, *Astron. Astrophys.* **277**, 677.

Millis, R.L. and Schleicher, D.G.: 1986, *Nature* **324**, 646.

O'Dell, C.R., Robinson, R.R., Krishna Swamy, K.S., McCarthy, P.J., and Spinrad, H.: 1988, *Ap. J.* **334**, 476.

Potter, A.E. and DelDuca, B.: 1964, *Icarus* **3**, 103.

Probstein, R.F.: 1968, in *Problems of Hydrodynamics and Continuum Mechanics*, Society for Industrial and Applied Mathematics, Philadelphia, p. 568.

Rauer, H., Arpigny, C., Boehnhardt. H., Colas. F., Crovisier, J. Jorda, L., Küppers, M., Manfroid, J., Rembor. K., and Thomas, N.: 1997, *Science* **275**, 1909.

Roussellot, P., J. Clairemidi. and Moreels G.: 1994, *Astron. Astrophys.* **286**, 645-653.

Samarasinha, N.H. and Belton, M.J.S.: 1994, *Icarus* **108**, 103

Samarasinha, N.H., Mueller, B.E.A., and Belton, M.J.S.: 1998, *Earth, Moon and Planets* in press.

Senay, M.C., Rownd, B., Dickens, J.E., DeVries, C.H., F.P. Schloerb, Mayhew, L., Yuen, L., and Mauskopf, P.: 1998, *Earth, Moon and Planets* in press.

Schleicher, D.G., Lederer, S.M. Millis, R.L., and Farnham, L. *Science* **275**, 1913.

Schulz, R. and A'Hearn, M.F.: 1995, *Icarus* **115**, 191.

Schulz, R. , A'Hearn, M.F., Birch, P.V., Bowers, C., Kempin, M., and Martin, R.: 1993a, *Icarus* **104**, 206.

Schulz, R. , McFadden, L.A., Chamberlin, A.B., A'Hearn, M.F., and Schleicher, D.G.: 1994, *Icarus* **109**, 145.

Schulz, R. , A'Hearn, M.F., and Samarasinha, N.H.: 1993b, *Icarus* **103**, 391.

Sekiguchi, T., Watanabe, J., Fukushima, H., and Tamamoto, N.: 1998, *Earth, Moon and Planets* in press.

Smyth, W.H., Combi, M.R., Roesler, F.L., and Scherb, F.: 1995, *Ap.J.* **440**, 349.

Thomas, N. and Keller, H.U.: 1990.*Astron. Astrophys.* **249**, 258.

Wagner, R.M. and Schleicher, D.G.: 1997, *Science* **275**, 1918.

Wallace, LV., and Miller F.D.: 1958.*A.J.* **63**, 213.

Weaver, H.A., Feldman, P.D., A'Hearn, M.F., Arpigny, C., Brandt, J.C., Festou, M.C., Haken, M., McPhate, J.B., Stern, S.A., Tozzi, G.P.: 1997, *Science* **275**, 1900.

Whipple, F.L., and Huebner, W.F.: 1976, *Ann. Rev. Astron. Astrophys.* **14**, 143.

Wink, J., Bockelèe-Morvan, D., Despois, D., Colom, P., Biver, N., Crovisier, J., Gèrard, E., Lellouch, E., Davies, J.K., Dent, W.R.F., and Jorda, L.: 1998, *Earth, Moon and Planets* in press.

Womack, M., Festou, M.C., and Stern, S.A.: 1997, *A. J.* **114** 2789.

Wyckoff, S., Tegler, S., Wehinger, P.A., Spinrad, H., and Belton, M.J.S.: 1988, *Ap. J.* **325**, 927.

Yamamoto, T.: 1981, *Moon and Planets* **24**, 453.

Address for correspondence: Michael R. Combi, 1417A Space Research Building, The University of Michigan, Ann Arbor, MI 48109-2143, USA, Voice: 1-(734)-764-7226, Fax: 1-(734)-647-3047, mcombi@umich.edu.

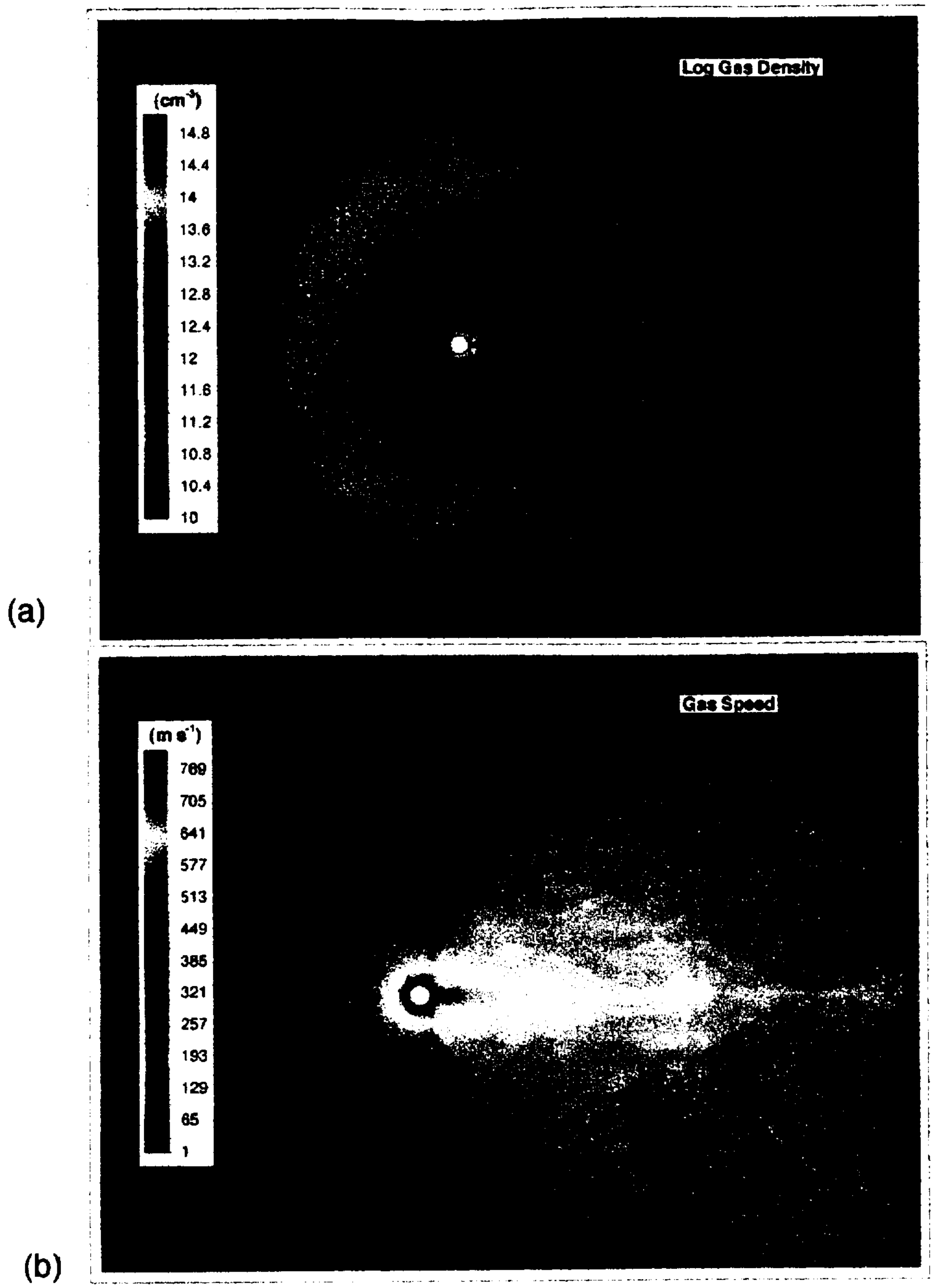

Figure 3. Plate 1. 3D Dusty-Gasdynamic Model of a Dust-Gas Jet. Shown are (a) the number density of gas and (b) the speed of the gas. The calculation corresponds to comet Hale-Bopp at ~1 AU. The jet is directed toward the right.

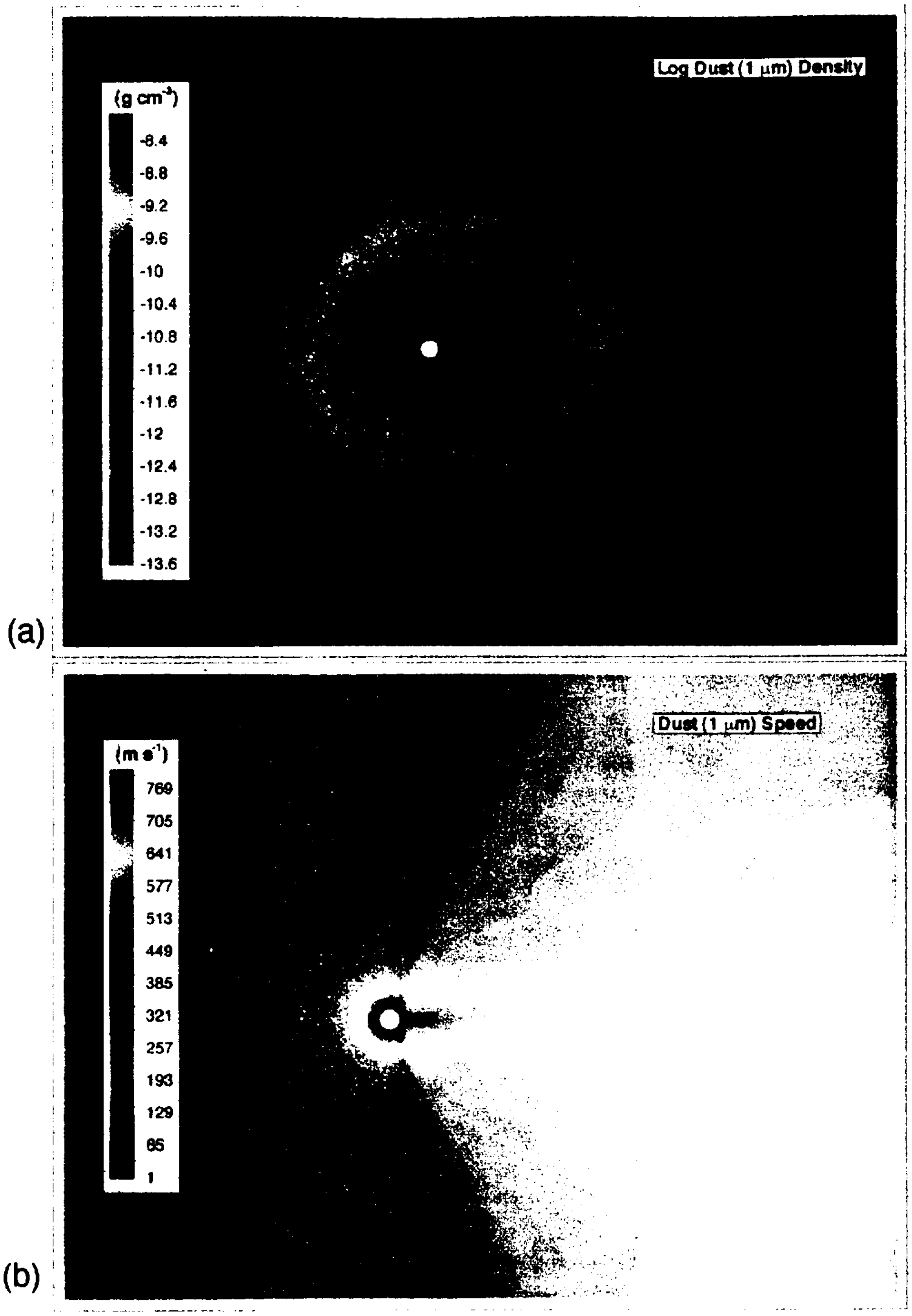

Figure 4. Plate 2. 3D Dusty-Gasdynamic Model of a Dust-Gas Jet. Shown are (a) the bulk mass density and (b) the speed for the 1 μm dust particles. The calculation corresponds to comet Hale-Bopp at ~1 AU. The jet is directed toward the right.

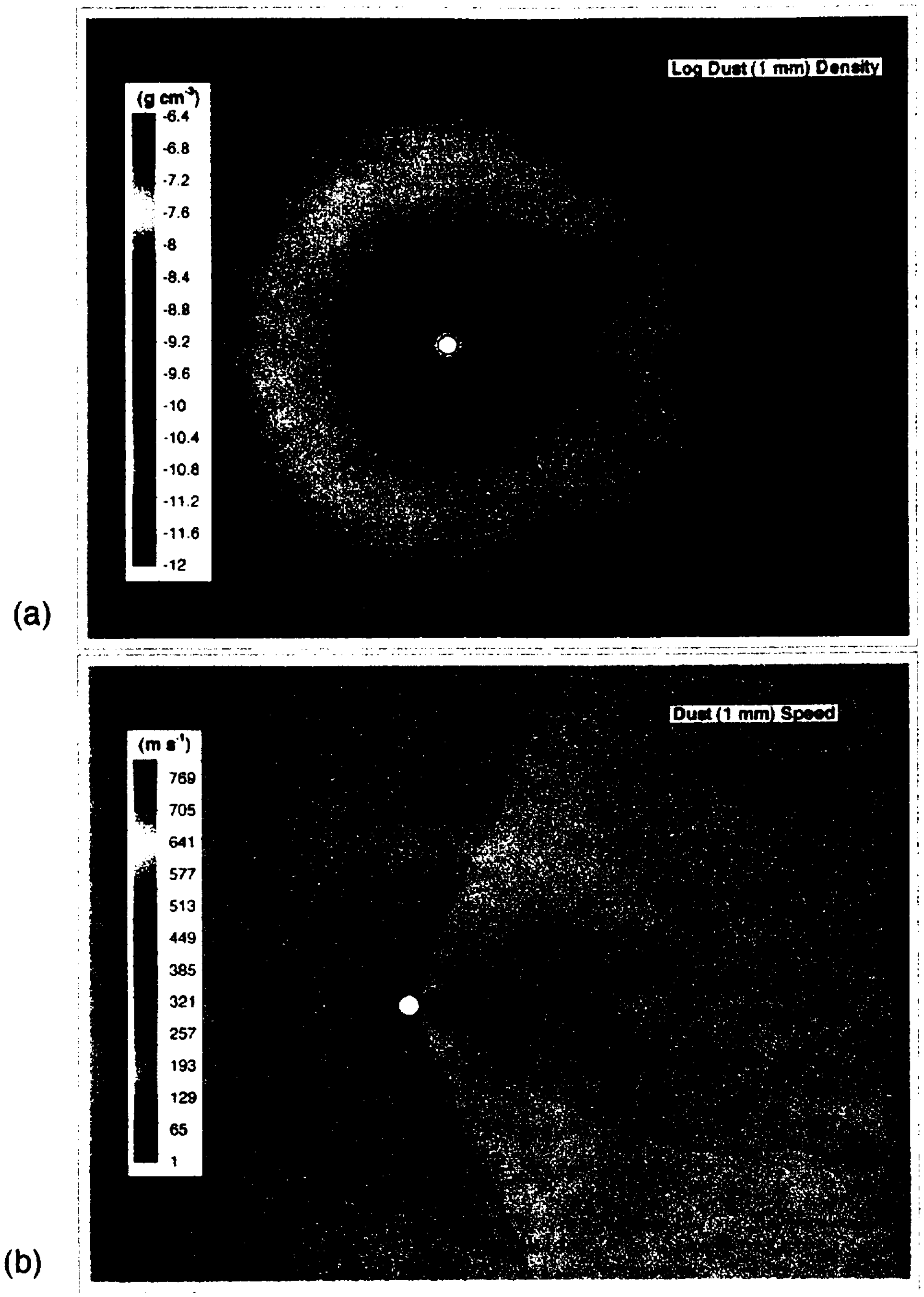

Figure 5. Plate 3. 3D Dusty-Gasdynamic Model of a Dust-Gas Jet. Shown are (a) the bulk mass density and (b) the speed for the 1 mm dust particles. The calculation corresponds to comet Hale-Bopp at ~1 AU. The jet is directed toward the right.

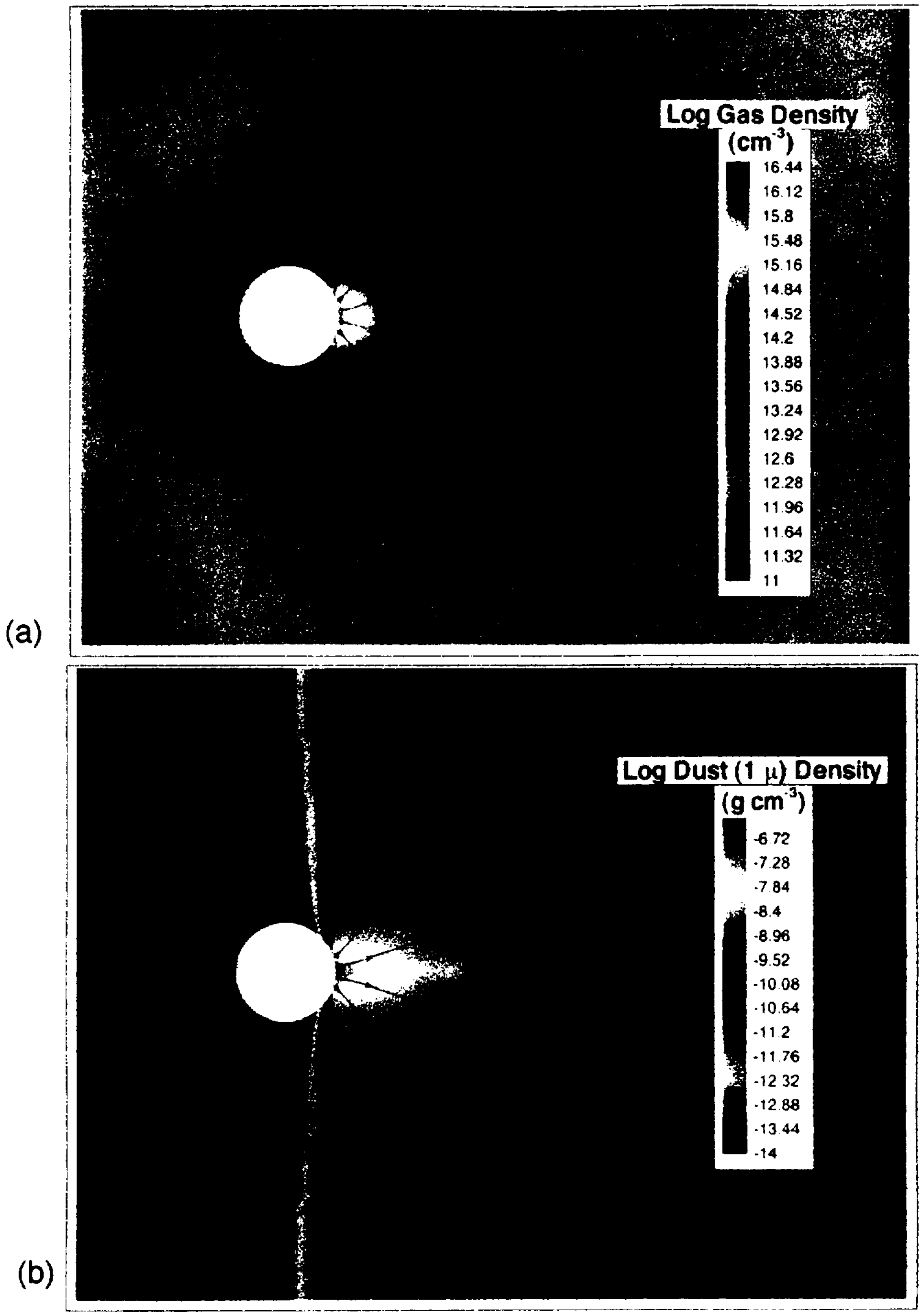

Figure 6. Plate 4. 3D Dusty-Gasdynamic Model of a Strong Dust-Gas Jet. Shown are (a) the number density of the gas and (b) the bulk mass density for optical 1 μm particles in the vicinity of a strong jet, directed toward the right.

JOURNAL OF GEOPHYSICAL RESEARCH, VOL. 103, NO. A5, PAGES 9071-9081, MAY 1, 1998

Io's plasma environment during the Galileo flyby: Global three-dimensional MHD modeling with adaptive mesh refinement

M. R. Combi, K. Kabin, T. I. Gombosi, and D. L. DeZeeuw
Space Physics Research Laboratory, University of Michigan, Ann Arbor

K. G. Powell
Department of Aerospace Engineering, University of Michigan, Ann Arbor

Abstract. The first results for applying a three-dimensional multiscale ideal MHD model for the mass-loaded flow of Jupiter's corotating magnetospheric plasma past Io are presented. The model is able to consider simultaneously physically realistic conditions for ion mass loading, ion-neutral drag, and intrinsic magnetic field in a full global calculation without imposing artificial dissipation. Io is modeled with an extended neutral atmosphere which loads the corotating plasma torus flow with mass, momentum, and energy. The governing equations are solved using adaptive mesh refinement on an unstructured Cartesian grid using an upwind scheme for MHD. For the work described in this paper we explored a range of models without an intrinsic magnetic field for Io. We compare our results with particle and field measurements made during the December 7, 1995, flyby of Io, as published by the Galileo Orbiter experiment teams. For two extreme cases of lower boundary conditions at Io, our model can quantitatively explain the variation of density along the spacecraft trajectory and can reproduce the general appearance of the variations of magnetic field and ion pressure and temperature. The net fresh ion mass-loading rates are in the range of ~300-650 kg s^{-1}, and equivalent charge exchange mass-loading rates are in the range ~540-1150 kg s^{-1} in the vicinity of Io.

1. Introduction

Io's interaction with Jupiter's corotating inner magnetosphere has been studied for over 25 years. Io has a neutral atmosphere which is probably locally thick but rather uneven across its surface [*Lellouch et al.*, 1992; *Ballester et al.*, 1994]. The ultimate source for atmospheric gases appears to be the numerous active volcanoes on the surface. It is the energetic particle environment near Io which is responsible for the balance of the plasma heating, Joule heating, ionization, and surface and atmospheric sputtering, and which in some form drives the escape of the neutral atmosphere [*Schneider et al.*, 1989]. A realistic model for the flow of magnetospheric plasma, interacting with Io's neutral atmosphere is necessary for a complete understanding of the global picture.

The results of the measurements by the particle and field instruments on the Galileo Orbiter during the December 1995 flyby of Io provide new and important information with which a realistic MHD simulation for the plasma interaction can be tested. *Kivelson et al.* [1996a,b] have recently suggested that an intrinsic magnetic field for Io with a strength and direction which would nearly cancel the local Jovian field near the surface of Io, can explain many aspects of the Galileo magnetometer measurements taken during the December 1995 flyby of Io. However, the large plasma densities and low temperatures measured at the same time by the Galileo plasma science package [*Frank et al.*, 1996] and the plasma wave instrument [*Gurnett et al.*, 1996], indicate that ion mass loading is significant and may provide an explanation for the magnetic field measurements without requiring an intrinsic field.

Our understanding of the interaction of Io with Jupiter's magnetosphere goes back to the discovery of Io-related decametric radio emission discovered by *Bigg* [1964] and the unipole inductor model which explains it [*Goldreich and Lynden-Bell* 1969]. There have been a number of theoretical studies of this interaction during the immediate post-Voyager era [e.g., *Southwood et al.*, 1980; *Neubauer*, 1980] (see also *Hill et al.* [1983] for an excellent post-Voyager review). *Neubauer* [1980] presented an analytical model of Alfvén standing wave current system which connects current through the ionosphere of Io. *Southwood et al.* [1980] examined data from several Voyager instruments and examined the possible role of an intrinsic magnetic field for Io as a way to retain a robust enough ionosphere to provide enough conductivity for completing the Io-Jupiter current circuit. Early theoretical work was often done either in the context of a "thin" atmosphere [e.g., see *Cloutier et al.*, 1978] indicative of the surface temperature (~130 K), or "thick" extended neutral atmosphere [e.g., see *Goertz*, 1980] more indicative of volcanic

Paper number 98JA00073.
0148-0227/98/98JA-00073$09.00

temperatures (~1000 K). Subsequent evidence [*Sieveka and Johnson*, 1985; *Schneider et al.*, 1991; *Lellouch et al.*, 1992; *Ballester et al.*, 1994; *Belton et al.*, 1996] seems to indicate a mixed picture of the global atmosphere, which has a large extended corona like a thick atmosphere, but appears to be dominated by local major injection of hot (high speed) gas/dust plumes to high altitudes but only near active volcanic vents. Therefore, although the atmosphere is probably only locally thick, it still has a large extended neutral corona which might provide a sufficient source of impact ionization and photoionization.

There have been a number of three-dimensional (3-D) numerical studies of the plasma flow past Io [*Linker et al.*, 1988, 1989, 1991; *Wolf-Gladrow et al.*, 1987]. Because of the complexities in the problem and numerical difficulties, studies have been limited to restricted portions of the problem, have introduced fixes such as artificial viscosity, or have been run using less than fully physically realistic conditions. *Linker et al.* [1991] have performed the best example to date of 3-D MHD modeling of Io. In this model they used the two-step Lax-Wendroff method. These calculations were performed on a nonuniform but fixed structured grid, and artificial dissipative terms (artificial viscosity) had to be introduced to the basic MHD equations in order to make them computational stable.

A new numerical method has been developed at the University of Michigan for solving the full 3-D MHD equations which resolves a number of difficulties that have plagued past attempts. The 3-D version of this new method, called multiscale adaptive upwind scheme for MHD (MAUS-MHD), has already been applied to the full comet-solar wind interaction problem and has been discussed in detail by *Gombosi et al.* [1996]. This interaction is quite similar to that expected for the Io-Jupiter-magnetosphere interaction in the absence of an intrinsic magnetic field for Io. A full Earth magnetosphere version of the same calculation has also recently been developed [*De Zeeuw et al.*, 1996], so the method is also able to treat intrinsic magnetic fields as well, if necessary. We can and have run test cases with an intrinsic field for Io, but in this paper, concentrate on trying to explain the existing data with nonintrinsic field models.

2. Model Description

In the 3-D MAUS-MHD model the calculation is done on an unstructured Cartesian grid using octree adaptive mesh refinement (AMR). This makes optimal use of computer resources allowing problems with disparate scales and unusual and varying geometries to be modeled globally, while still retaining sufficient resolution locally to capture shocks and other important features resulting from naturally occurring sharp gradients in the flow. The octree structure is a hierarchical cell structure, based on multiple generations of cubic parent cells which can be split into eight daughter cells. The adaptive data structure has been explained by *DeZeeuw and Powell* [1992]. The approximate eight-wave Riemann solver for ideal MHD is combined with a second-order MUSCL-type scheme [*van Leer*, 1979]. It uses a novel approach to handle the "div **B** problem" derived and discussed at length by *Powell* [1994] and *Powell et al.* [1995, also Multiscale adaptive upwind scheme for magnetohydrodynamics; MAUS-MHD, manuscript in preparation, 1998]. In this scheme div **B**/r is treated as a passive scalar so that any numerically generated nonzero contributions are convected away. Once div **B** = 0 is imposed as an initial condition to the problem it is satisfied to within truncation error.

Our model of Io's interaction with Jupiter's magnetosphere is essentially similar to the comet problem of *Gombosi et al.* [1996]. The dimensionless conservative form of the ideal MHD equations can be written as

$$\frac{\partial \tilde{\mathbf{W}}}{\partial \tilde{t}} + \left(\nabla \cdot \tilde{\mathbf{F}}\right) = \tilde{\mathbf{S}} \tag{1}$$

where W and S are eight-dimensional state and source vectors, while F is an 8 x 3 dimensional flux diad. All quantities denoted by a tilde are normalized by physical quantities in the undisturbed upstream region

$$\tilde{t} = a_\infty t / R_{Io} \tag{2a}$$

$$\tilde{\mathbf{r}} = \mathbf{r} / R_{Io} \tag{2b}$$

$$\tilde{\rho} = \rho / \rho_\infty \tag{2c}$$

$$\tilde{\mathbf{u}} = \mathbf{u} / a_\infty \tag{2d}$$

$$\tilde{p} = p / \rho_\infty a_\infty^2 \tag{2e}$$

$$\tilde{\mathbf{B}} = \mathbf{B} / \sqrt{\mu_0 \rho_\infty a_\infty^2} \tag{2f}$$

where *t* is time, ***r*** is radius vector, *ρ* is mass density, ***u*** is bulk flow velocity, *p* is pressure, μ_0 is the permeability of free space, and ***B*** is magnetic field vector. The subscript ∞ refers to values in the undisturbed upstream flow. Finally, R_{Io} is the radius of Io and a_∞ is the hydrodynamic sound speed in the undisturbed upstream plasma flow.

The normalized state and flux vectors are written as

$$\tilde{\mathbf{W}} = \begin{pmatrix} \tilde{\rho} \\ \tilde{\rho}\tilde{\mathbf{u}} \\ \tilde{\mathbf{B}} \\ \tilde{\varepsilon} \end{pmatrix} \tag{3a}$$

$$\tilde{\mathbf{F}} = \begin{pmatrix} \tilde{\rho}\tilde{\mathbf{u}} \\ \tilde{\rho}\tilde{\mathbf{u}}\tilde{\mathbf{u}} + \left(\tilde{p} + \frac{1}{2}\tilde{B}^2\right)\mathbf{I} - \tilde{\mathbf{B}}\tilde{\mathbf{B}} \\ \tilde{\mathbf{u}}\tilde{\mathbf{B}} - \tilde{\mathbf{B}}\tilde{\mathbf{u}} \\ \tilde{\mathbf{u}}\left(\tilde{\varepsilon} + \tilde{p} + \frac{1}{2}\tilde{B}^2\right) - \left(\tilde{\mathbf{B}} \cdot \tilde{\mathbf{u}}\right)\tilde{\mathbf{B}} \end{pmatrix} \tag{3b}$$

where $\tilde{\varepsilon}$ is the normalized internal energy density

$$\tilde{\varepsilon} = \frac{1}{2}\left[\tilde{\rho}\tilde{\mathbf{u}} \cdot \tilde{\mathbf{u}} + \frac{2\tilde{p}}{\gamma - 1} + \tilde{B}^2\right] \tag{4}$$

The source vector in (1) corresponding to ion mass-loading, M, is of the same form as used by *Gombosi et al.* [1996], and is given in normalized units as

$$\tilde{S} = \begin{pmatrix} \dot{M} \\ \left(\dot{M}+\eta\tilde{\rho}\right)\tilde{u}_n - \eta\tilde{\rho}\tilde{u} \\ 0 \\ \frac{1}{2}\left(\dot{M}+\eta\tilde{\rho}\right)\tilde{u}_n{}^2 - \eta\left(\frac{1}{2}\tilde{\rho}\tilde{u}^2 + \frac{1}{\gamma-1}\tilde{p}\right) \end{pmatrix}, \qquad (5)$$

where

$$\dot{M} = \frac{m_c}{\rho_\infty}\frac{R_{Io}}{a_\infty}Q_i\left(\frac{R_{Io}}{r}\right)^{\alpha},$$

$$\eta = \frac{R_{Io}}{a_\infty}F_{in}\left(\frac{R_{Io}}{r}\right)^{\alpha}.$$

Q_i is the ionization rate per unit volume evaluated at Io's radius; F_{in} is the ion-neutral collision momentum-energy transfer rate per unit volume, also evaluated at Io's radius. In the simplest interpretation $Q_i(R_{Io}/r)^{\alpha}$ is given by the neutral density, n_n, divided by τ_i, the ionization timescale for neutrals, and $F_{in}(R_{Io}/r)^{\alpha}$ is given by $n_n k_{in}$, where k_{in} is the ion-neutral momentum transfer collision rate, and n_n is the neutral density. The choice for the exponent, α, is discussed below. For the Io cases presented here the net neutral flow velocity, u_n, is taken to be zero. This could be generalized in the future to account for a net escaping neutral atmosphere at high altitudes.

For the Io version of the MAUS-MHD model simulations were performed both for a pure conducting sphere with and without ion mass loading and for a sphere with fixed boundary conditions, as discussed in detail below. The simulation volume is 900 x 600 x 600 R_{Io}, and there are 9 levels of refinement and 92,000 cells with sizes ranging from < 0.1 R_{Io} near Io to 50 R_{Io} far upstream and downstream. We have chosen the upstream plasma conditions as follows from our best estimates of the Galileo December 1995 epoch, including the various recently published Galileo measurements (see Table 1). Since the calculation is performed in normalized units, there is some flexibility to rescale the results over a range of realistic conditions, but this cascades to other parameters [see, e.g., *Gombosi et al.*, 1996]. We have investigated numerous versions of cases for a simple conducting sphere, a mass-loading ionosphere, and with an intrinsic magnetic field for Io.

The formulation of mass loading for comets [*Gombosi et al.*, 1996] permits us to incorporate both the effects of mass loading from new ionization (impact and photoionization) as well as momentum and energy loading from charge exchange and nonreactive ion-neutral collisions. In the comet calculation Gombosi et al. used the term "ion-neutral friction" to describe the effect of collisions which cause momentum and energy exchange but which result in no new ions. The dominant source of such an exchange of momentum and energy results from symmetric charge exchange reactions involving the dominant torus ions and atmospheric neutrals (O^+ + O, S^+ + S, and S^{++} + S). *Linker et al.* [1991] appropriately included an ion mass loading rate and a "charge exchange rate" in their MHD models. However, many nonreactive collisions between ions and atmospheric neutrals also can exchange momentum and energy without yielding net new ion mass. These so-called knock-on collisions are important for producing the extended neutral corona of Io [*Sieveka and Johnson*, 1985; *Johnson*, 1990]. Furthermore, it has been shown by *Smyth and Combi* [1997] that the distribution of sodium in the corona [*Schneider et al.*, 1991] as well as the more familiar B-cloud is a natural outcome of the collisional cascade process (incomplete atmospheric sputtering) that is initiated by such collisions. For simplicity in the remainder of this paper this momentum-energy loading term is referred to as the charge exchange rate.

Table 1. Upstream Plasma Conditions

Parameter	Value
Upstream plasma density	3500 cm^{-3}
Upstream plasma temperature	92 eV
Upstream mean molecular mass	22 amu
Upstream magnetic field	1800 nT
Corotation flow speed	56.8 km s^{-1}
Alfvénic Mach number	0.4
Mach number	2.2
Ratio of specific heats (γ)	1.667

On the basis of Voyager-era conditions, *Smyth* [1992] has estimated a total collision rate of ~2 x 10^{28} s^{-1} between incident plasma torus ions and neutrals in Io's atmosphere with about 1/3 yielding fresh ions deposited into the plasma flow and the rest contributing to momentum/energy exchange alone, i.e., the charge exchange rate. These estimates are based on extrapolations of knowledge gained about the extended sodium atmosphere of Io to the more abundant neutral species S, O, SO, and SO_2. On the basis of their own estimates, *Linker et al.* [1989, 1991] have explored MHD models with a comparable charge-exchange rate but with a fresh ion mass-loading rate nearly an order of magnitude smaller (~10^{27} s^{-1}) than Smyth's. Based on the then non-detection of optical/UV emissions close to Io, *Shemansky* [1980] provided an upper limit to the fresh ion mass-loading rate of ~10^{27} s^{-1}. *Smyth and Shemansky* [1983] later raised this to 4 x 10^{27} s^{-1} after subsequent detections of neutral O and S emissions from ground-based and space-based remote measurements. It is also likely that the torus is more robust in recent years, and that mass, momentum, and energy input rates may all be higher now than 17 years ago. This appears to be borne out by comparisons between Galileo measurements during the December 1995 flyby and Voyager measurements [*Frank et al.*, 1996; *Gurnett et al.*, 1996].

As is evidenced by the range of values which appear in the literature, making an independent estimate for ion mass loading and charge exchange rates is difficult, because they are based on a number of uncertain and indirect measurements and assumptions. With the availability of the Galileo PLS measurements [*Frank et al.*, 1996] of plasma density, temperature, and pressure we have adopted the different approach of using the net ion mass-loading and charge exchange rates as adjustable parameters and constraining the values based on comparison of our model results with the measurements along the spacecraft track.

SO_2 appears to be the major primary constituent in Io's atmosphere [*Ballester et al.*, 1994; *Lellouch et al.*, 1992], but observations still to date only provide hemispherically averaged total column abundances. The sodium eclipse measurements of *Schneider et al.* [1991] are the only unambiguous information we have about the vertical distribution of neutral gas species in the corona of Io from about 1.4 to about 6 R_{Io}. The interpretation of recent Hubble observations of various UV emissions of atomic S and O [*Ballester et al.*, 1996] is complicated by the fact that the spatial distributions of the emissions are determined by a combination of the mass distribution in the atmosphere with excitation by the plasma density and temperature environment. Theoretical and empirical models have explored the structure of the neutral atmosphere and its behavior to various gas sources and energetic heating and ejection processes, such as sublimation, volcanic ejection, surface and atmospheric sputtering, UV, plasma, and Joule heating, and LTE and non-LTE IR radiative cooling [*Sieveka and Johnson*, 1985; *McGrath and Johnson*, 1987; *Moreno et al.*, 1991; *Strobel et al.*, 1994; *Pospiezalska and Johnson*, 1996; *Wong and Johnson*, 1995; *Smyth and Combi*, 1997]. Despite recent advances in observational and theoretical work, still only a rough sketch of the structure of the neutral atmosphere can be made.

For our MHD simulations we have adopted ion mass, momentum, and energy loading source terms in the vicinity of Io as if proportional to the neutral density distribution which is scaled as a power law in distance (r/R_{Io}) with an exponent, α. We do not need to specify the neutral density itself, however, just the ionization mass and momentum/energy exchange rates and their dependence on distance. We have adopted the power law with an exponent of $\alpha \sim -3.5$ as found by *Schneider et al.* [1991] for the trace species, sodium, outside about 1.4 R_{Io}. *Smyth and Combi* [1997] have shown that this vertical distribution of sodium from the *Schneider et al.* [1991] eclipse observations and the more typical emission profiles of more spatially extended sodium can together be explained by a single modified incomplete cascade sputtering distribution, which results naturally from multiple neutral-neutral and ion-neutral collisions between torus ions and atmospheric neutrals. Therefore it is reasonable to expect a similar type distribution for neutral species in general. This power law is contrasted with the less steep inverse square-type power law distribution assumed in past MHD mass-loading calculations [*Linker et al.*, 1988, 1991]. For the mass-loading models presented here, we assume the neutral distribution has this dependence from an inner boundary at 150 km above the surface of Io, out to the Lagrange radius of 6 R_{Io}.

If details about the ion composition and electron temperature in the torus, and the global spatial distribution and composition of the neutral atmosphere were available, it would be possible to make a better estimate of the spatial distribution of the ion mass-loading rate and the charge-exchange rate (the collisional energy-momentum loading rate) needed to specify the source terms in the MHD equations. Typical cross sections [*McGrath and Johnson*, 1989] between oxygen and sulfur ions dominating the torus and O, S, and SO_2 neutrals dominating the atmosphere show that typical symmetric charge exchange reactions have cross sections in the range of 20 to 40 $Å^2$ whereas most impact ionization and elastic collisions [*Johnson*, 1990] have cross sections in the range of 1 to 20 $Å^2$. Electron impact of course only nets ion mass but is highly dependent on the electron temperature.

The power law distribution may not be correct well inside of 1.4 R_{Io} because the range of the observations of *Schneider et al.* [1991] started at this distance. At much lower altitudes the resulting ion mass-loading rate is a trade off between the likely rapid increasing of neutral density (probably more like an exponential scale height distribution), with the decreasing plasma flux (electron and ions) caused by recombination and plasma-neutral collisions themselves. *Flaser et al.* [1997] have shown preliminary results of Galileo radio occultation measurements which indicate electron densities in excess of 50,000 cm^{-3} at the peak of the ionosphere, ~50-80 km above the surface. This is similar to but higher than given by *Kliore et al.* [1974, 1975] from the Pioneer era, and again generally consistent with the more robust torus of the recent times. At this time, a fully coupled MHD-ionosphere calculation would be beset with many assumptions, for example, the neutral atmosphere density profile which is still uncertain to within a factor of a few. In any case the scope of this type of study is currently beyond the state of the art even for the Earth for which there is much more knowledge.

For the models presented in this paper we have adopted two types of lower boundary conditions which represent opposite pictures of the type of conditions present above Io's ionosphere One is a perfectly conducting impenetrable sphere. In this case both the magnetic field and the plasma flow are reflected from the lower boundary. This represents an extreme case of not allowing either plasma flow or magnetic flux to penetrate the sphere, and we hereafter refer to this as a reflecting boundary condition. The second case corresponds to fixed boundary conditions where the magnetic field and plasma density and velocity are specified in ghost cells just below the boundary. In this case both magnetic flux and plasma flow can pass through the boundary. For the fixed boundary condition model presented here the plasma density is set to a value of 3 times the upstream torus density (or 10,500 cm^{-3}) which is representative of the global spherical average indicated by radio occultation measurements at an altitude of 150 km. The plasma velocity is set to zero, being consistent with strong coupling to the neutral atmosphere. The choice of a value for the fixed magnetic field at the lower boundary requires some discussion. We hereafter refer to this case as fixed boundary conditions.

Linker et al. [1991] presented model results which solved for the full MHD equations (mass, momentum, energy, and B field) outside of Io, and only the magnetic field with a constant conductivity inside the inner boundary, throughout the interior of Io. The internal conductivity was set in such a way to obtain a high enough integrated conductivity (10-150 mhos) necessary for maintaining the Jupiter-Io current system. They point out that it is not really known where the current loops close, i.e., in the ionosphere but outside of Io, or even through the dense lower ionosphere and into a possible conducting interior. Linker et al. found, however, that the same exterior solutions could be obtained whether they performed the computationally intensive calculation of the magnetic field inside Io or whether they simply held the B field at the inner boundary constant at the background level. In fact, their full calculation showed that in any case "the magnetic field changed very little inside the sphere."

The physical interpretation for a constant magnetic field is that if Io does not have an intrinsic B field (i.e., from an internal dynamo), it would be expected that a value similar to the average imposed Jovian external field would be induced over time. We have estimated that the time-averaged value of the field at Io happens to be slightly less (~98%) than the instantaneous value at Io's position at the point of Galileo's close approach. The same ratio was found either roughly using the variation from the old *Goertz et al.* [1976] magnetic field model or more carefully using the newest model of *Connerney et al.* [New model of Jupiter's magnetic field constrained by the Io flux tube footprint, manuscript in preparation, 1998]. It is noteworthy that those models predict values that are overall too low and too high, respectively, compared with the actual values measured by Galileo [*Kivelson et al.*, 1996b].

As mentioned already for this study we have left the ion mass-loading rate and the charge exchange rate (pure momentum/energy exchange) as adjustable parameters. We then undertook an iterative procedure to vary these quantities and compare our model results with the measured plasma density, pressure, and magnetic field along the Galileo spacecraft trajectory until a reasonable (albeit not perfect) match was obtained. Upstream we assume the aforementioned torus conditions. Downstream and to the sides of the simulation box we assume absorbing boundary conditions, i.e., mass, momentum, and energy, exit, and nothing comes back. Because of the adaptive grid technology we are able to place the upstream, downstream, and lateral boundaries far enough from Io so they do not affect on the solution.

3. Model Results

To serve as a baseline, we show results for a perfectly conducting sphere without mass loading, given realistic upstream plasma torus conditions. We refer to this case as no mass loading and reflective boundary conditions. This is shown mainly for comparison with the similar nonintrinsic field model of *Kivelson et al.* [1996b], and to serve as a point of comparison with the mass-loaded cases. For this case, the only parameters to be set are the upstream Mach number of 2.2 and the upstream Alvénic Mach number of 0.4. In (5) the ion-mass and ion-neutral drag rates Q_i and F_{in} are zero. The results are scaleable to other values of upstream magnetic field and conducting radius given constraints imposed by the Mach number (which does not have a great effect on the overall global structure of the flow) and the Alfvénic Mach number (which is more critical). In any case our estimates of both the upstream Mach number and Alfvénic Mach number are consistent with the measured Galileo flyby conditions and rigid corotation.

We show results for two mass-loading cases where the particular values of the ion mass-loading rate and the charge-exchange rate serve as the adjustable parameters. We have run some models with larger exponents (-4 to -5), however, -3.5 is based on an actual measurements and is quite satisfactory. The goal is to be able to reasonably reproduce the variation of the plasma density, pressure (and temperature), and magnetic field along the spacecraft trajectory according to the results of the Galileo Io flyby results [*Frank et al.*, 1996; *Kivelson et al.*, 1996b; *Gurnett et al.*, 1996]. The sensitive features in the plasma data to be reproduced are (1) the height of the plasma density peak along the center of the wake, (2) the reduction of the magnetic field, (3) total width of the disturbance in all quantities, (4) the reversal and side peaks of the pressure and temperature, and (5) the vector velocity magnitude and direction. *Frank et al.*, [1996] have reported plasma velocities (44 km s^{-1}) that are below corotational speeds (56.8 km s^{-1}) even 4 R_{Io} from the central axis of the wake. However, these have a large enough uncertainty (-5 and +15 km s^{-1}) to be consistent with corotational speed, which seems more reasonable.

Plates 1a-1f show a comparison of slices of the magnetic field and flow streamlines in the planes parallel and perpendicular to the upstream magnetic field for the non-mass-loaded and both mass-loaded cases. In the non-mass-loaded reflective case one can see the strong influence of the Alfvén wings in the parallel plane (1a) [see *Neubauer*, 1980; *Linker et al.*, 1991] as the flow diverts around the conducting sphere and as the disturbance is directed off at the expected angle ($\tan \theta = 1/M_A$) where θ is the deflection angle and M_A is the Alfvénic Mach number. In MHD the Alfvén wings are the analog of vortex sheets of regular fluid dynamics [*Kogan*, 1961]. In the parallel plane for the mass-loading case with reflective boundary conditions (1b), the effect of the inner boundary conducting sphere, which dominates the non-mass-loaded case, is weakened but still present. Finally, in the fixed-boundary mass-loading case (1c) the effect of the Alfvén wings has all but disappeared. Plates 1d-1f show the comparable plots in the plane perpendicular to the upstream magnetic field. The December 1995 Galileo flyby trajectory lay very close to this plane. The diverted flow streamlines are not very different between any of the three cases, in fact for the two mass-loaded cases the flow fields in this plane are virtually identical. The small variations in the magnetic field magnitude are apparent. Note that in mass-loading fixed case (Plates 1c and 1f) the diversion of flow is similar in both planes.

Plates 2a, 2b & 2c show the striking differences for the plasma ion density among the various cases. The dark lines show the outlines of the octree cell structure of the adaptively refined mesh. In the non-mass-loading reflective case (2a) the flow diversion around the sphere is evident. The density concentrates somewhat along the Alfvén wings but the wake is essentially evacuated of material. The mass-loaded reflective case (2b) shows a large density pileup in the wake right behind Io and a fair dispersion of material spread in the direction parallel to the upstream magnetic field. This is caused by the strong influence of the reflective boundary conditions. The mass-loaded fixed boundary case (2c) also produces a plasma wake, but it is more concentrated along the central line of the wake, does not have the large extension along the field-parallel direction (as in Plate 2b), and is more extended along the wake.

Direct comparisons of the model with the Galileo flyby data, along the trajectory are given in Figures 1a-1d. Model results are superimposed on the measurements for both mass-loading models with reflective and fixed boundary conditions. The reduction of the magnetic field in the wake along the spacecraft trajectory is shown in Figure 1a. Both of these models provide a similar breath and depth of the magnetic field disturbance as the pure intrinsic dipole model of *Kivelson et al.*, [1996b]; i.e., the measured field disturbance is wider and deeper. The model with reflective boundary conditions yields a somewhat deeper central disturbance than the fixed boundary model, but the overall widths are nearly identical.

Figure 1b shows the plasma density compared with the measurements of *Frank et al.* [1996]. Both the peak of the density at the center of the wake and the width of the disturbance are well reproduced by both mass-loading models. In fact, the height of the plasma density was one key factor in adjusting the mass-loading rate in our process of reproducing the measurements. The plasma pressure from the model is compared with the Frank et al. data in Figure 1c and the temperature in Figure 1d. The character of the pressure/temperature disturbance is reasonably well reproduced. There is a rise to either side of a narrow central minimum. The depth and width of the central minima in pressure and temperature, which correspond well with narrow density peak, are well reproduced by both models. However, the measurements show a large increased temperature and pressure in the flanks of the wake, which roughly corresponds to the wider measured magnetic field disturbance, and which is not quantitatively reproduced by either mass-loading model. The models show smaller peaks which are closer to the central line of the wake, and the model with reflecting boundary conditions produces higher side peaks in both temperature and pressure.

The two key attributes on which we focused fitting were the height of the density peak (as mentioned above) and the central depth of the minima in temperature and pressure. Although there is some interplay in adjusting both parameters, the density peak was more sensitive to changes in the mass-loading rate, while the depths of the pressure and temperature minima were more sensitive to the charge exchange rate. For the model results shown in Plates 1 and 2 and Figure 1, the total ion mass-loading rate corresponds to 0.84 x 10^{28} and 1.8 x 10^{28} ions s^{-1} for the fixed and reflective boundary condition models, respectively, where the mean molecular mass is 22 amu and the radial distribution varied as $r^{-3.5}$. The charge exchange rate (due again to momentum/energy loading for which charge exchange is the dominant part) is equivalent to 1.5 x 10^{28} and 3.2 x 10^{28} ions s^{-1}, respectively, for comparison with the charge exchange rates given by *Linker et al.* [1991]. For the best match to the density peak and pressure reversal, the ion-neutral collision frequency was about two times the ionization rate. The 2 to 1 ratio in relative rates are in rough agreement with recent estimates by *Smyth* [1992].

This net ion mass loading corresponds to a fresh ion mass-loading rate of 300-650 kg s^{-1}. From the momentum/energy exchange rate we can generate an equivalent total apparent mass-loading rate which has contributions from both the true ionization rate as well as the momentum and energy loading from the combination of (mostly) symmetric charge exchange and non-reactive ion-neutral collisions of about 840-1800 kg s^{-1}. This total loading rate is a factor of 2-4 larger than Smyth's

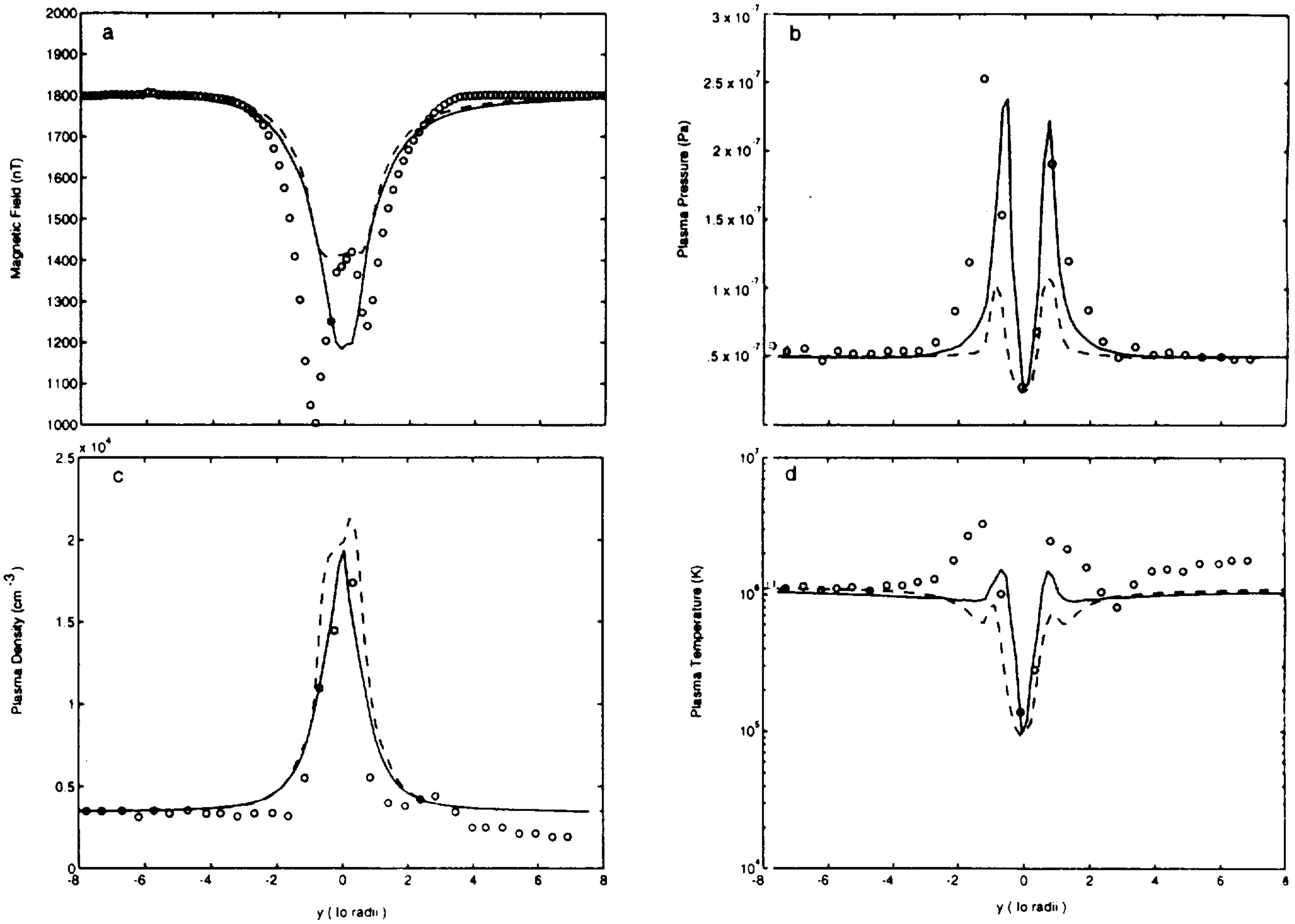

Figure 1. Comparison of the mass-loading models with Galileo particle and field measurements. The magnetic field measurements in (a) from *Kivelson et al.* [1996] are shown with the model values. The (b) plasma density, (c) pressure, and (d) temperature from the model are shown with those from *Frank et al.* [1996] obtained from the plasma ion measurements. The solid lines give the results for the model with mass-loading and reflective boundary conditions. The dashed lines give the results for the model with mass-loading and fixed boundary conditions.

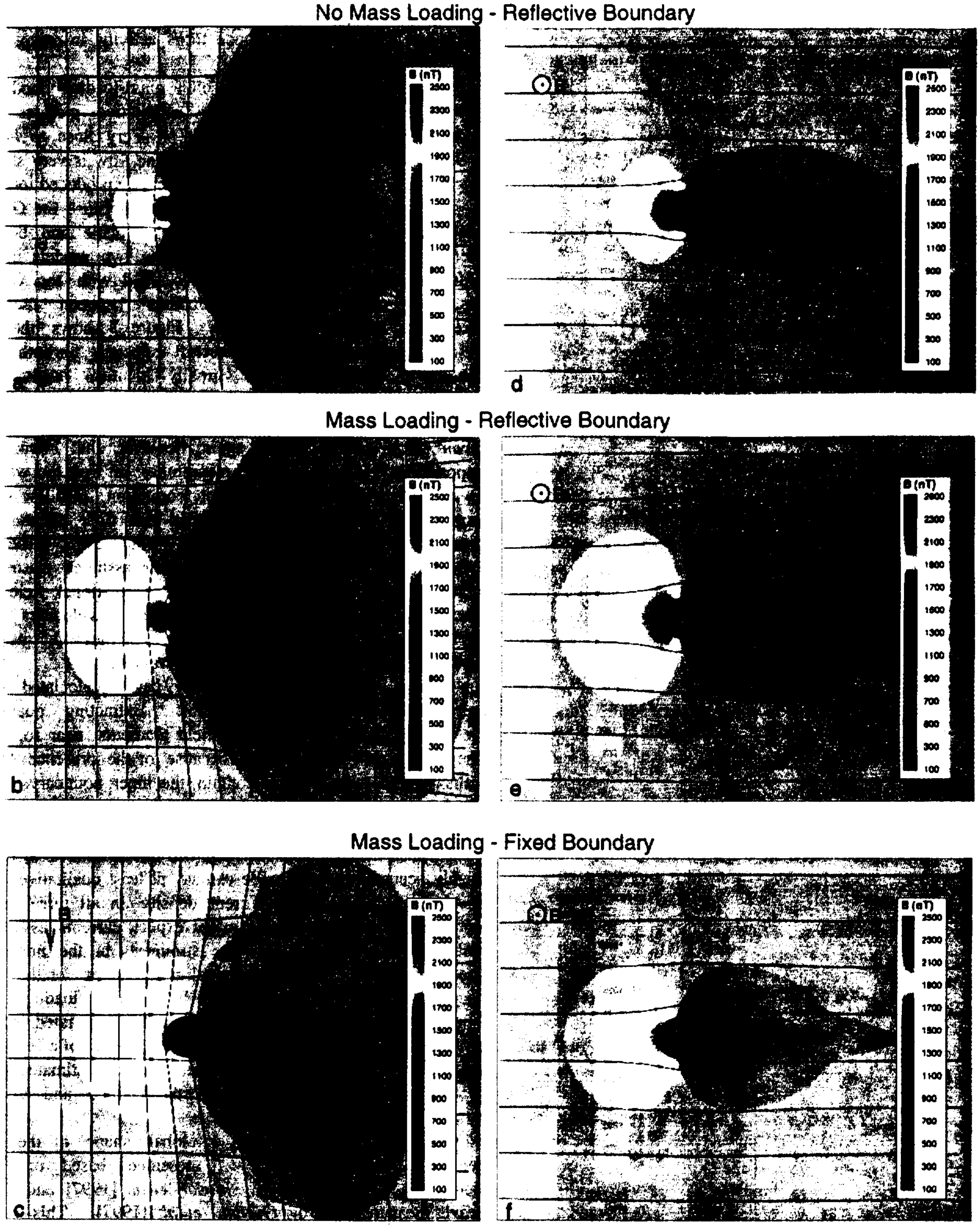

Plate 1. Magnetic field and streamlines for non-mass-loading and mass-loading flows past Io. (a)-(c) The plane aligned along the upstream magnetic field direction. The draped field lines (generally vertical lines) and velocity stream lines (generally horizontal lines with arrows) are shown. (d)-(f) The plane perpendicular to the upstream magnetic field direction. As indicated, Plates 1a and 1d correspond to the case with no mass-loading and reflective boundary conditions, Plates 1b and 1e correspond to mass loading and reflective boundary conditions, and Plates 1c and 1f correspond to the mass loading and fixed boundary conditions. The spectral color table indicates the magnitude of magnetic field. The strong influence of the Alfvén wings is apparent on the non-mass-loaded flow (Plates 1a and 1d), and is weakened with the addition of mass loading. The increased magnetic field perturbation in the wake is apparent in the mass-loaded cases. The spatial scale covers from -10 to +12 Io radii horizontally and to ±8 Io radii vertically.

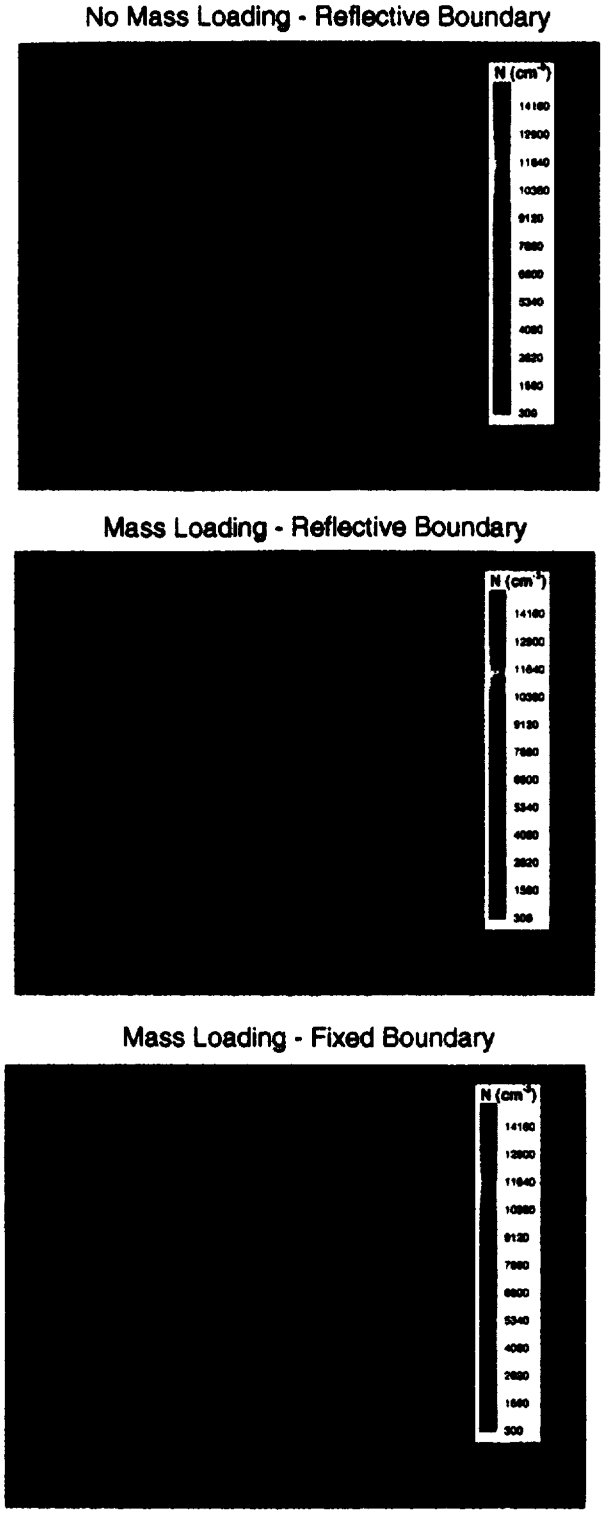

Plate 2. Plasma density for the non-mass-loading and mass-loading flows past Io. (a) The plasma density for the models with no mass-loading and reflective boundary conditions, in (b) for mass-loading and reflective boundary conditions, and in (c) for mass-loading and fixed boundary conditions. The non-mass-loading model (Plate 2a) produces a rarefied region in the wake, contrary to the Galileo particle measurements. Both mass-loading models (Plate 2b and 2c) produce a strong density peak in the wake behind Io. The symmetry line through Io covers distances from -4 to +8 Io radii.

Voyager-era estimates but may be consistent with the apparent overall larger Io atmosphere and torus activity in recent times compared with the Voyager era.

The general flow pattern in both mass-loading models is similar to the typically suggested qualitative pictures. For example, see *Schneider et al.* [1991]. Very close to Io and especially in the extended wake region the flow is very slow (a few km s^{-1}) where the effects from the locally produced ions and from charge exchange are most important. Because the Galileo trajectory is nearly in the perpendicular plane and because there is not much difference between the two models in this plane a comparison of the velocity field with the Galileo results provides little discrimination between the two alternative boundary conditions. Figure 2 shows the flow velocity vectors along the spacecraft trajectory for both mass-loading models, which give virtually identical results. The flow directions and change in the velocity magnitude in the orbit plane are quite similar to those shown in Figure 1 of *Frank et al.* [1996]. Note again, however, that Frank et al. reported asymptotic velocity magnitudes far from the wake (4 Io radii) somewhat below strict corotation (45 km s^{-1} as opposed to 56 km s^{-1}). They warned that their uncertainties were asymmetric and large enough to include strict corotation, being dependent on the details of their assumed plasma ion composition. Our model results yield corotational velocities far from Io with somewhat supercorotational velocities (13% enhancements) in the immediate flanks of the wake near Io, about 2 Io radii from the center of the wake.

In ideal MHD the current density can be calculated as the curl of the magnetic field vector. Extracting quantities determined from components of field gradients near Io, where they are largest, is uncertain because of the presence of cut-cells (partial cubes which contain the inner boundary at one face), because of the conversion from cell-averaged parameters to node-values, and because of boundary effects. For the model runs shown here the cell structure was not optimized to obtain highly accurate currents. We can say at least qualitatively that the largest values of the current density in all three models occur near the body. As one might expect, currents associated with the Alfvén wings are the strongest in the non-mass-loading reflective boundary model and weakest for the mass-loading fixed boundary model. In the mass-loading fixed boundary model we can also estimate the integrated current from the current density near Io to be on the order of a few x 10^6 amperes. This is comparable to independently estimated values [*Khurana et al.*, 1997] for both the Galileo and Voyager epochs.

Preliminary pictures of the global shape of the local ionosphere of Io have been presented based on radio occultation measurements by *Flasar et al.* [1997] and plasma wave measurements by *Gurnett et al.* [1997]. This overall shape is dominated by the dense, stagnant, and heavily mass-loaded region indicated by the very low velocities which excludes the outer plasma torus flow, as seen in Plate 2. It is apparent then that the overall structure of Io's upper ionosphere may be largely controlled by the combination of mass loading and plasma torus flow past Io. Furthermore, the upstream-dawn and downstream-dusk ionosphere profile asymmetry seen in the Pioneer 10 radio occultation measurements [*Kliore et al.*, 1974, 1975], that are qualitatively similar to the preliminary Galileo measurement, is then most likely an upstream/downstream phenomenon rather than a

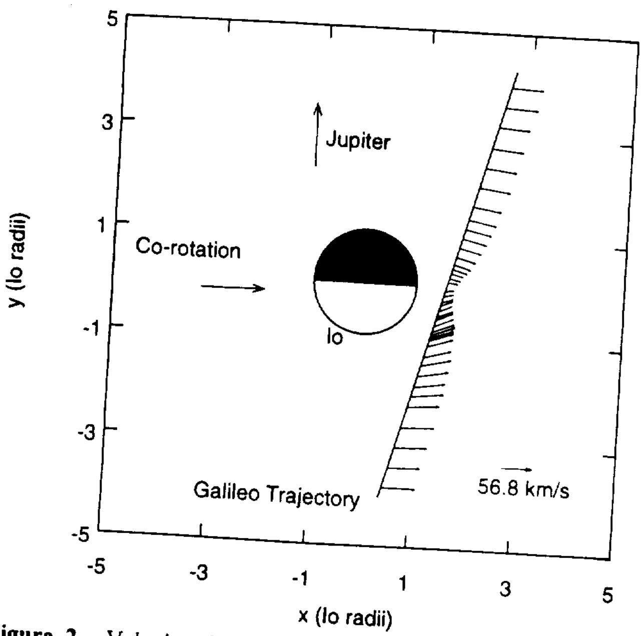

Figure 2. Velocity flow vectors along the December 1995 Galileo flyby trajectory. Shown along the projected trajectory in Io's orbit plane are the velocity vectors (direction and magnitude) from our mass-loaded MHD model calculations. The results for the fixed boundary model are shown but the reflective boundary model is virtually identical. Both the variations in direction and variation in magnitude of the velocity are quite similar to those by *Frank et al.* [1996] obtained from the Galileo plasma ion measurements. The absolute velocities from the measurements are uncertain at this time.

dawn-dusk one. This has been noted previously by *Kivelson et al.* [1979]. Preliminary Hubble Space Telescope measurements of atomic oxygen and sulfur emissions near Io [*Trauger et al.*, 1997; *Ballester et al.*, 1997] also seem to show the presence of a bright wake.

Our case of reflective boundary conditions considers the ionosphere to be a perfectly conducting and reflecting sphere at 150 km altitude above the surface, somewhat above the electron density peak [*Flasar et al.* 1997; *Kliore et al.* 1974 & 1975]. This is certainly an overestimate of even a large but finite conductivity. Our fixed boundary condition allows plasma and magnetic flux to pass, but may underestimate the effect of the underlying high ion densities (50,000 - 90,000 cm^{-3}) at the ionospheric peak near 80 km where the ions are likely more coupled with the neutral atmosphere, increasing the conductivity. In any case these two limiting cases likely bracket the true influence of a more realistic lower ionosphere/atmosphere on the outside flow. It is interesting to note that the choice of the boundary conditions does not drastically effect the character of the direct comparison with the Galileo measurements themselves, although it does substantially change the character of the flow above and below Io in the plane parallel to the upstream magnetic field where there are as yet no Galileo data. Because of the larger deflection in the field-aligned direction for the reflective compared with the fixed boundary conditions, a higher mass-loading rate is required for the reflective case.

Note that we have already mentioned that our model with no intrinsic field, but with mass-loading and charge exchange can produce the magnetic field signature about as well as the vacuum superposition model of *Kivelson et al.* [1996b]. Assuming almost the same background field composed of a superposition of Jupiter's field and the intrinsic dipole as that of *Kivelson et al.* [1996b], *Khurana et al.* [1997] have recently presented a calculation of the magnetic field perturbation that would result from the plasma pressure as measured by Galileo PLS [*Frank et al.*, 1996]. We refer here to the broad peaks in plasma pressure (and temperature) which appear in the flanks at about 2 R_{Io} from the center of the wake. There is no corresponding density increase at this location, but it does coincide with the broad magnetic field signature. They conclude that given the validity of their assumptions only ~30% of the total field perturbation can be due to plasma effects as separate from an intrinsic magnetic field. In contrast both our models without an intrinsic magnetic field are able to account for roughly 2/3 of the total disturbance in magnetic and all of the density peak.

Although our mass-loading profile does account for the density peak, and our charge exchange profile accounts for the temperature and pressure minimum in the center of the wake they do not produce the large broad temperature and pressure peaks and the corresponding larger magnetic field disturbance in the flanks of the wake. If as *Khurana et al.* [1997] found, the enhanced plasma pressure in the flanks of the wake can account for the general breadth and depth of the magnetic field disturbance (remember this is just outside the density peak), then it is equally reasonable to conclude that if we could add a process or mechanism which would produce the enhanced temperature (and resulting pressure in absence of increased density), it should similarly also produce the correct enhanced magnetic field disturbance in our model without an intrinsic magnetic field, just as it does for their model.

Clearly then what is required is to alter our formulation to include a process which adds energy (or possibly subtracts less energy) in the flanks of the wake and/or upstream of the flanks. We consider two immediately apparent possible candidates: (1) the spatial dependence of the mass-loading and charge exchange rates, and (2) the formulation of the ion pickup process. In absence of including a detailed ion-chemical network, we adopted mass-loading and charge exchange rates which are both everywhere proportional to the measured neutral sodium radial profile of *Schneider et al.* [1991]. If the mass-loading rate and charge exchange rates are in reality not proportional to one another everywhere, it might be possible to enhance the temperature in the flanks of the wake. This increased temperature would necessarily have a corresponding increased pressure (where there is no increased density) and by the same argument as *Khurana et al.* [1997] there should also be a corresponding further decreased magnetic field. It is worth noting that our models produce somewhat super-corotational velocities enhanced by 13% just at 2 R_{Io} from the center line of the wake, exactly where the temperature is enhanced. A different velocity dependence on collision cross sections would in general be expected for the different relevant ionization and charge exchange (and knock-on) processes.

The precise forms for the ion-mass-loading and ion-neutral momentum-energy exchange (charge exchange) as functions of location around Io are in reality set by the interplay of a whole series of ion, neutral, and electron impact reactions which depend on the detailed composition of both the neutral atmosphere and plasma. Including all the effects of this kind of detailed picture for the Io flow problems has already been done for the comet solar-wind flow problem in terms of successful comparisons with in situ spacecraft data [*Gombosi et al.*, 1996] and 2-D ground-based spectra and images for H_2O^+ [*Häberli et al.*, 1997]. In the comet problem, although much more complicated in terms of total species and reactions than for Io, the details of the neutral atmosphere structure and composition are also much better understood than for Io.

The second possibility would be to reexamine the premise behind the formulation of the pick-up process. As mentioned in the model description, the ion pick-up process adopted assumes ions are produced initially in a pick-up ring and shortly thereafter scattered into a shell distribution by wave-particle interactions. Recent Hubble Space Telescope images of the Jupiter aurora with the new STIS instrument [*Clarke et al.*, 1997] show that the footprint of Io is accompanied by a trailing footprint of the wake itself extending up to one-quarter to one-half way around Jupiter. This implies that ions picked up at Io, are still being pitch angle scattered into the loss cone for 3 to 6 hours, and still precipitating along wake-crossing flux tubes into Jupiter's ionosphere for a quarter to a half a Jupiter rotation. Those picked up very close to Io, where densities are high, would be scattered immediately. This could also explain why the models provide an excellent match to all the measurements in the densest regions. The inclusion of pickup ions remaining in ring distributions would substantially alter the formulation of the MHD equations. A multispecies model that could account for a mixed ring and shell populations is beyond our current capability. It is certainly well beyond any modeling that has yet been published. It is possible that the inclusion of this process (W. Smyth, private communication, 1997) might have desired effect on the magnetic field disturbance.

4. Summary

We have demonstrated the application of an ideal MAUS-MHD model to the interaction of Jupiter's corotating plasma torus with Io's atmosphere. The model solves the single-fluid MHD flow in 3-D on an adaptively refined mesh. Because of its numerical robustness and the ability to adapt the grid structure to the flow, the heavily mass-momentum-energy loaded flow in the supersonic and sub-Alfvénic regime relevant for the interaction of Jupiter's plasma torus has been solved without the need to introduce artificial dissipative terms.

We find that we can reproduce many of the observed structures of the plasma wake behind Io as measured by various Galileo instruments. We obtain a good quantitative match to the plasma density peak, the plasma pressure and temperature minima at the center of the wake, and the vector velocity plasma flow directions .and magnitude variations. We obtain a qualitative match to the overall pressure and temperature profiles. We reproduce the magnetic field disturbance about as well as the intrinsic dipole magnetic field model of *Kivelson et al.* [1996b]. The distant flanks of the disturbance indicate a more decreased magnetic field as well as corresponding increased plasma pressure and temperature which appear to be coincident and possible correlated. Although the responsible mechanism is not yet known, it may be due to decreased cooling in the flanks from velocity-dependent collision cross sections (which are not yet taken into account) or from the influence of pickup ions that are still in ring distributions.

Acknowledgments. This work was supported by the NASA Planetary Atmospheres Program under grant NAGW-3417, the NSF-NASA-AFOSR interagency grant NSF ATM-9318181, and by NASA HPCC CAN NCCS5-146. We thank M. Kivelson and the Galileo Magnetometer team for providing us with electronic versions of the their data and for helpful conversations regarding the interpretation of their data and our model results. We thank both referees for their critical comments which have helped us to improve this paper. Conversations with W. H Smyth, J. Linker, J. Clarke, F. Bagenal, C. Groth, and T. Linde were also very helpful.

The Editor thanks two referees for their assistance in evaluating this paper.

References

Ballester, G. E., M. A. McGrath, D. F. Strobel, X. Zhu, P. D. Feldman, and H.W. Moos, Detection of the SO_2 atmosphere on Io with the Hubble Space Telescope, *Icarus, 111*, 2, 1994.

Ballester, G. E., J. T. Clarke, D. Rego, M. Combi, N. Larsenn, J. Ajello, D.F. Strobel, N.M. Schneider, and M. McGrath, Characteristics of Io's far-UV neutral oxygen and sulfur emissions derived from recent HST observations, *Bull. A. A. S. 28*, 1156, 1996.

Ballester, G. E., J. T. Clarke, M. Combi, D.F. Strobel, N. Larsenn, M. McGrath, M. Lenigan, J. Ajello, N.M. Schneider, and D. Rego, Io's far-ultraviolet emissions as observed with HST and IUE, *Bull. A. A. S. 29*, 980, 1997.

Belton, M. J. S., et al., Galileo's first images of Jupiter and the Galilean satellites *Science*, *274*, 377, 1996.

Bigg, E.K., Influence of the satellite Io on Jupiter's decametric emission, *Nature*, *203*, 1008-1010, 1964.

Clarke, J.T., G. Ballester, J. Trauger, J. Ajello, W. Pryor, K. Tobiska, H. Waite, R. Gladstone, B. Jaffel, J. Connerney, and J.C. Gerard, HST observations of Jupiter's UV aurora during Galileo in situ measurements, *Eos Trans. AGU, 78* (46), Fall Meet. Suppl., F414, 1997.

Cloutier, P. A., R.E. Daniell, Jr., A.J. Dessler, and T.W. Hill, A cometary ionosphere model for Io, *Astrophys. Space Sci.*, *55*, 93, 1978.

DeZeeuw, D. L., and K.G. Powell, An Adaptively-refined Cartesian mesh solver for the Euler equations, *J. Comput. Phys.*, *104*, 55, 1992.

DeZeeuw, D.L., T.I. Gombosi, K.G. Powell, T.J. Linde, Multiscale modeling of the solar wind-magnetosphere-ionosphere coupling with a 3D adaptive MHD model, *Eos, Trans. AGU, 77* (46), Fall Meet. Suppl., 639, 1996.

Flasar, M., D.P. Hinson, A.J. Kliore, P.J. Schinder, J.D. Twicken, R. Woo, R. Herrera, S. Asmar, D. Chong, and P. Priest, Jupiter's Ionosphere: A review of Galileo radio-occultation measurements, *Ann. Geophys.*, *15* (III), 825, 1997.

Frank, L. A., W. R. Paterson, K. L. Ackerson, V. M. Vasyliunas, F. V. Coroniti, and S. J. Bolton, Plasma observations at Io with the Galileo spacecraft, *Science, 274*, 394, 1996.

Goertz, C.K., Io's interaction with the plasma torus, *J. Geophys. Res.*, *85*, 2949, 1980.

Goertz, C.K., D.E. Jones, B.A. Randall, E.J. Smith, and M.F. Thomsen, Evidence for open field lines in Jupiter's magneosphere, *J. Geophys. Res.*, *81*, 1393, 1976.

Goldreich, P., and D. Lynden-Bell, Io, A unipolar inductor, *Astrophys. J.*, *156*, 59-73, 1969.

Gombosi, T. I., D. L. De Zeeuw, R. M. Häberli, and K. G. Powell, Three-dimensional multiscale MHD model of comet plasma environments, *J. Geophys. Res.*, *101*, 15333, 1996.

Gurnett, D. A., W. S. Kurth, A. Roux, S. J. Bolton, and C. F. Kennel, Galileo plasma wave observations in the Io plasma torus and near Io, *Science*, *274*, 391, 1996.

Gurnett, D. A., W. Kurth, A. Roux, S. Perraut, and T. Chust, Galileo plasma wave observations at Jupiter, *Ann. Geophys.*, *15* (III), 825, 1997.

Häberli, R.M., M.R. Combi, T.I. Gombosi, D.L. DeZeeuw, and K.G. Powell, Quantitative analysis of H_2O coma images using a multiscale MHD model with detailed ion chemistry, *Icarus*, *130*, 373, 1997.

Hill, T.W., A.J. Dessler, and C.K. Goertz, Magnetospheric models, in *Physics of the Jovian Magnetosphere*, edited by A. J. Dessler, p. 353, Cambridge Univ. Press, New York, 1983.

Johnson, R.E., *Energetic Charged-Particle Interactions With Atmospheres and Surfaces*, Springer-Verlag, New York, 1990.

Khurana, K., M.G. Kivelson, and C.T. Russell, Interaction of Io with its torus: Does it have an internal magnetic field? *Geophys. Res. Lett.*, *24*, 2391, 1997.

Kivelson, M.G., J.A. Slavin, and D.J. Southwood, Magnetospheres of the Galilean satellites, *Science*, *205*, 491, 1979.

Kivelson, M. G., K. K. Khurana, R. J. Walker, C. T. Russell, J. A. Linker, D. J. Southwood, and C. Polanskey, A magnetic signature at Io: Initial report from the Galileo magnetometer, *Science*, *273*, 337, 1996a.

Kivelson, M. G., K. K. Khurana, R. J. Walker, J. Warnecke, C. T. Russell, J. A. Linker, D. J. Southwood, and C. Polanskey, Io's interaction with the plasma torus: Galileo magnetometer report, *Science*, *274*, 296, 1996b.

Kliore, A., D.L. Cain, G. Fjeldbo, and B.L. Seidel, Preliminary results on the atmosphere of Io and Jupiter from the Pioneer 10 s-band occultation experiment, *Science*, *183*, 323, 1974.

Kliore, A., G. Fjeldbo, B.L. Seidel, D.N. Sweetnam, T.T. Sesplaukis, P.M. Woiceshyn, Atmosphere of Io from Pioneer 10 radio occultation measurements, *Icarus*, *24*, 407, 1975.

Kogan, M.N., On the vortices and currents in magnetofluid dynamics; *Dokl. Akad. Nauk SSSR*, *139*, 58, 1961.

Lellouch, E., M. Belton, I. De Pater, G. Paubert, S. Gulkis, and T. Encrenaz, The structure, stability, and global distribution of Io's atmosphere, *Icarus*, *98*, 271, 1992.

Linker, J.A., M.G. Kivelson, and R.J. Walker, An MHD simulation of plasma flow past Io: Alfvén and slow mode perturbations, *Geophys. Res. Lett.*, *15*, 1311, 1988.

Linker, J.A., M.G. Kivelson, and R.J. Walker, The effect of mass loading on the temperature of a flowing plasma, *Geophys. Res. Lett.*, *16*, 763, 1989.

Linker, J.A., M.G. Kivelson, and R.J. Walker, A Three-dimensional MHD simulation of plasma flow past Io, *J. Geophys. Res.*, *96*, 21037, 1991.

McGrath, M.A. and R.E. Johnson, Magnetospheric plasma sputtering of Io's atmosphere, *Icarus*, *69*, 519, 1987.

McGrath, M.A., and R.E. Johnson, Charge exchange cross sections for the Io plasma torus, *J. Geophys. Res.*, *94*, 2677, 1989.

Moreno, M. A., G. Schubery, J. Baumgardner, M. G. Kivelson, and D. A. Paige, Io's volcanic and sublimation atmospheres, *Icarus* , *93*, 63, 1991.

Neubauer, F.M., Nonlinear standing Aflvén wave current system at Io: Theory, *J. Geophys. Res.*, *85*, 1171, 1980.

Pospieszalska, M. K., and R. E. Johnson, Monte Carlo calculations of plasma ion-induced sputtering of an atmosphere: SO_2 ejected from Io, *J. Geophys. Res. 101*, 7565, 1996.

Powell, K.G. An approximate Riemann solver for magnetohydrodynamics (that works in more than one dimension), *ICASE Rep. 94-24*, 1994.

Powell, K. G., P. L. Roe, R. S. Myong, T. I. Gombosi, and D. L. De Zeeuw, An upwind scheme for magnetohydrodynamics, *AIAA Pap. 95-1704-CP*, 1995.

Russell, C.T., F. Bagenal, A.F. Cheng, W-H. Ip, A. Roux, W.H. Smyth, S.J. Bolton, and C.A. Polanskey, Io's interaction with the Jovian magnetosphere, *Eos. Trans. AGU*, *78*, (9), 95, 1997.

Schneider, N.M., W.H. Smyth, and M.A. McGrath, Io's atmosphere and neutral clouds, in Time-variable phenomena in the Jovian system, *Proceedings of the Workshop on Time-variable Phenomena in the Jovian system*, NASA Spec. Publ., *NASA SP- 494*, 75-99, 1989.

Schneider, N.M., D.M. Hunten, W.K. Wells, A.B. Schultz, and U. Fink, The structure of Io's corona, *Astrophys. J.*, *368*, 298, 1991.

Shemansky, D.E., Mass-loading and diffusion-loss rates of the Io plasma torus, *Astrophys. J.*, *242*, 1266, 1980.

Sieveka, E. M., and R. E. Johnson, Nonisotropic coronal atmosphere on Io, *J. Geophys. Res.*, *90*, 5327, 1985.

Smyth, W.H., Neutral cloud distribution in the Jovian system, *Adv. Space Res.*, 12(8), 8337, 1992.

Smyth, W. H., and M. R. Combi, Io's sodium corona and spatially extended cloud: A consistent flux speed distribution, *Icarus*, *126*, 58-77, 1997.

Smyth, W.H., and D. E. Shemansky, Escape and ionization of atomic oxygen from Io, *Astrophys. J.*, *271*, 865, 1983.

Southwood, D.J., M.G. Kivelson, R.J. Walker, and J.A. Slavin, Io and its plasma environment, *J. Geophys. Res.*, *85*, 5959, 1980.

Strobel, D. F., X. Zhu, and M.E. Summers, On the vertical thermal structure of Io's atmosphere, *Icarus*, *11*,1 18, 1994.

Trauger, J.T., K.R. Stapelfeldt, G.E. Ballester, J.T. Clarke, and WFPC2 Science Team, HST observations of [OI] emissions from Io in eclipse, *Bull. A. A. S.*, *29*, 1002, 1997.

van Leer, B., Towards the ultimate conservative difference scheme, V, A second-order sequel to Godunov's method, *J. Comput. Phys.*, *32*, 101, 1979.

Williams, D. J., B. H. Mauk, R. E. McEntire, E. C. Roelof, T. P. Armstrong, B. Wilken, J. G. Roederer, S. M. Krimigis, T. A. Fritz, and L. J. Lanzerotti, Electron beams and ion composition measured at Io and in its torus, *Science*, *274*, 401, 1996.

Wolf-Gladrow, D.A., F.M. Neubauer, and M. Lussem, Io's interaction with the plasma torus: A self-consistent model, *J. Geophys. Res.*, *92*, 9949, 1987.

Wong, M. C., and R.E. Johnson, The effect of Plasma heating on sublimation-driven flow in Io's atmosphere, *Icarus*, *115*, 109, 1995.

M. R. Combi, D. L. De Zeeuw, T. I. Gombosi, and K. Kabin, Space Physics Research Laboratory, University of Michigan, 2455 Hayward Street, Ann Arbor, MI 48109-2143. (e-mail: mcombi@umich.edu)

K. G. Powell, Department of Aerospace Engineering, University of Michigan, Ann Arbor, MI 48109-2118.

(Received May 16, 1997; revised December 29, 1997;
accepted December 31, 1997.)